Aus dem Institut für Aktive Polymere
Helmholtz-Zentrum Hereon

Design and fabrication of geometry-assisted on-demand dosing systems

Dissertation

zur Erlangung des akademischen Grades

"doctor rerum naturalium"

(Dr. rer. nat.)

in der Wissenschaftsdisziplin „Materialien in den Lebenswissenschaften“

eingereicht an der Mathematisch-Naturwissenschaftlichen Fakultät der Universität Potsdam

Von

Osamah Altabal

Potsdam, 2021

Hauptbetreuer: Prof. Dr. Andreas Lendlein, Universität Potsdam

Gutachter: Prof. Dr. Andreas Lendlein, Universität Potsdam

Prof. Dr Jürgen Stampfl, Technische Universität Wien

Prof. Dr. Daniel Klinger, Freie Universität Berlin

Ort und Tag der Disputation: Universität Potsdam am 28.10.2021

Published online on the
Publication Server of the University of Potsdam:
https://doi.org/10.25932/publishup-53244
https://nbn-resolving.org/urn:nbn:de:kobv:517-opus4-532441

Statement of originality

I, Osamah Altabal, formally submit the dissertation entitled „Design and fabrication of geometry-assisted on-demand dosing systems“ to the Institute of Chemistry, Faculty of Mathematics and Natural Science, of the University of Potsdam, in the process to acquire the academic degree of Doctor of Natural Sciences (Dr. rer. nat.) in the discipline of “Materials in Life Science”.

Hereby, I certify that neither the dissertation, nor any excerpts thereof, has been previously submitted to any other institution or university to obtain a qualification or a science degree. This submission comprises my own and original work. To the best of my knowledge, it contains no material written and published by another person, except where references are provided. Support by colleagues for selected techniques is noted in the acknowledgement section.

Osamah Altabal

Potsdam, 01.06.2021

Acknowledgments

I would like to express my sincere gratitude to my supervisor Prof. Dr. Andreas Lendlein for providing me the opportunity to accomplish the work for this thesis at the Institute of Biomaterial Science of HZG and for his valuable guidance and numerous scientific discussions, which always brought me steps forward.

I thank my second supervisor Prof. Dr. Carsten Beta for his support in my projects and for his advices during my PhD study.

I would like to thank my mentor Dr. Christian Wischke for his valuable suggestions, helpful scientific advices and his friendly behavior, which always provided me strength to work harder and in a delightful way.

Special thank goes to my colleagues Dr. Fabian Friess and Florian Störmann who played a remarkable supportive role during the journey towards my PhD thesis as well as for providing necessary assistance regarding the project. I also want to thank Dr. Elizabeth Wailes and Dr. Dilek Saglam.

I am very thankful to Dr. Ulrich Nöchel and Dr. Matthias Heuchel for their support in customizing specific set-ups for the mechanical analysis and introduction to some analytical methods. I also want to thank Dr. Thomas Weigel for XPS measurements, Daniela Radzik for functionalizing the PCL Polymer, Susanne Schwanz for DSC measurements and Yvonne Pieper for TEM measurement.

Above all, I am extremely thankful to my parents and my wife who supported me to achieve my target.

Osamah Altabal

Table of content

Abstract

The controlled dosage of substances from a device to its environment, such as a tissue or an organ in medical applications or a reactor, room, machinery or ecosystem in technical, should ideally match the requirements of the applications, e.g. in terms of the time point at which the cargo is released. On-demand dosage systems may enable such a desired release pattern, if the device contain suitable features that can translate external signals into a release function. This study is motivated by the opportunities arising from microsystems capable of an on-demand release and the contributions that geometrical design may have in realizing such features. The goals of this work included the design, fabrication, characterization and experimental proof-of-concept of geometry-assisted triggerable dosing effect (a) with a sequential dosing release and (b) in a self-sufficient dosage system. Structure-function relationships were addressed on the molecular, morphological and, with a particular attention, the device design level, which is on the micrometer scale. Models and/or computational tools were used to screen the parameter space and provide guidance for experiments. In this line, two concepts were explored in this thesis:

Concept 1: Stress concentration in micro-structured materials for a sequential dosing function

When a tensile load acts on materials with cutouts, a stress concentration can occur, which is typically considered as an obstacle that should be avoided during the engineering of load bearing structures to prevent their failure. In this study, it is hypothesized that exploiting cutouts as cues should enable a tensile-induced sequential dosing function by stress and strain concentration. Conceptually, utilizing coated microcavities of different geometrical shapes within a single substrate will concentrate the stress differently at each microcavity upon stretching (function 1). This stress should transfer locally to the coating layer, allowing tailored dosing via controlled coating rupture (function 2) of individual cavities according to their shapes. Coupling function 1 to function 2 will be enabled by a strong adhesion at the substrate-coating interface.

In designing such a dosing device, a key step was to understand how the shape and arrangement of different cavities on a substrate influence the stress concentration factor

(SCF) of each individual cavity considering the direction of deformation. This was studied by finite element analysis (FEA). Results indicated that cavities, which are perpendicularly oriented to the direction of the applied load, e.g. vertical rhombuses, displayed a high SCF. Deeper cavities in the substrate also exhibited an increased SCF, which can be quantitatively described and distinguished. Additionally, when combining geometrical cavities of different SCF in a substrate, e.g. vertical rhombuses and circles (named design 2), the SCF of each cavity remained unaffected at least in the model. These findings underpin the feasibility of the shape-controlled mechanical dosing concept and have been used to guide the experimental device design.

In order to explore the feasibility of local stress-transfer from the site of shaped microcavities to a coating layer, the mechanism of the stress transition from ductile substrates to a brittle thin coating layer at the site of cutouts was evaluated by FEA. Substrates containing coated-shaped cavities of differential SCF values (circle cavities with SCF =2.5 and vertical rhombus cavities with SCF = 5.2) were simulated under a tensile load. It was detected that the magnitude of the stress at the substrate-to-coating interface is highest at the cavities with the higher SCF, i.e. at rhombus cavities compared to circular cavities. In addition, the correlation between the coating thickness and the SCF in the coating layer was simulated by FAE, whereby it was detected that increasing the coating thickness from 1 to 15 µm reduces the SCF at the coating-substrate interface and vice versa. These findings conceptually demonstrate the feasibility of the hypothesis.

Practically, a strong interfacial adhesion between the coating-substrate is required to avoid coating detachment upon stretching. In this context, polydopamine (PDA) was applied on the substrate as an intermediate layer that exposes amines and alcohol groups on the surface, which are assumed to initiate the polymerization of cyanoacrylate (CA) monomer in situ at the substrate surface. This was confirmed by the X-ray photoelectron spectroscopy, by which it was concluded that the primary amine groups of PDA contribute to the initiation of CA polymerization.

Based on the outcome of the previous evaluations, prototype devices were fabricated from polydimethylsiloxane (PDMS). They were then treated with PDA, their micro-reservoirs were loaded with dyes (as model compounds) and sealed by in situ polymerized poly(n-

butylcyanoacrylate) PBCA with a layer thickness of 2 µm ± 0.9 µm. By subjecting the devices to a continuous uniaxial stretching, the sequential dosing function was demonstrated successfully by subsequent initiation of release of two dyes. As expected, the dosing was initiated first from rhombus cavities (due to high SCF and StrCF) at ε ≈ 1 ± 0.3% (n = 3) and then from circle cavities (low SCF, and StrCF) at ε ≈ 12 ± 1% (n = 3).

Concept 2: Self-sufficient thermo-responsive dosing device

The Poisson's ratio (v) of materials describes their change in lateral dimensions upon uniaxial stretching. Materials typically have a positive v, i.e. they become smaller in y- and z-direction when being stretched in x-direction. In contrast, a specific 3D design can exhibit a negative Poisson's ratio (NPR), e.g. re-entrant hexagon (re-Hex) structures, which show bidirectional expansion upon unidirectional stretching. Often, the NPR effect arises by a direct contact (e.g. stretching) with the structures. Here, however, the NPR structure was exploited for self-sufficient switchable devices by coupling different functions together. In this concept, a shape-memory polymer (SMP) (function 1) provided an active principle integrated in a re-Hex scaffold design, leading to a free-standing bi-axial device expansion (function 2) upon stimulation of SMP. If the cavities of the re-Hex-SMP skeleton are loaded with a compound and then sealed on both sides, actuating the skeleton will enable a mechanical opening of cavities (function 3) via transferring the shape switching of the device to a coating rupture, resulting in compound release.

In this concept, the structure-function relationship of the system covers three levels. At the molecular level, the matrix material should have a covalent polymer network structure to implement the SME. A polymer network was synthesized from a linear oligo(ε-caprolactone) with its endgroups functionalized with 2-isocyanatoethyl methacrylate, which enabled the netpoints formation upon UV-induced radical polymerization. The obtained re-Hex-SMP exhibited a degree of swelling Q = 114 ± 4% (n = 3) and a gel content G = 98.5 ± 0.3% (n= 3), which confirmed that the molecular structures as needed for SME have been established.

At the morphological level, semi-crystalline structure of the polymer is necessary to enable the fixation of the temporary shape by crystalline domains (temporary netpoints), which exhibited a melting temperature T_m≈ 48 °C (n = 1). To implement the SME, the skeletons were

programmed to a defined compressed (temporary) shape via a PDMS template-based method, resulting in defined internal temporary angles with a shape-fixity rate 98.9 ± 1.2% (n = 6). By inducing the shape-recovery, the network's entropy-elasticity as a driving force allowed for a self-sufficient and active biaxial expansion of the free-standing re-Hex-SMP skeleton with a shape-recovery rate R_r ≈ 99 ± 1% (n = 6). The switching temperature T_{switch} was determined to be ≈ 49 ± 1 °C (n = 3).

At the macroscopic level, the structure-function relationship is linked to the device design. To define the suitable design parameters, an evaluation based on the hinge deformation model was performed, which provided guidelines for the experimental design. The effect of skeleton depth (b), walls thickness (t) and length (l) and the angle deformation degree ($\Delta\theta$) on the produced strain (ε) and the force during shape-recovery (F_{rec}) was evaluated. It was concluded that a re-Hex cell of $\Delta\theta$ = - 40°, b = 2.5 mm and t = 0.3 mm should exhibit the highest values of F_{rec} and ε. Accordingly, re-Hex-SMP skeletons were obtained with these dimensions and programmed to $\Delta\theta$ = -40°. When evaluated experimentally, an individual cell of re-Hex-SMP exhibited an x- axis strain ε ≈ 103 ± 12% and F_{rec}≈ 41 ± 8.7 mN (n = 6) during shape-recovery (biaxial expansion).

Polycyanoacrylates (polyCA) were selected as the coating material due to their ability of instant polymerization in situ. The strain at break (ε_B) and the force at break (F_B) of several types of polyCA coating layers were examined in situ on the re-Hex-SMP device by a micro-indentation method. PBCA with ε_B = 0.85 ± 0.3% and F_B = 4.5 ± 2 mN was identified as a suitable (breakable) coating. When compared to the obtained values during the shape-recovery of the re-Hex-SMP device (ε = 103 ± 12% and F_{rec}= 41 ± 8.7 mN), PBCA should theoretically enable the coating rupture upon device stimulation and thus an on-demand release effect.

Based on the previous evaluations, the functionality of the system has been demonstrated experimentally by employing a programmed re-Hex-SMP device that was loaded with a blue dye (as a model compound for visualizing the triggered dosing) and coated with PBCA. By increasing the temperature of the aqueous medium, the device is bi-axially expanded when the T_{switch} was reached, successfully inducing the coating failure and allowing the payload to be released. This work provided a proof-of-concept that designing of a re-Hex skeleton from

actively switchable SMP enabled expandable devices capable to achieve a dosing effect. By being operated in a non-contact mode without electronic parts, these results add technical solutions to the state-of-the-art of self-sufficient and free-standing polymer-only devices.

Both concepts have the potential to be employed as a platform for creation of geometry-related functions and the coupling of such functions to achieve on-demand dosing effects for biomedical or technical applications, including e.g. deformation / temperature sensors for use in the body or environments hostile to humans.

Zusammenfassung

Die kontrollierte Freisetzung von Substanzen aus einem Device in seine Umgebung, wie ein Gewebe oder Organ in medizinischen Anwendungen oder ein Reaktor, ein Raum, ein Gerät oder ein Ökosystem in technischer Nutzung sollte idealerweise den Anforderungen des Einsatzzweckes entsprechen, beispielsweise hinsichtlich des Zeitpunktes an dem die Freisetzung erfolgt. On-demand Freisetzungssysteme könnten eine derartiges gewünschtes Verhalten zeigen, wenn das System die Befähigung besitzt, externe Signale in eine Freisetzungsfunktion zu überführen. Diese Arbeit greift die Möglichkeiten auf, die sich durch den Einsatz und ein gezieltes Design von mikrostrukturierten Systemen für die Realisierung einer on-demand Freisetzung ergeben könnten. Die Ziele der Arbeit umfassen die Konzeptionierung, Herstellung, Charakterisierung sowie den grundsätzlichen Nachweis durch Stimuli induzierten on-demand Freisetzungsfunktion einerseits in Form eines sequentiellen Freigabeverhaltens und anderseits in Form eines autarken (kontaktfrei ausgelösten) Dosiersystems. Struktur-Eigenschafts-Beziehungen wurden auf molekularer, morphologischer und - mit besonderen Augenmerk - auf der Ebene des Device-Designs untersucht. Modelle und/oder Computer-gestützte Verfahren wurden verwendet um geeignete Materialparameter zu identifizieren und einen Leitfaden für die Experimente bereitzustellen. In dieser Hinsicht wurden innerhalb dieser Arbeit zwei Konzepte verfolgt:

Konzept 1: Spannungskonzentration in mikrostrukturierten Materialien für die sequentielle Dosierfunktion

Wenn eine mechanische Belastung auf ein Material mit Defektstrukturen einwirkt, können an eben diesen Stellen Spannungskonzentrationen auftreten. Typischerweise wird im Entwicklungsprozess mechanisch belastbarer Bauteile darauf geachtet, dass Auftreten von Spannungskonzentrationen zu vermeiden, da diese ein Materialversagen hervorrufen können. Diese Studie hingegen postuliert, dass das Einbringen von Defektstrukturen zur Erzeugung von Dehnungs- und Spannungskonzentrationszonen eine dehnungsinduzierte sequentielles Dosierfunktion ermöglicht. Konzeptionell sollen beschichtete Devices mit Mikrokavitäten unterschiedlicher Geometrie erzeugt werden, welche bei Dehnung lokale Spannungs- Konzentrationen in unterschiedlicher Ausprägung hervorrufen (Funktion 1). Die Spannung soll dabei lokal auf die Beschichtung übertragen werden, wodurch eine

kontrollierte Ruptur (Funktion 2) der Beschichtung ermöglicht wird. Die Ruptur soll dabei in Abhängigkeit zur Formgestaltung der individuellen Mikrokavitäten stehen und eine steuerbare Dosierung ermöglichen. Die Kopplung beider Funktionen soll durch eine starke Adhäsionskraft zwischen Substrat und Beschichtung an deren Grenzfläche realisiert werden.

Ein Schlüsselschritt in der Auswahl eines geeigneten Designs war es, ein Verständnis dafür zu erhalten, wie die Form der Mikrokavitäten und deren Anordnung auf dem Substrat für die jeweilige einzelne Kavität den Spannungskonzentrationsfaktor (SCF) in der Dehnungsrichtung beeinflusst. Dies wurde mittels Finite-Elemente-Analyse (FEA) untersucht. Die Ergebnisse zeigten, dass Kavitäten, welche senkrecht zur aufgebrachten mechanischen Belastung ausgerichtet waren, wie zum Beispiel vertikale Rhomben, einen hohen SCF aufwiesen. Die quantitative Untersuchung ergab zudem, dass tiefere Kavitäten im Substrat ebenfalls einen höheren SCF aufwiesen. Wurden Kavitäten mit unterschiedlichen SCF in einem Substrat kombiniert, so zeigte sich, dass die individuellen SCF der einzelnen Kavitäten, wie zum Beispiel vertikale Rhomben und Zylinder (Design 2), zumindest im Modell unverändert blieben. Diese Befunde unterstrichen die Realisierbarkeit eines formkontrollierten und mechanischen Dosierkonzepts. Die Erkenntnisse wurden daraufhin dazu verwendet, die Formgebung der Prototypen festzulegen.

Die Untersuchung der lokalen Spannungsübertragung im Bereich der Mikrokavitäten in einem duktilen Substrat hin zu einer dünnen und spröden Beschichtung oberhalb dieser Strukturen erfolgte ebenfalls mittels FEA. Die Simulation beschichteter Substrate mit geformten Mikrokavitäten unterschiedlicher SCF (kreisförmige Kavitäten mit SCF = 2,7 und vertikale Rhomben mit SCF = 5,2) erfolgte unter Anwendung einer Streckbelastung. Die Spannungsübertragung an der Substrat-Beschichtungs-Grenzfläche war dabei für Mikrokavitäten mit höherem SCF am größten, das heißt für vertikale Rhomben im Vergleich mit kreisförmigen Vertiefungen. Zusätzlich wurde der Zusammenhang zwischen der Beschichtungsdicke und dem SCF der Beschichtung mittels FEA simuliert. Es zeigte sich, dass eine Vergrößerung der Beschichtungsdicke von 1 zu 15 µm den SCF an der Substrat-Beschichtungs-Grenzfläche verringerte. Die Ergebnisse bekräftigten die Realisierbarkeit der Hypothese.

Für eine praktische Anwendung eines solchen Systems muss jedoch eine starke Adhäsion zwischen dem Substrat und der Beschichtung gewährleistet werden, um ein unvorhergesehenes Ablösen der Deckschicht während der Dehnung zu unterbinden. In diesem Zusammenhang wurde eine Polydopamin (PDA) Zwischenschicht auf dem Substrat aufgebracht, welche sowohl Amin- als auch Alkoholgruppen auf ihrer Oberfläche aufweist, die ihrerseits eine in situ Initiierung der Polymerisation von Cyanoacrylat (CA) Monomeren ermöglichen soll. Diese Annahme konnte mittels Röntgenphotoelektronenspektroskopie (XPS) als zutreffend nachgewiesen werden und bestätigte, dass primäre Amingruppen der PDA Zwischenschicht die CA-Polymersation initiierten.

Basierend auf den Ergebnissen der Voruntersuchungen wurden Prototypen auf Grundlage von Polydimethylsiloxan (PDMS) angefertigt. Diese wurden mit PDA behandelt, dessen Mikrokavitäten mit Farbstoff als Modellsubstanz beladen und abschließend mittels in situ Polymerisation von n-Butylcyanoacrylat (PBCA) mit einer Schichtdicke von 2,0 ± 0,9 µm versiegelt. Eine kontinuierlich angewendete uniaxiale Belastung der Devices zeigte eine erfolgreiche sequentielle Freisetzung von zwei unterschiedlichen Farbstoffen. Wie vorausgesagt erfolgte die Freisetzung zuerst aus Kavitäten der Rhombusform bei $\varepsilon \approx 1{,}0$ +-0,3% (n = 3) aufgrund des höheren SCF und StrCF. Danach erfolgte die Freisetzung aus kreisförmig Kavitäten bei $\varepsilon = 12 \approx 1\%$ (n = 3) wegen des vergleichsweise niedrigen SCF und StrCF.

Konzept 2: Autarkes thermoresponsives Dosiersystem

Das Poisson-Verhältnis von Materialien beschreibt die Veränderung der lateralen Dimensionen nach erfolgter uniaxialer Dehnung. Typischerweise besitzen Materialien ein positives Poisson- Verhältnis, das heißt, diese werden schmaler in y- und z-Richtung bei erfolgter Dehnung in x- Richtung. Im Gegensatz hierzu können Gerüststrukturen mit einem bestimmten 3D-Design ein negatives Poisson-Verhältnis (NPR) aufweisen, wie zum Beispiel gefaltete hexagonale Strukturen (re-Hex), welche eine bidirektionale Ausdehnung als Folge einer uniaxialen Dehnung aufweisen. Häufig wird die NPR-Funktion durch ein direktes Einwirken auf die Gerüststruktur hervorgerufen (zum Beispiel durch mechanische Belastung). In dieser Studie hingegen wurden Gerüststrukturen untersucht, welche eine autonome

Auslösung des NPR-Effekts aufgrund der Kopplung verschiedener Funktionen zulassen. re-Hex-Gerüststrukturen basierend auf einem Formgedächtnispolymer (SMP) (Funktion 1) stellten ein aktives Schaltelement bereit, welches eine autonome biaxiale Strukturausdehnung (Funktion 2) nach Auslösung des SME ermöglicht. Im Falle einer Beladung der re-Hex Skelettstruktur mit einer Wahlsubstanz und seiner beidseitigen Versiegelung durch eine aufgebrachte Beschichtung kann eine Auslösung des SMP durch Spannungsübertragung zu einer mechanischen Öffnung der Kavitäten (Funktion 3) mittels Ruptur der Beschichtung führen. Hierdurch soll die eingeschlossene Substanz freigesetzt werden.

Die Struktur-Funktions-Beziehung dieses Konzepts deckt dabei 3 Ebenen ab. Das Matrixmaterial sollte aus einem kovalent vernetzten Polymernetzwerk bestehen (molekularer Ebene), welches Grundlage für die Implementierung des SME ist. Das Polymernetzwerk wurde aus linearen Oligo(ε-caprolacton) (oCL) Telechelen, dessen Endgruppen mittels 2-Isocyanatoethyl methacrylat (IEMA) funktionalisiert wurden, erhalten. Die Netzpunkte wurden durch die UV- induzierte radikalische Polymerisation der IEMA-Endgruppen erzeugt, wobei die Umsetzung der Methacrylatendgruppen mittels IR-Spektroskopie nachgewiesen wurde. Die erhaltenen re-Hex- SMP wiesen einen Quellungsgrad von Q = 114 ± 4% (n = 3) und einen Gelgehalt von G = 98,5 ± 0,3% (n = 3) auf. Anhand der Ergebnisse konnte geschlussfolgert werden, dass die für den SME benötigten molekularen Netzwerkstrukturen erhalten wurden.

Auf morphologischer Ebene werden semi-kristalline Polymerstrukturen benötigt um eine Fixierung der temporären Form durch kristalline Domänen als temporäre Netzpunkte zu erreichen. Die hier entwickelten Prototypen zeigten einen Schmelzpunkt von T_m = 48 °C (n = 1). Zum Zwecke der Implementierung des SME wurden die Skelettstrukturen durch Deformation mittels PDMS Matrizen in eine definierte temporäre Form überführt. Diese Programmierung der temporären Form lieferte definierte innere Winkel (a_{tem}) mit einem Fixierungsgrad von R_f = 98,9 ± 1,2% (n = 6). Nach dem Auslösen des SME, führte die Entropie-elastische Rückstellung des Polymernetzwerks zu einer autonomen und aktiven biaxialen Ausdehnung der re-Hex-SMP Gerüststruktur mit einem Rückstellgrad von R_r = 99 ± 1% (n = 6). Die Schalttemperatur T_{switch} lag bei 49 ± 1 °C (n = 3) und konnte der Schmelztemperatur der kristallinen Domänen zugewiesen werden.

Auf makroskopischer Ebene ist die Struktur-Funktions-Beziehung mit dem Device-Design verknüpft. Geeignete Designparameter wurden mit dem Hinge-deformation model ermittelt, welche nachfolgend in das Prototypdesign eingeflossen sind. Der Effekt der Devicedicke (Skeletttiefe) (b), der Wandstärke (t) und Wandlänge (l), sowie die Winkeldeformation in Grad ($\Delta\theta$) auf die erzeugte Dehnung (ε) und Spannung (F_{rec}) während der Formrückstellung wurden untersucht. Es konnte gefolgert werden, dass eine re-Hex-Zelle mit $\Delta\theta$ = - 40°, b = 2,5 mm und t = 0,3 mm sowohl die höchsten Werte für F_{rec} als auch für ε ergeben. Demzufolge wurde eine re-Hex-SMP Skelettstruktur mit eben diesen Parametern in einer photolithographisch erzeugten Gussform durch Photovernetzung hergestellt und anschließend zu einem Winkel von $\Delta\theta$ = - 40° programmiert. Experimentell wurden für eine re-Hex- Zelle während der biaxialen Formrückstellung eine Dehnung von ε = 103 ± 12% in x-Richtung und eine Spannung von F_{rec} = 41 ± 8,7 mN (n = 6) ermittelt.

Polycyanoacrylate (PolyCA) wurden aufgrund ihrer Fähigkeit zur in situ Polymerisation als Beschichtungsmaterial ausgewählt. Die Bruchdehnung (ε_B) und Bruchspannung (F_B) wurden direkt am re-Hex-SMP für verschiedene polyCA-Beschichtungen mittels Mikro-indentations-technik ermittelt. PBCA wurde aufgrund der Brucheigenschaften (ε_B = 0,85 ± 0,3% und F_B = 4,5 ± 2 mN) als geeignetes Beschichtungsmaterial ausgewählt. Im direkten Vergleich zu den erhobenen Werten der re-Hex-SMP während der Formrückstellung (ε = 103 ± 12% und F_{rec} = 41 ± 8,7 mN) sollte eine Ruptur der PCBA Deckschicht durch Auslösen des SME theoretisch möglich sein und eine bedarfsgerechte Freisetzung von eingelagerten Substanzen erfolgen.

Basierend auf den Voruntersuchungen wurde die Funktionalität dieses Systems experimentell bestätigt. Hierzu wurden programmierte re-Hex-SMP Skelettstrukturen mit einem blauen Farbstoff als Modelsubstanz zur Visualisierung der gesteuerten Freisetzung beladen und mit PBCA beschichtet. Durch Erhöhung der Temperatur des wässrigen Umgebungsmediums konnte nach Erreichen von T_{switch} eine biaxiale Ausdehnung der Gerüststruktur und eine simultane Ruptur der Beschichtung festgestellt werden, wodurch eine abrupte und vollständige Freisetzung des Farbstoffes nachgewiesen werden konnte. Diese Arbeit lieferte den konzeptionellen Beweis, dass Systeme zur bedarfsgerechten Dosierung durch re-Hex Gerüststrukturen auf Basis einer SMP-Matrix ermöglicht werden können, wobei die Freisetzung auf Grundlage eines aktiv gesteuerten SME erfolgt. Aufgrund der kontaktlosen Ansteuerung und dem vollständigen Verzicht auf elektronische Bauteile stellt dieses

ausschließlich polymere System nach dem Stand der Technik eine technische Lösung für freistehende und autonome Freisetzungssysteme bereit.

Die beiden hier vorgestellten Konzepte besitzen das Potential, Form-gestützte Funktionen zu realisieren und durch Kopplung solcher Funktionen Dosiersysteme für eine kontrollierbare bedarfsgerechte Freisetzung zu ermöglichen. Solche Systeme sind sowohl für den biomedizinischen Bereich als auch für technische Anwendungen von Interesse, wie zum Beispiel Dehnungs/Temperatursensoren im menschlichen Körper oder in unwirtlichen, für den Menschen gefährlichen Umgebungen.

Abbreviation and symbols

A_{gross}	Cross-section area of an unstructured substrate
A_{net}	Cross-section area of a structured substrate
D_{cavity}	Depth of the cavity
$D_{substrate}$	Depth of the substrate
K_h	Hinge force constant
R_f	Shape fixity ratio
R_r	Shape recovery ratio
T_g	Glass transition temperature
T_m	Melting temperature
T_{switch}	Switching temperature need to be exceeded to induce a SME
T_{trans}	Thermal transition temperature
α_{per}	Permanent angle
α_{tem}	Temporary angle
$\varepsilon_{nominal}$	Nominal overall strain
ε_0	Elongation of a sample in the permanent shape
ε_B	Elongation at break
ε_{local}	Local strain
$\varepsilon_{longitudinal}$	Longitudinal (axial) strain
ε_m	Maximum elongation
ε_{trans}	Transverse (lateral) strain
ε_u	Elongation after unloading of SMP sample in thermo-mechanical experiment
η_{per}	η of a permanent angle
η_{pro}	η of a programmed angle
η_{rec}	η after shape-recovery
η_{unload}	η after unloading
a	Axial length
BCA, PBCA	N-Butyl cyanoacrylate, poly(n-butyl cyanoacrylate)
CA	Cyanoacrylate
DSC	Differential scanning calorimetry
ECA, PECA	Ethyl cyanoacrylate, poly(ethyl cyanoacrylate)
EECA, PEECA	Ethoxyethyl cyanoacrylate, poly(ethoxyethyl cyanoacrylate)
FEA	Finite element analysis
FTIR	Fourier-transform infrared
F_{rec}	Shape recovery force
F_B	Force at break
F_{app}	Applied force
h	Length of the horizontal wall
IEMA	2-Isocyanatoethyl methacrylate
MCA, PMCA	Methyl cyanoacrylate, poly(methyl cyanoacrylate)
MECA, PMECA	Methoxyethyl cyanoacrylate, poly(methoxyethyl cyanoacrylate)
MEMS	Micro-electro-mechanical systems
mN	Milinewton
MNPs	Magnetic nanoparticles
MW	Molecular weight
N	Newton

NPR	Negative Poisson's ratio
oCL	Oligo(ε-caprolactone)
PCL	Poly(ε-caprolactone)
PDA	Polydopamine
PDMS	PDMS
PEG	Poly(ethylene glycol)
PMMA	Poly(methyl methacrylate)
PolyCA	Poly(cyanoacrylate)
PS	Polystyrene
r	Radius
re-Hex	Re-entrant hexagonal
ROP	Ring opening polymerization
SAR%	Surface area reduction percentage
SCF	Stress concentration factor
SEM	Scanning electron microscope
SME	Shape-memory effect
SMP	Shape-memory polymers
StrCF	Strain concentration factor
TEM	Transmission electron microscopy
XPS	X-ray photoelectron spectroscopy
η	Complementary degree of an angle
λ	Wavelength
E	Elastic modulus
F	Force
G	Gel content
Q	Degree of swelling
T	Temperature
b	Depth
l	Inclined wall
q	Arc length of the hinge
t	Wall thickness
δ	Displacement
ε	Elongation
θ	Angle of inclined edge to the y-axis
ν	Poisson's ratio
σ	Stress

Chapter 1 Introduction

1.1 Micro-scaled architectures and their contribution to material functions

Functions of polymeric systems are often conceptualizing a strategy based on material chemistry. However, chemistry is not the only option in material systems design. Material structures and geometry can also be linked to specific functions of polymeric systems. The geometry of particles affects the phagocytosis process and the circulation behavior of particles in *in-vivo* [1]. The shapes in patterned substrates have an influence on the differentiation or secretion profile of mesenchymal stem cells [2-4]. Polymeric micro-structures, e.g. hierarchical or cylindrical, modulate the surface wettability [5, 6] and the tip geometry of pillars influences their adhesion to dry surfaces [7, 8].

Micro-structured materials may be microspheres, shaped microparticles, foams, or substrates with cavities. Structures with macropores, e.g. scaffolds, have attracted particular interest due to their low density (mass-to-volume ratio) because of high pore volume. These features allow them to host considerably larger amounts of substances, such as dyes, drugs, catalysts, or active molecules, in comparison to non-porous structures [9].

Shaped microparticles (non spherical) and structured substrates can be fabricated by manipulating previously prepared spherical particles [10] or by micro-molding techniques e.g. photolithography [11-13]. The photolithography method has an advantage of creating reproducible and well defined shapes with distinct dimensions on silicon wafers with the support of a structured photomask. Thereafter, the structure can be replicated in an elastic polymer, typically polydimethylsiloxane (PDMS), which can be used as a template. Despite this technique produces variety of structures in three dimensions (length, width and depth), it is also called a technique of 2.5D as some geometries such as concave-, convex-, cones- and pyramid-like shapes, cannot be obtained by this technique. The principle of photolithography has been extended via combination with a microfluidic device, in which a spot of the microfluidic stream is irradiated through a photomask to produce shaped particles continuously (stop-flow microfluidic) [14-16]. Alternatively, 3D-printing can be used to produce structured materials [17-19], however, these methods may be limited by the number of polymers suitable for printing.

Though previous examples accentuate the impact of structure and geometry in different technical, biological and biomedical applications, geometry may not yet be extensively employed as cues for controlled on-demand dosing functions.

1.2 Stress concentration phenomenon

The geometry of materials (or their included structures, e.g. cutouts) influence their mechanical properties when materials are subjected to a load. In mechanics, the stress (σ) is defined as a force (F) per unit area. Applying a load, for example a tensile load, on a substrate generates an internal force, which will distribute through the substrate. This force may cause substrate failure based on the material properties and the stress intensity.

In case of an unstructured substrate, the force will uniformly distribute under the tensile load (Figure 1 A) and σ can be calculated according to Equation 1 , where A_{gross} is the gross cross-sectional area of the substrate (perpendicular to the direction of the applied force). On the contrary, when the substrate is structured e.g. by containers, holes, notch or grooves, the stress distribution through the substrate will be modified [20]. For instance, in case of a hole pierced throughout the sample, the lack of material becomes an obstacle and hence the force must redistribute around the hole (Figure 1 B). In this case, the stress will be higher because there is less material as expressed by Equation 2, where A_{net} is the net cross sectional area of the structured substrate (A_{gross} minus the area of the hole). The redistribution of the inner force will raise the stress at the edge or the tip of the structure, which may cause a local failure at a specific point. This phenomenon is known as stress concentration.

The stress concentration factor (SCF) is employed for describing the extent of the stress concentration and generally expressed by Equation 3, where σ_{max} is the maximum stress at the cutout and $\sigma_{nom}$is the nominal stress at the unstructured cross-section area as shown in Figure 1 B. For a defined shape of a cutout, e.g. ellipse cutout, the SCF can be calculated based on the equivalent ellipse concept (Figure 1 C, dashed line) according to Equation 4 [21], where *2 a* is the length of the axis of the ellipse that is perpendicular to the direction of the applied load and *r* is the radius of the curvature. Interestingly, it is also shown that the same concept can be applied to different geometries, e.g. a flower-like shape (Figure 1 C).

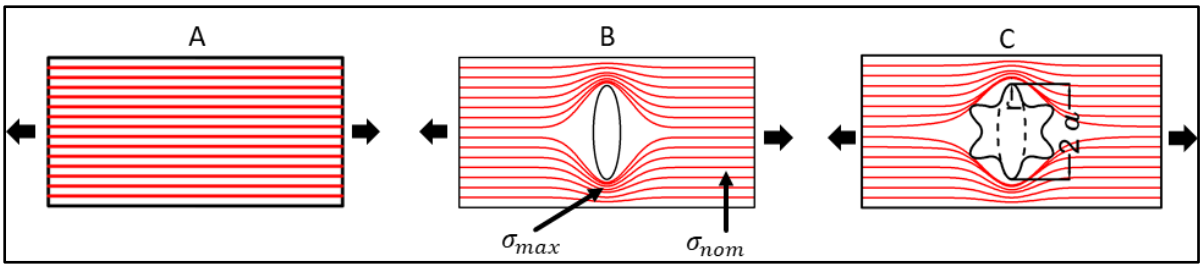

Figure 1. Scheme of stress distribution in a sample under an applied tensile load. A) Unstructured substrate with inner force uniformly distributed. B) Structured substrate with stress concentrated around the ellipse cutout. C) Concept of equivalent ellipse (dashed line) for calculation of the stress concentration factor (SCF) with applicability to different geometries (here, a flower-like shape). Arrows represent the stretching directions. Red lines represent the inner force distribution.

$$\sigma = \frac{F}{A_{gross}} \qquad \text{Equation 1}$$

$$\sigma = \frac{F}{A_{net}} \qquad \text{Equation 2}$$

$$SCF = \frac{\sigma_{max}}{\sigma_{nom}} \qquad \text{Equation 3}$$

$$SCF_{ellipse} = 2\,x\,\sqrt{\frac{a}{r}} + 1 \qquad \text{Equation 4}$$

Furthermore, it has been found that in addition to the stress concentration, the local strain is also enhanced at the site of the structure. The strain concentration factor (StrCF) is expressed generally as the local strain at the tip of a specific structure in a substrate (ε_{local}) divided by the nominal overall strain of the substrate ($\varepsilon_{\ nominal}$) (Equation 5).

$$StrCF = \frac{\varepsilon_{local\ (\varepsilon\ of\ a\ structure)}}{\varepsilon_{nominal(\varepsilon\ of\ the\ substrate)}} \qquad \text{Equation 5}$$

It has been reported that the geometry of cutouts (stress concentrator) has a substantial influence on the magnitude of stress concentration [22-24]. For example, a triangle cutout has the highest stress concentration effect, a square cutout has the next highest, and a circle has the lowest stress concentration. Moreover, the shapes' degree of curvature plays a role on the stress concentration. In general, the higher the degree of curvature, the higher the concentrated stress, where acute angles exhibit the highest stress concentration.

Stress concentration in thin films has been exploited as a tool to generate fracture-induced nano-patterns. Notches with various geometries are utilized to concentrate the stress and thus to initiate and propagate cracks in a controlled manner [25-27]. Such systems consist of stiff thin film with lateral notches supported on a flat substrate (Figure 2 A). When subjecting

the substrate to a tensile load (which exceeds the fracture strength of the thin film) via swelling, mechanical or thermal expansion (Figure 2 B), cracks are initiated at notch sites due to the concentrated stress and propagate through the stiff film.

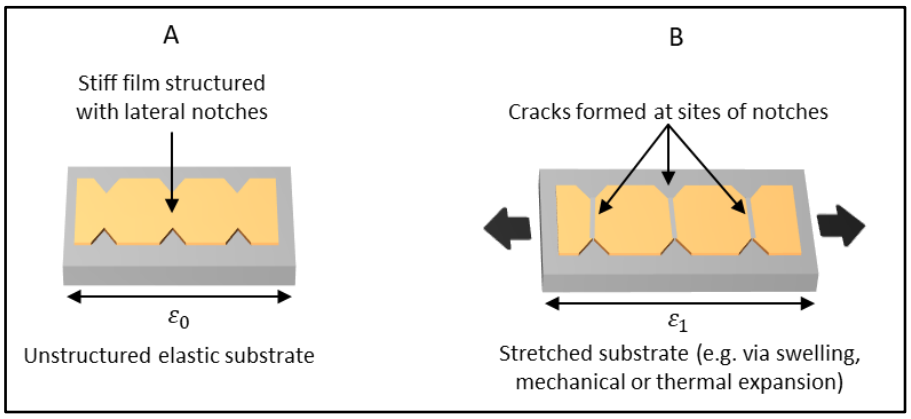

Figure 2. Scheme illustrates the principle of fracture-induced pattern based on structured thin film. A) Stiff thin film supported on an elastic substrate before stretching and B) after stretching showing the generated cracks in the film at sties of notches.

However, so far in engineering, cutouts are typically considered a critical issue as they may cause materials failure. For instance, old aircrafts with square shaped windows were crushed during flight due to stress concentration at the corners of the square windows [28]. As a consequence, all modern aircraft have oval shaped windows in order to minimize the concentrated stress. Accordingly, cutout structures have often been assumed to be obstacles that should be avoided or carefully managed during engineering to prevent structural failure.

1.3 Mechanical deformation and Poisson's ratio

Poisson's ratio: from positive to negative

Conventionally, when a bulk material is stretched in one direction (x axis), it tends to contract in the transverse directions (y, z axes) (Figure 3). In the case of compression (x axis), the material will often expand in the transverse directions (y, z axes).

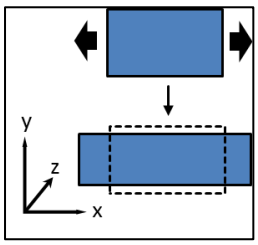

Figure 3. Scheme of typical alteration of material dimensions upon stretching (positive Poisson's ratio).

The Poisson's ratio (ν) describes this behavior and can be calculated according to Equation 6, where ν is the Poisson's ratio, ε_{trans} is the transverse strain (lateral strain) and $\varepsilon_{longitudinal}$

is the axial strain. For most common materials, ε_{trans} is negative for axial stretching and positive for axial compression, while $\varepsilon_{longitudinal}$ is positive for axial tension and negative for axial compression. Most of the common materials have a positive ν.

$$\boldsymbol{\nu} = -\frac{\varepsilon_{trans}\, of\ the\ substrate}{\varepsilon_{Longitudinal}\, of\ the\ substrate} \qquad \text{Equation 6}$$

Interestingly, by specific structuring of materials, systems can be obtained that show inverse behavior (Figure 4 C). Such a structure, also called auxetic structure, expands in the transverse direction when it is stretched (ε_{trans} and $\varepsilon_{longitudinal}$ are positives) and shrinks when it is compressed (ε_{trans} and $\varepsilon_{longitudinal}$ are negatives). According to Equation 6, such a structure has a negative Poisson's ratio (NPR). It has been found that the NPR effect is material- and mostly scale-independent. Meaning, any material having suitable mechanical properties and possessing an auxetic design can show the NPR effect from the micro- to macro-scale. To date, a variety of auxetic materials have been developed and fabricated including metals, ceramics and polymers in the form of foams, fibers or composites, e.g. based on polyurethane, ultra-high molecular weight polyethylene and polypropylene [29-39].

Geometrical design and deformation of NPR structures

The NPR phenomenon is based on structuring materials into particular 3D shapes, i.e. it is considered a geometry-related phenomenon. Various designs have been proposed and demonstrated to exhibit NPR behavior. These structures can be categorized according to their auxetic mechanisms into i) re-entrant structures ii) chiral type and iii) rotating units.

Re-entrant structures contain inward inclined walls in their designs, which create the NPR effect as illustrated in Figure 4, which compares the structure of a conventional hexagonal and re-entrant hexagonal (re-Hex) scaffold. Stretching the substrate of the conventional hexagonal multi-cells from x-axis (Figure 4 A) causes the cells to elongate along the x-axis and compress along the y-axis (Figure 4 B). Modifying the cell geometry to obtain a re-Hex design (Figure 4 C) produces the opposite behavior. The alignment of re-entrant walls beside the vertical ribs along the x-axis allows re-entrant walls to act as a hinge-like structure. Under a tensile load in x-axis (Figure 4 D), cells will flatten-out at cell-wall junctions, which causes the substrate to move apart and expand both along and transverse to the direction of the applied

load. The variation of angles between cells will alter the magnitude of Poisson's ratio and gives a strain-dependent response [40, 41]. Additionally, other re-entrant structures were developed to exhibit the NPR effect, e.g. structures of re-entrant triangle and re-entrant stars show a NPR (Figure 5) by rotating their inclined walls outwardly and opening up when being stretched [42, 43].

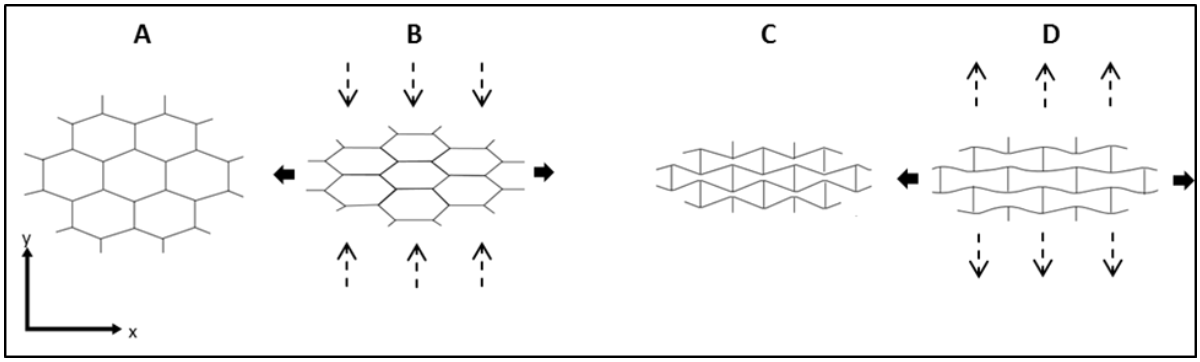

Figure 4. Illustration of the effect of a geometrical design on Poisson's ratio under applied load. Filled arrows represent the direction of stretching. A) A design of hexagonal multi-cells before and B) after stretching, which compresses transversely (dashed arrows) and exhibits a positive Poisson's ratio. C) A design of re-entrant hexagonal multi-cells before and D) after stretching, which expands transversely (dashed arrows) and exhibits a negative Poisson's ratio.

In a structure with a chiral behavior, the design consists of ligaments connected tangentially to rings [44, 45], where the structure is constructed by linking the rings unit together (the design and its NPR are shown in Figure 5 (chiral circular). Upon tensile loading, the NPR behavior arises by warping and unwarping the ligaments around the rings. Additionally, in the design of rotating units (show in Figure 5), the structure consists of shape-units connected at vertices. By stretching the substrate, the units will rotate to open up and bi-axially expand. Such structures may include designs of rotating squares, rotating rectangles and rotating rhombi [46-49].

While all aforementioned structures demonstrate an auxetic behavior, they exhibit a different magnitude of NPR. Figure 5 shows theoretical NPR values of various auxetic geometries under a tensile load from x-axis [50]. The structure of re-Hex design is considered the most distinguished among the others as it displays the highest magnitude of NPR and thus a high bi-axial expansion capability, which is ideal for creating bi-axially expandable devices for various applications [51].

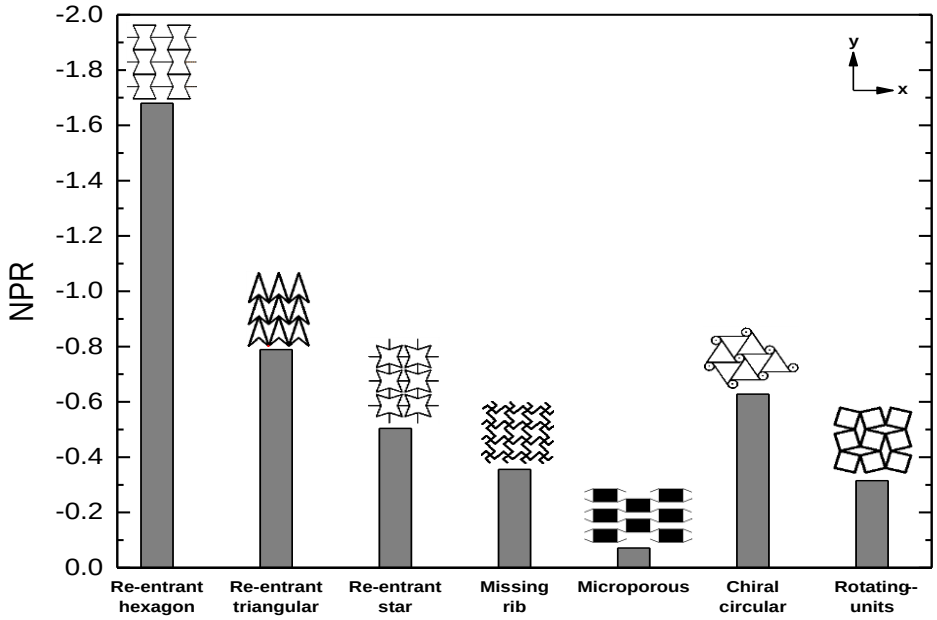

Figure 5. Review of various geometrical designs and their theoretical NPR values from reference [50]. Stretching applied from x-direction.

Model of NPR of re-entrant hexagonal design

The cell geometry of a symmetrical re-Hex cell is illustrated in Figure 6. Where α is the internal angle of the cell, h is the horizontal wall, l is the inclined wall, *t* is the wall thickness, *b* is the depth of the substrate (correspond to the z axis) and θ is the angle of the inclined edge to the y-axis. By compressing the re-Hex cell in the x-direction ($\theta < 0$), the cell will contract in the y-direction and NPR_{xy} can be defined to be:

$$NPR_{xy} = \frac{\sin\Delta\theta\ (\frac{h}{l} + \sin\Delta\theta)}{\cos^2\Delta\theta} \qquad \text{Equation 7}$$

According to Equation 7, the NPR of such a structure relates mainly to the value of θ and the ratio of h/l. Increasing the ratio of h/l will increase the magnitude of NPR and vice versa. Varying the degree of θ will alter the value of NPR such that, in case of a compression state, decreasing the value of θ (higher compressing) will enhance the NPR.

The deformation of re-Hex structure has been studied by considering deformation mechanisms of stretching and hinging models, which relate the displacement of cell walls to the applied force. The stretching model assumes that the cell walls are only able to deform by stretching along their axes with no change in angles, i.e. an elongation of l only [52]. In contrast, the hinging model assumes that the cell wall is rigid along its length. Under an axial applied load (F_{app}), the substrate will deform elastically at the junctions with other cell walls

and restore its original shape when the load is removed. The cells deform only by bending and changing the angle degree as shown in Figure 6 B [52]. Generally, the hinge model is applicable to flexible materials, e.g. flexible polymers.

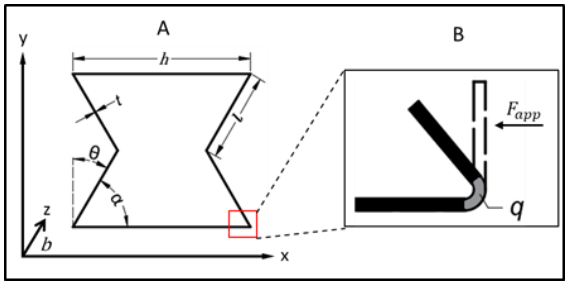

Figure 6. A) Cell geometry and coordinate system of a re-entrant hexagonal cell. B) Schematically magnified view at the hinge after deformation due to a local wall bending (dashed lines) under an applied load. The gray curve represents the arc length of the hinge (q).

For the geometry and model shown in Figure 6, F_{app} is defined by Equation 8:

$$F_{app} = K_h \delta \qquad \text{Equation 8}$$

where K_h is the hinge force constant and δ is the displacement, which are defined as:

$$K_h = \frac{Ebt^3}{6l^2 q} \qquad \text{Equation 9}$$

$$\delta = l \ sin\, \Delta\theta \qquad \text{Equation 10}$$

by substituting K_h and δ in Equation 8, F_{app} can be expressed as

$$F_{app} = \frac{E\ bt^3\ l\ sin\, \Delta\theta}{6l^2 q} \qquad \text{Equation 11}$$

where E is the elastic modulus, b is the depth of the cell, $\Delta\theta$ is the change in the degree of θ angle and q is the arc length of the hinge. According to Equation 11, increasing b, t and l and decreasing $\Delta\theta$ (higher compression) will increase F_{app}, which suggests that a higher compression force is needed to deform the cell and a higher force will be generated when the cell restores its original shape.

Application of devices with NPR structure in the biomedical field

NPR structures were suggested in the biomedical area for uses such as expandable stents [53] or smart bandages, which are loaded with active substances [54]. This bandage (with fibrous structure) can be applied to a wound, when the wound swells, the bandage will expand (opening the auxetic fibers micropores) and release the loaded substances. Furthermore, an auxetic structure was suggested for a drug delivery foam, which releases the loaded drug

based on porosity variation with an applied strain [55]. Often, the functions of systems arise from in-contact manipulation. However, the capacity of material to undergo an active movement upon an external stimulation without application of a load may expand the opportunities offered by auxetic polymer materials.

1.4 Shape-memory polymers (SMP)

Shape-memory polymers (SMPs) are mechanically active materials, which are capable of switching their shape from a temporary shape to their permanent shape upon exposure to a specific external trigger, e.g. light [56], pH value [57], magnetic field [58], ultrasound [59] or ,most commonly, temperature [60]. SMPs are required to exhibit an elastic polymer network structure, which is characterized by polymer network chains and netpoints. The polymer chains from domains, which act as switches, while the netpoints determine the permanent shape of SMPs. These netpoints can be formed physically (intermolecular interactions) or chemically (covalent bonds); the latter can be produced using methods such as UV-light-induced crosslinking of functionalized precursors [61].

The principle of active movement from a first to a second shape has been extended to a triple-shape effect. Triple-shape polymers can consist of multiphase polymer networks like AB polymers [62-64], which can actively transform from a first shape A to a second shape B and from there to the permanent shape C. The underlying concept is that shapes A and B are, on the morphological level, composing two types of phase segregated domains. Each type has a distinct and a well separated thermal transition temperature ($T_{trans,\mathrm{A}}$ for shape A and $T_{trans,\mathrm{B}}$ for shape B), which allows temporary fixing of shape A and B during the programming process. Furthermore, the concept of SMPs has been developed to include multifunctional composite materials by incorporation of functional nanoparticles into the SMP matrix. For instance, integrating magnetic nanoparticles (MNPs) into SMPs allowed for non-contact actuation of dual-shape and triple-shape effects by inductive heating via an alternating magnetic field [58, 65, 66]. Moreover, multi-shape switching [67, 68], temperature-memory materials [69], and fully reversible and reprogrammable actuators [70-72] were developed.

A representative SMP capable of a temperature-induced SME is crosslinked poly(ε-caprolactone) (PCL), which has crystallizable switching domains. Typically, the synthesis of PCL can be performed by ring opening polymerization, which gives high yields with a narrow

molecular weight distribution [73, 74]. Figure 6 A shows the chemical structure of a hydroxy-terminated PCL. The hydroxyl endgroups can be functionalized with crosslinkable moieties to create a network structure, which enable the utilization of PCL as SMP. Figure 7 B shows the chemical structure of PCL functionalized with 2-Isocyanatoethyl methacrylate (IEMA) end groups that can form covalent netpoints with each other by photo-induced free-radical crosslinking as illustrated in Figure 6 C. The crosslinking conditions, e.g. in melt or in solution, may influence the thermal and the mechanical properties of the formed network. For instance, UV-induced crosslinking of linear PCL-IEMA precursors in molten state produced network with a lower melting temperature (T_m) and higher elastic modulus than crosslinking in solution [75], which is preferential for fabrication thermo-responsive switchable multi-reserves polymeric devices.

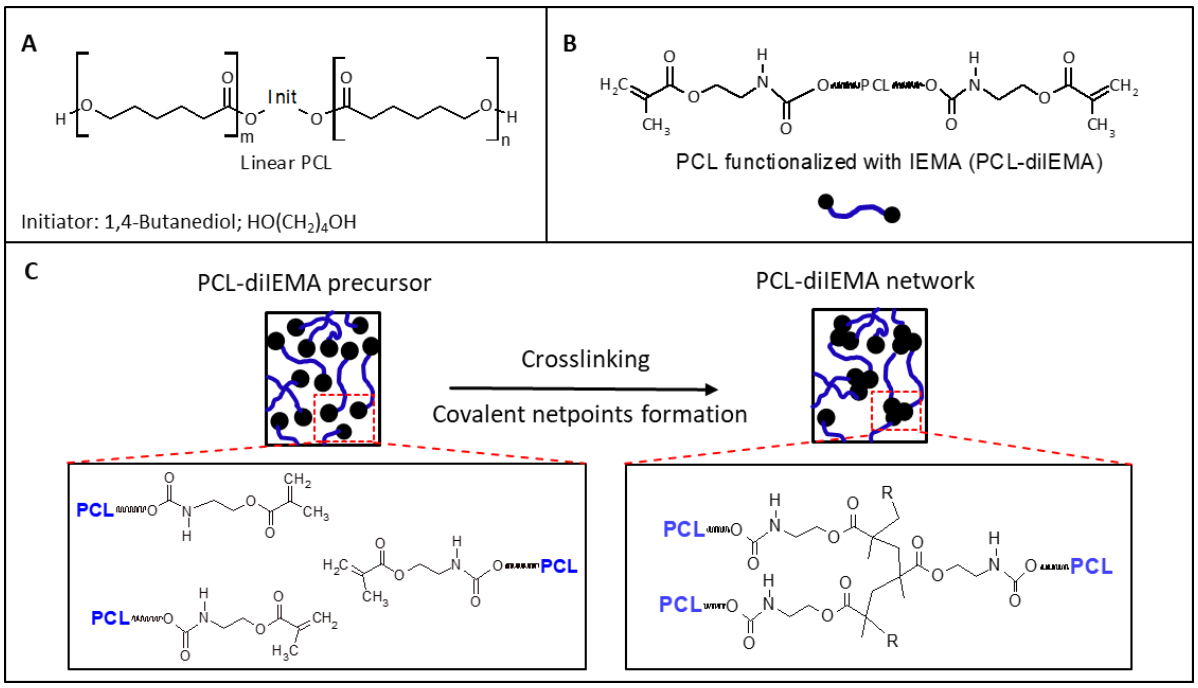

Figure 7. A) Chemical structure of hydroxy-terminated poly(ε-caprolactone) (PCL). B) Chemical structure of PCL functionalized with IEMA (PCL-dilEMA). C) Illustration of PCL-dilEMA crosslinking and covalent netpoints formation.

Actuation mechanism of SMPs

The actuation mechanism of SMPs is based on the shape-memory effect (SME). In order to implement the SME, a thermomechanical process named programming has to be applied to the polymer networks. Figure 8 (i) shows a semi-crystalline polymer network in the permanent shape, where the covalent netpoints define the permanent shape and the switching segments forms crystallizable domains that enable the fixation of the temporary

shape during programming. By heating above the melting temperature ($T > T_m$) (Figure 8 ii), the crystallites melt, the polymer segments become flexible, and elastic deformation can be performed by applying an external load, e.g. stretching. By this external load, the distance between the netpoints increased and the switching segments are uncoiled (Figure 8 ii). Cooling the networks ($T < T_m$), while keeping the external load, will fix the temporary shape at a distinct elongation due to re-crystallization of the oriented switching segments (i.e. formation of temporary netpoints) (Figure 8 iii). Heating the SMP again above the T_m removes the temporary netpoints and leads to the entropy-elastic recovery (recoiling) of deformed polymer segments, which induces a macroscopic switching of the material from the programmed (temporary) shape to the permanent shape (Figure 8 iv) [76].

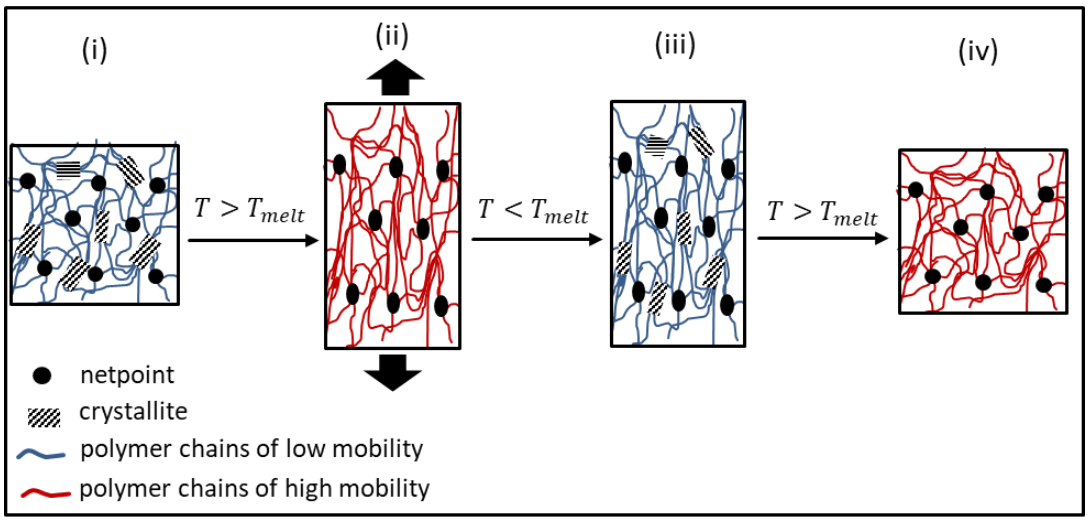

Figure 8. Schematic illustration of the molecular mechanism of a dual shape-memory polymer. i) The permanent shape of a semi-crystalline polymer network. ii) Programming by heating above the T_m, where the polymer segments become flexible and chains uncoiled by stretching (arrows). iii) Cooling below the T_m and fixation the temporary shape by re-crystallization of the oriented segments followed by unloading. iv) Inducing shape-recovery by heating above the T_m due to polymer segments recoiling (entropy-elastic recovery).

Characterization of network properties

The polymer network structure can be characterized by a number of analytical techniques. Fourier-transform infrared (FTIR) spectroscopy is a qualitative method to determine the formation of covalent networks. This method can be used to observe the conversion of the functional groups of the crosslinkable polymer (precursor) into crosslinked networks as shown in Figure 7 E [77]. Crosslinking causes end groups moieties, e.g. $=CH_2$, to form covalent bonds with one other, resulting in removing their individual peaks from the resulting FTIR spectra. The effectivity of covalent crosslinking can be determined in swelling/extraction experiments by measuring the gel content (G) according to Equation 12. While the crosslink

density can be determined by measuring the volumetric degree of swelling (Q) of a polymer network, which can be calculated according to Equation 13. Where m_{iso}, m_d and m_{sw} are the mass of the sample in the dried non-extracted state, dry extracted state and the swollen state, respectively. $p_1$and p_2 refer to the specific density of the swelling medium and the polymer network, respectively.

$$G = \frac{m_d}{m_{iso}} \qquad \text{Equation 12}$$

$$Q = 1 + p_2 \cdot \left(\frac{m_{sw}}{m_d \cdot p_1} - \frac{1}{p_1}\right) \qquad \text{Equation 13}$$

One of the key characteristics of SMP with thermally-induced SME are their thermal properties, e.g. T_g and T_m, which can be determined by differential scanning calorimetry (DSC). The macroscopic performance of SME is generally characterized by the descriptors shape fixity ratio (R_f, Equation 14) and the shape recovery ratio (R_r, Equation 15), which typically are applied for quantifying the effect of programming by an axial stretching. R_f describes the ability of switching domains to fix the mechanical deformation, which has been applied during the programming process. R_r describes the ability of the SMP-network to memorize its permanent shape, i.e., measuring how far the applied strain during programing has been recovered. Where $\varepsilon_0, \varepsilon_m$, ε_u and ε_{rec} are the elongation of the SMP sample at permanent shape, during programming, after unloading/shape fixation and after shape recovery, respectively.

$$R_f = \frac{\varepsilon_u}{\varepsilon_m} \qquad \text{Equation 14}$$

$$R_r = \frac{\varepsilon_m - \varepsilon_{rec}}{\varepsilon_m - \varepsilon_0} \qquad \text{Equation 15}$$

Furthermore, according to the intended application of SMP, a programming of the SMP sample by bending may be required. In such case, the SME can be quantified according to the bending test [77], in which the sample is bent (programmed) to a specific degree of internal angle (α) and consequently the SME is quantified based on the degree of the complementary angle (η) (Figure 9). Thereafter, the shape-recovery will be induced and the recovery rate ($R_{r,\,bending}$) and the shape fixity rate ($R_{f,bending}$) can be calculated according to (Equation 16 and Equation 17), where η_{pro}, η_{rec}, η_{per} and η_{unload} are the degree of the programmed, shape-

recovered, permanent and unloading complementary angels as shown in Figure 9. The quantification of SME by the bending test appears relevant to the hinge model introduced in section 1.3.

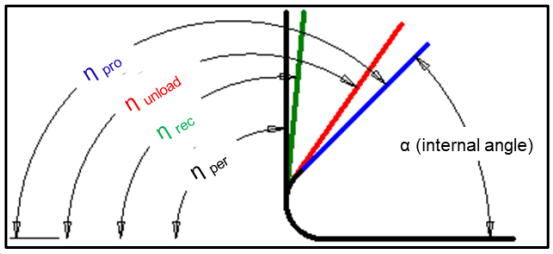

Figure 9. Schematic illustration of the SMP sample programming by the bending method and the SME characterization according to the degree of complementary angles (η). The blue line, red line, green line and the black lines are the programmed sample under load, programmed sample after unloading, sample after shape-recovery and the permanent shape of the SMP sample, respectively, and their corresponding complementary angles.

$$R_{r,bending}\,\% = \frac{\eta_{pro} - \eta_{rec}}{\eta_{pro} - \eta_{per}} \times 100 \qquad \text{Equation 16}$$

$$R_{f,bending}\,\% = \frac{\eta_{unload}}{\eta_{pro}} \times 100 \qquad \text{Equation 17}$$

Application of SMPs in switchable devices

The potential biomedical application of SMPs has been extensively studied, e.g. suggesting their use as an implant technology. This may allow for medical devices that are inserted in the body in a compact shape but can subsequently be transferred to the original, unfolded and application-relevant shape *in vivo* [78]. Examples include stents [79], heart valves [65], neuronal electrode [80] and self-tightening sutures [78]. SMPs were also suggested as matrix materials for a thermo-responsive drug carrier platform [81, 82], in which the networks were loaded with a substance of interest. Increasing the temperature induces the shape-recovery and promotes the release of the substance due to the enhanced permeability from the matrix above the T_g.

1.5 Micro-structured dosing systems

1.5.1. Passive dosing system

Diffusion-based release

Sustained dosage of substances such as drugs, proteins, enzymes and reagents (indicator) from vehicles in a controlled manner has been the basis for long-term delivery systems [83-87]. Current dosage concepts include matrices from polymers, which embed substances of interest and conventionally liberate them from the matrix without the ability of external control (passive diffusion-based release) [83]. The passive delivery system may be combined

with a membrane diffusion, in which a coating layer acts as a diffusion barrier and may prolong the release rate [88]. Passive dosing systems range from nano- to macro-scale and may include microspheres, container, multi-reservoir arrays, and reservoir-based stents [89-92].

Autonomously dosing systems

The concept of passive release has been developed to autonomously dosing systems, in which the dosing is controlled by feedback information from the environment without an external intervention. An example of such system is the self-rupturing of dextran-based gel-microcapsules coated with a polyelectrolyte membrane (polyelectrolyte; layer-by-layer technique) [93]. The rupturing of the microcapsule is triggered by the swelling pressure of the degraded microgels. To allow for a sufficient pressure for coating rupture, the degradation product must remain inside and not diffuse through the coating layer. Therefore, the study was performed at basic pH = 9, at which the membrane is impermeable for the chains fragments of the gel [93]. Another concept utilizes an implantable osmotic pump system, which typically comprises a chamber with an orifice, a piston, a drug reservoir, a semi-permeable membrane and an osmotic gradient between the piston and the membrane. In response to the osmotic gradients, water moves through the semipermeable membrane, which increases the osmotic pressure and thus drives the piston forward, pumping the drug formulation through the orifice [94, 95]

Generally, current passive and autonomous systems may be limited by a small dosage volume and by their dependency on distinct environmental conditions, e.g. osmotic pressure gradients and pH. Additionally, the release from these systems is typically preferred to be slow, often lasting up to several months for hydrophobic polymer matrices [83]. In order to allow for both a rapid and controllable release of the substance of interest, an externally stimulated system, which can rapidly expel loaded substances, would be beneficial.

1.5.2. Externally stimulated dosing

Stimuli-responsive dosing system

Here, an active external trigger is applied to accelerate or initiate the dosing from carrier systems. One applied mechanism is an enhancement of matrix erosion, which can be based e.g. on applying ultrasound to a bulk polymeric substrate. This principle was proven using a

copolymer from ethylene and vinyl acetate (EVAc) with a half-spherical (16 mm diameter) matrix loaded with salicylic acid [96]. The substrate was immersed in water to open micro-channels in the matrix by osmotic force. Subsequently, exposing the matrix to ultrasound irradiation (1 hour) enhanced the drug release due to the cavitation effect (formation, growth and collapse of microbubbles in liquid) in the micro-channels, which accelerates matrix tearing and erosion and hence the release of substances. Another example demonstrated controlling the release of wheat germ lipase from polymer network of poly[(N-isopropylacrylamide)-co-(vinyl imidazole)], which has a volume phase transition temperature (VPTT) [97]. Applying ultrasound (for 20 min) on the microgels below VPTT, where the polymer chains are expanded and the network is swollen, enhanced the released of the cargo (by a factor of 4) due to fragmentation of the polymer network into smaller pieces [97]. Additionally, ultrasound can be applied to cavitation-induced shell rupture of core-shell capsules [98]. The shell, titanium dioxide (TiO_2), suppressed the passive burst release of the loaded substance in the core. Applying an ultrasound for 15 minutes produced burst release, again due to the cavitation effect. Cavitation created at shells leads to local cracking and crumbling of the surface of the capsules.

Another mechanism is the opening of diffusion channels by using materials that exhibit a lower critical solution temperature (LCST), which shrink or shrivel by increasing the temperature above the LCST [99]. This principle was employed in the design of a nanocomposite membrane based on a thermo-responsive material, poly(N-isopropylacrylamide) (PNIPAM) [100], filled in channels of an ethyl cellulose membrane. Applying an oscillating magnetic field increases the temperature by aid of embedded MNPs and causes shrinking of PNIPAM, hence opening the channels and allowing drug flux. Furthermore, near-infrared radiation (NIR) was reported as a release trigger of ibuprofen from strands of poly(*D,L*-lactic acid) [PDLL] *in vivo* and *in vitro* [101]. The concept is based on diffusivity variation upon heating near the T_g (PDLL; T_g = 56 °C). Increasing the temperature from 37 °C to 55 °C by NIR irradiation (with support of dicarboximide dye to enhance NIR absorption) lead to the release of ibuprofen in a stepwise fashion by enhancing the diffusivity above the T_g.

Mechanical force-activated dosing systems

Mechanical forces have been addressed as an in-contact stimuli to activate dosing from flexible polymeric devices. Typical of dosing mechanisms from such systems is that under an applied load, polymer carriers undergo physical deformation which is translated to on-demand dosing, including accelerated release, based on different concepts. These concepts can be categorized based on the type of the applied force, yielding (i) compression and (ii) tensile-activated dosing.

Compression-activated dosing

The main principle of compression-induced release is based on a loss of reservoir volume. Applying a compressive strain reduces the given volume available for the loaded compound and expels it from the reservoir (Figure 10 A). An example of a dosing triggered by compression is an infusion “micro-pump” device. The device consists of an elastomeric PDMS reservoir, which is loaded with a solution of active molecules, and a valve. The dosing is triggered manually by compression with a finger [102, 103]. Similarly, spherical PDMS reservoir with a microchannel has been reported [104]. In the absence of a trigger, the system releases the payload slowly by diffusion. However, when the system is compressed, the volume of the payload exceeds the volume of the deformed reservoir and the microchannel, forcing the payload out of the device. Another study demonstrated a compression-induced release of bovine serum albumin (BSA) from porous matrices [105]. The system consists of BSA-loaded microspheres, which are incorporated in an elastomeric scaffold. Applying a cyclic compression (for 3 hours each day at 4-5% compressive strain) to the scaffolds accelerated the release of BSA due to the loss of pore volume compared to a control scaffold (without compression).

Tensile-activated dosing

The principle of tensile-triggered release is based on enlarging the surface area of the device upon stretching, accompanied with a small transverse contraction due to the Poisson's coefficient, which initiates or accelerates the release of loaded compounds (Figure 10 B). Such a principle has been reported for drug-loaded nanoparticles embedded in alginate microgel depots, which are contained in an elastomer substrate [106, 107]. In static conditions, the payload is slowly released by passive diffusion from the matrix. Upon stretching, the release is promoted due to changing of the surface area and alteration of internal volume caused by

the Poisson's ratio effect (Figure 10 B). Another principle for tension-triggered dosing are drug-loaded substrates with a thin coating as a diffusion barrier, which responds to a tension strain by opening pores or forming cracks [108]. This principle has been demonstrated to mechanically activate a release of a substance from a polymeric substrate coated with polyelectrolytes layers when stretching the substrate up to a critical strain (70%) as illustrated in Figure 10 C [109].

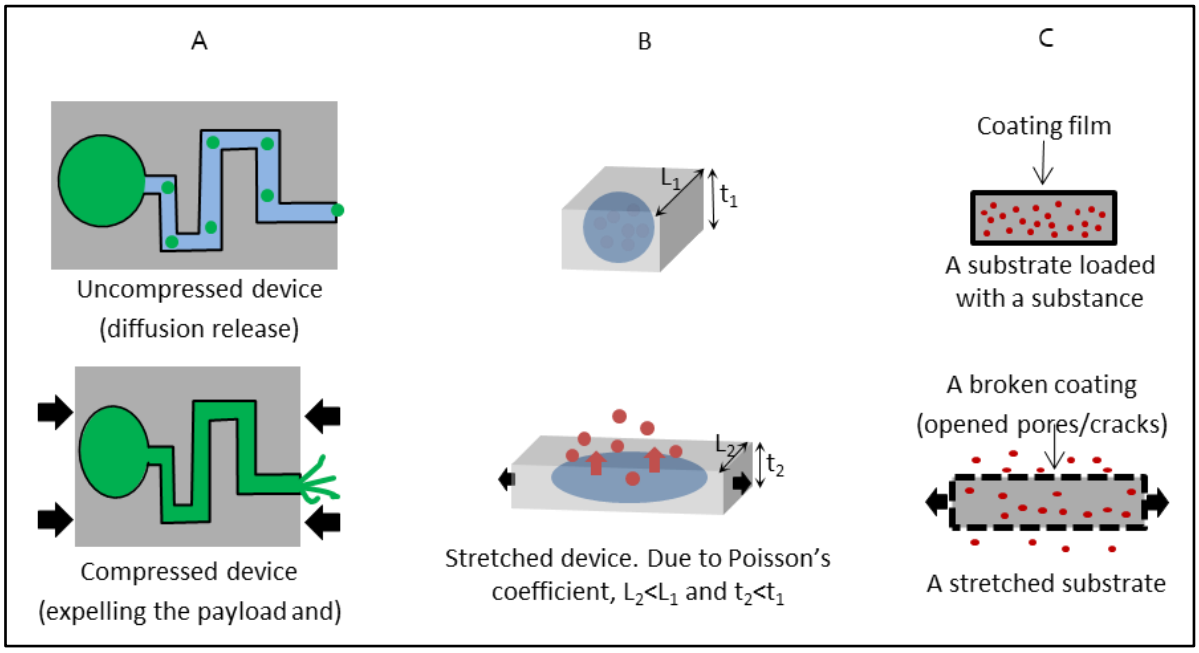

Figure 10. Principles illustration of mechanically-triggered release. A) The principle of compression-induced release. A reservoir in a static state (top) and under compression (bottom) (arrows indicates the side of compression), which expels the payload. B) The principle of tensile-Poisson-ratio-induced release. A substrate loaded with active molecules in normal mode (top) and under stretching (bottom). C) Principle of opening pores/cracks formation in a diffusion barrier layer upon stretching, which allows diffusion of loaded substances.

Despite mechanically-induced dosing systems have been pursued using various concepts and approaches, it is still not yet understood how a specific geometry may serve as cues to facilitate and control a dosing function, e.g. targeting the tensile-stimulus to a specific reservoir in order to initiate dosing or enable a sequential dosing under a tensile load.

Reservoir-based dosing devices

Although active dosing has been achieved from different systems, e.g. bulk substrate, micro-capsules, and nano-channels as described previously, these systems are limited to a small dosage volume. Therefore, the principle of active dosing from capped-reservoir devices, with a high loading capacity, has been developed based on various mechanisms. Reservoir-based

on-demand dosing systems are devices, which are typically complex in structure and consist of containers in combination with membranes, which (temporarily) serve as a diffusion barrier and will be (partially) removed from the device upon stimulation. However, to allow for such an on-demand dosing function, the device should be designed to respond to a stimulus, which should subsequently be translated to a release initiation.

One previously employed mechanism is magnetically stimulated dosing driven by active channel transport from a reservoir sealed with a flexible membrane composed of a MNPs-PDMS composite. This membrane has an orifice in the middle. Applying an alternating magnetic field deforms the membrane and expels the loaded solution out of the reservoir through the orifice (Figure 11 A) [110, 111]. Moreover, induced rapid dosing from membrane capped-reservoirs based on pressurized containers has been addressed (Figure 11 B) [112]. The container is sealed with a membrane and has micro-resistors as an actuation layer. By applying an electrical current, the micro-resistors will be heated in the loaded solution and air bubbles will be formed, which increase the pressure in the container and rupture the membrane, allowing release of loaded substance. In another design, a wireless electro-thermal actuator was reported to trigger dosing of compounds [113, 114]. This system consists of a microchip connected with reservoir arrays, which are capped with a metal membrane and metal traces for guiding the electrical current to the membrane (Figure 11 C). This complex microchip is placed in a titanium housing, which contains a micro-processor, communication electronics and a battery. Applying an electrical potential will destroy the membrane by resistive heating and release the loaded compound.

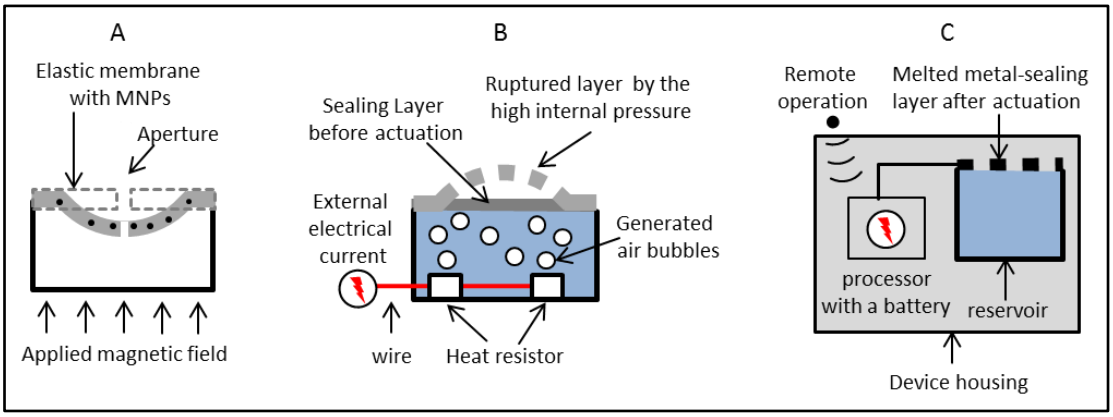

Figure 11 A) Principles of opening caped-reservoir dosing systems. A) A system with a magnetic PDMS composite membrane; membrane deformation after magnetic field application. B) A device with pressure-based actuation. Applying an electric potential heats the resistor in the solution and forms air bubbles, which increase the internal pressure and rupture the sealing layer. C) A device with a wireless activation of an electro-thermal actuator, which melts the metal sealing layer by resistive heating and release the loaded compound [111-114].

In conclusion, tensile-induced dosing systems have been addressed based on various mechanisms, which typically enabled only a single step release. However, so far, multi-release by the control of a tensile trigger (individual multi-step dosing of different compounds from a single polymeric substrate) could not be enabled. In such a device that contains various reservoirs, directing the tensile trigger to a site of a specific reservoir (among others) to initiate the dosing of the desired substance remains a challenge.

Furthermore, in case of a non-contact stimulation of dosing from reservoir-based systems that are presented in Figure 11, dosing functionality does not arise from features of the matrix materials themselves. Rather, these systems achieved their functions by aid of other integrated materials, e.g. micro-electro-mechanical systems (MEMS) and MNPs. Such techniques may involve a power supply, wires, communication processor and circuitry controller to operate and to actuate the system. In order to obtain less complex but similarly efficient systems, a key question would be if a reservoir-based on-demand dosing can be obtained and operated by a polymer-only device? So far, answers are still lacking because studies conventionally focus on composite materials and MEMS to activate dosing from sealed-reservoir devices.

Systems that would enable an on-demand dosing by mechanical principles (while being free-standing i.e. without contacting an external source of force) are of particular interest. Still, the main considerable challenges are 1) how the actuation can be generated from a polymeric device? and 2) how the actuation process can be translated to a rupture of the sealing layer? Considering these aspects may be a key for the design of a controlled dosing function based on the geometrical designs of polymer-only devices.

Chapter 2 Motivation, aims and hypotheses

2.1 Motivation and aims

Motivation

The geometry of a shaped body is a powerful design option for implementing functions in polymer devices. This vital role of geometry raised the question whether it can be harnessed as a key parameter to enable a controlled dosing function, which additionally may contribute to overcome some existing challenges. These include a distinct tensile-triggered sequential release of different compounds from a single substrate as well as an autonomous operation of the on-demand release by polymer-only devices.

Aims

This thesis aims to design, fabricate and evaluate geometry-assisted triggerable dosing effect by two types of devices that (a) show a sequential dosing release or (b) are self-sufficient dosage systems, all being fully polymer-based. Such dosing functions may arise when physical principles associated to geometrical designs, particularly stress concentration and NPR behavior, are exploited for fabrication on-demand dosing devices, where the dosing function is a result of devices (reservoirs) geometry. Devices should be designed that enable guiding an applied tensile stress to couple a mechanical input signal with a release of compounds (final effect) through sequential function-function coupling. Furthermore, combining the geometrical design of the device with a SMP, in which a mechanical stress can be stored and recalled upon external stimulation, may allow a self-sufficient (without electronics interfaces) on-demand dosing system operated in a non-contact mode.

2.2 Hypotheses

This thesis bases on the hypotheses that:

- Stretching a single substrate containing sealed reservoirs of different micro-scaled geometrical shapes creates differently concentrated strain and stress at each reservoir. Local strain and stress would transfer to the coating layer, which causes the cracking of the coating and opening of the reservoirs sequentially in a controlled order.

- Implementing a thermally induced SME in a polymer skeleton with a re-Hex structure allows an active biaxial expansion of the re-Hex skeleton upon a thermal stimulation. A self-sufficient polymer-based dosing device can be achieved by such re-Hex-SMP skeletons with sealed reservoirs, which allows translating the mechanical deformation occurring during the shape-recovery of the device into a compound release from reservoirs via rupturing of the sealing layer.

Chapter 3 Concepts and strategy

3.1 Stress concentration in micro-structured materials for a sequential dosing function

Concept

Generally, cutouts of sharp angles or of high curvature degrees are considered as obstacles that should be avoided during materials engineering as they likely cause material failure under an applied load. However, here these obstacles should be turned into a beneficial tool to create a functional device. Specifically, an on-demand sequential dosing effect is targeted via a stretch-induced controlled successive-opening of two different shapes of reservoirs in a single polymeric substrate leading to a discrete initiation of payload release in an aqueous environment. For realizing this sequential release, a difference of relative deformation in the range of 1 to 20% appears preferential for operation at micro-scaled level.

Conceptually, geometrical cutouts (reservoirs) may be used to guide the strain and the stress to a specific site, where a local failure is required (e.g. local rupture of a coating layer). In this study, sealed micro-reservoirs of distinct shapes will be explored providing micro-geometrical cues for local stress concentration (SC) and strain concentration (StrC).

In this multi-functional device, two individual functions should be sequentially coupled; (i) the stress concentration, by which a bulk deformation transforms to a distinct local deformation of different device sites and (ii) a rupturing in the coating layer occurring at different magnitudes of deformations at specific sites in order to achieve the desired effect, i.e. a sequential compound release. Figure 12 represents the idea schematically as gears to explain the concept of functions coupling. Applying a load, e.g. stretching, (Figure 12 A, input 1) to a substrate structured with cutouts (reservoirs) concentrates the stress and the strain at sites of reservoirs in a specific order, which represents the first function (Figure 12 A, output 1). When the reservoirs are sealed with a coating layer, a good adhesion at the interface of the coating-substrate (Figure 12, orange gear) should enable the transition of the output 1 to an input 2 leading to transferring the SC and StrC locally from the substrate to the coating layer. This causes a local mechanical deformation of the coating. Here, input 2 should cause crack initiation and propagation leading to a successive opening of reservoirs (output 2, Figure 12

B), i.e. coupling function 1 to function 2. Eventually, this leads to the final effect, which is a discrete payload release from the reservoirs when they are filled with the component of interest (Figure 12 C).

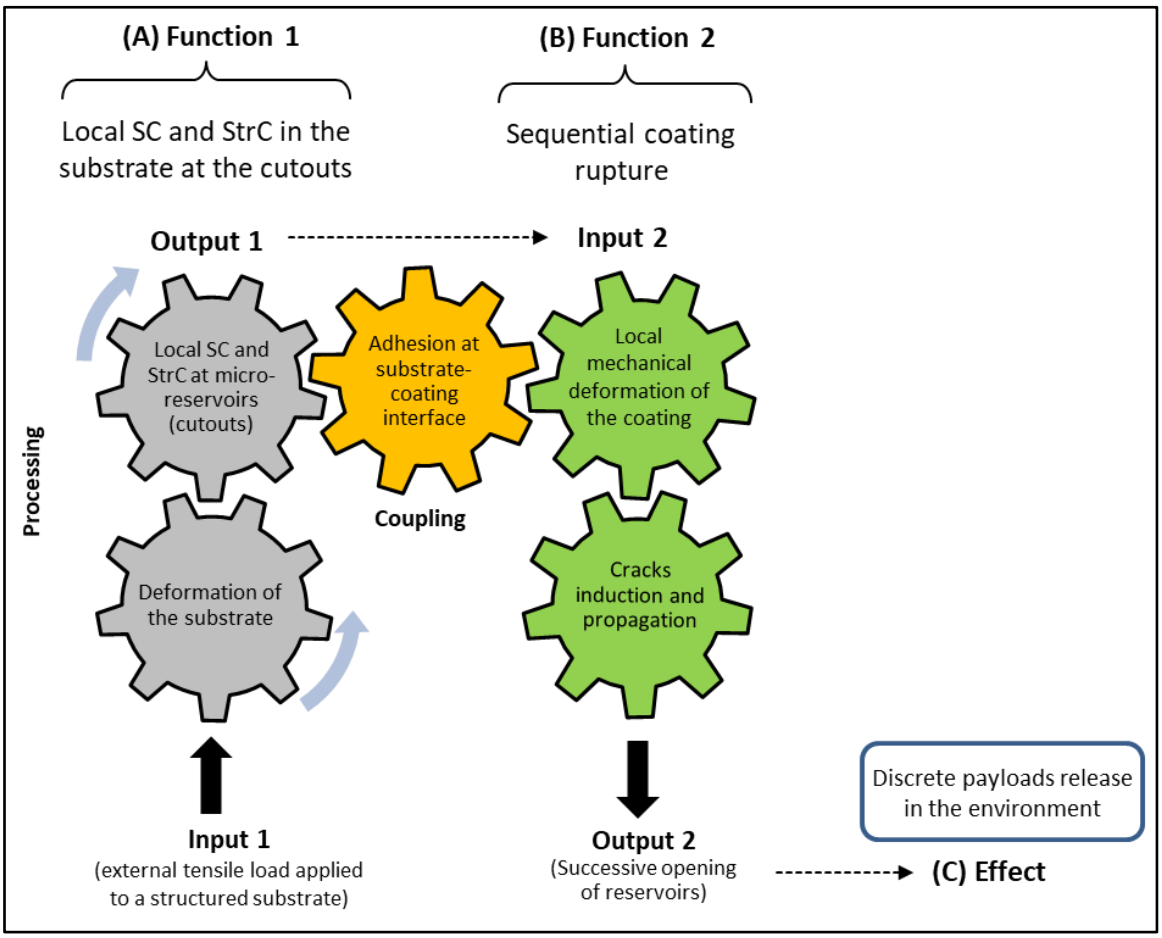

Figure 12. The concept of the multi-functional device with sequentially coupled function 1 (A) and function 2 (B). The concept should allow for an on-demand sequential compound release from a single polymeric substrate structured with micro-reservoirs. Stretching (A, input 1) a substrate with micro-cutouts (reservoirs) should create SC and StrC at sites of the reservoirs (A, output 1). A good adhesion between the substrate and the coating layer (orange gear) should enable transferring the SC and StrC locally from the substrate to the coating layer (output 1 to input 2). Input 2 should cause deformation of the coating at the site of the reservoirs followed by crack induction and propagation leading to a successive opening of reservoirs (output2), which should be translated to the final effect (C) as a discrete payload release from reservoirs.

In order to enable this multi-functional system, the windows of overlapping of output and input (frame conditions) should be considered. In function 1, the nominal stress in the substrate depends on the externally applied tensile load, while the difference of the magnitude of the local SCF and StrCF at the site of reservoirs relies on design parameters of the reservoirs (shape and dimensions). The transition of output 1 to input 2, and thus function 2, depends on the adhesion of the coating to the substrate. Weak interfacial adhesion may cause coating detachment or delamination upon stretching the substrate, which leads to

losing the system functionality. The magnitude of input 2 is related to the magnitude of output 1, while the processing of input 2 to output 2 depends on the coating characteristic (e.g. thickness and mechanical properties). Furthermore, the velocity of output 2 depends on the applied deformation rate in input 1. These input/output frame conditions will be considered and evaluated during the stage of device design for enabling the system functionality.

A schematic diagram of realizing such an on-demand sequential dosing device is shown in Figure 13. As the geometry of the reservoirs determines the magnitude of the concentrated strain and stress, combining different geometrical reservoirs, e.g. circles and rhombuses, in a single substrate should allow distinguishable SCF and StrCF at each reservoir upon deformation of the substrate. A substrate structured with shaped micro-reservoir can be fabricated by using a standard photolithography-replication method (Figure 13 A i-iii) followed by treatment of the substrate for modification of the surface (Figure 13 A iv). Reservoir can be injected individually with different compounds (Figure 13 B i) and then sealed with a polymer layer (Figure 13 B ii). The contact at the substrate-coating interface is a key factor for enabling the system functionality. As the adhesion strength relies on the type of the interaction between the coating and the substrate, a surface modification of the substrate should produce an intermediate layer (Figure 13 B iii) that enables a strong adhesion, preferentially by covalent bonds, which is necessary for transferring the mechanical deformation from the substrate locally to the sealing layer (corresponds to Figure 12, orange gear). As the rhombus reservoir has higher SCF and StrCF than the circular reservoir, subjecting the substrate to a small strain should result in high local concentrated stress and strain at the site of rhombus (Figure 13 C i, corresponds to output 1 in Figure 12), which should transfer locally to the sealing layer and exceed its tensile strength (stress and strain at break) resulting in coating rupture and thus a first compound release (Figure 13 C i). With further stretching, the second dosing should be induced from the circular reservoir (lower SCF and StrCF) (Figure 13 C ii). If the device is operated in a liquid medium as system environment, it will be of particular interest to investigate a discrete and pulse dosing (Figure 13 C iii, corresponds to effect C in Figure 12). Deforming the device by stretching should determine the time of release onset, while the release kinetic may depend on the diffusion coefficient,

the solubility/dissolution of the payload and on the deformation rate as linked to crack propagation.

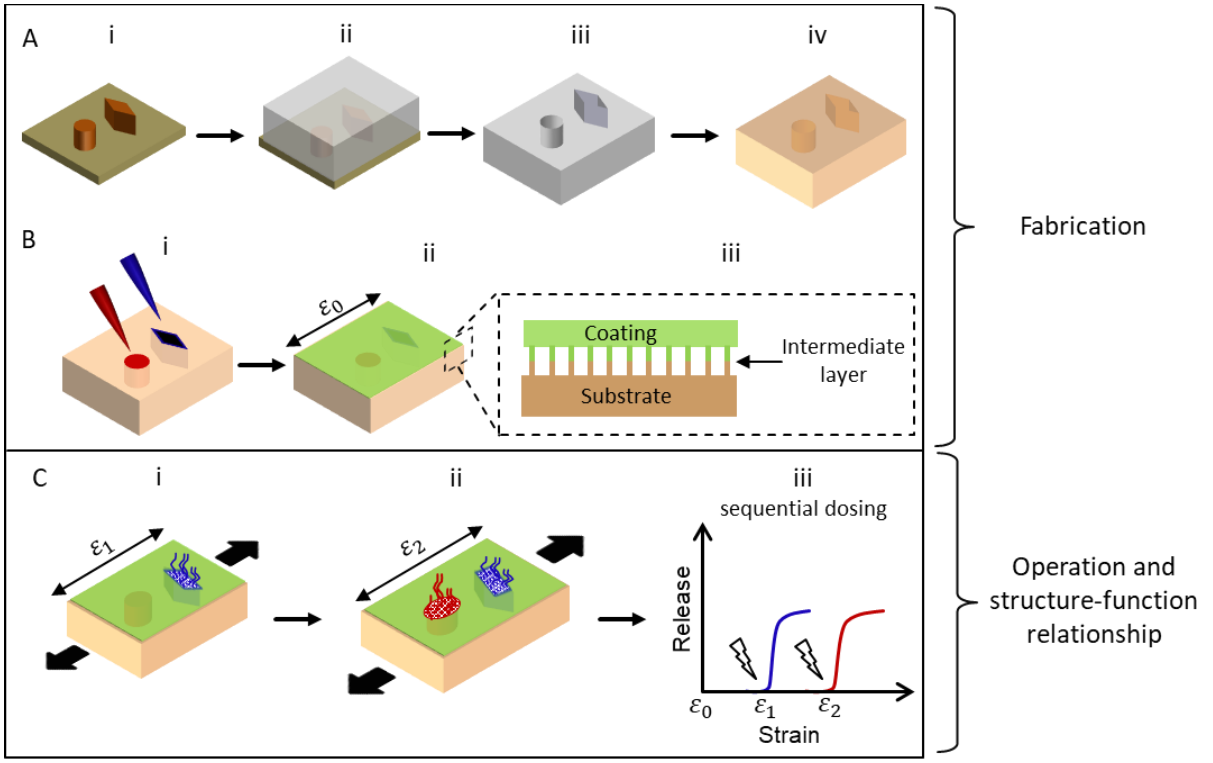

Figure 13. Schematic diagram describes the process for realizing the on-demand sequential dosing device based on the principle of locally concentrated strain and stress at sites of geometrical reservoirs. A i-iii) Fabrication of a substrate with geometrical cavities by the photolithography-replication method. A iv) Substrate treatment for surface modification. B i) Individual loading of reservoirs by micro-injection. B ii) Sealing the geometrical reservoirs with a polymer layer. B iii) A cross-sectional view at the substrate-coating interface, which should provide a strong adhesion, e.g. covalent bonds, for transferring the mechanical deformation of the substrate locally to the sealing layer. C) Illustration of the operation and the structure-function relationship; i) Stretching the substrate should produce at the rhombus cavity high concentration of stress and strain, which should transfer locally to the sealing layer, exceeds its tensile strength and induce sealing breakage leading to the first dosing initiation; ii) Further stretching leading to the second coating failure at the circular cavity and thus to the second dosing. C iii) Corresponded release diagram of the tensile on-demand sequential dosing effect of the device.

Strategy

Evaluation of structure-function relationships and selection of a substrate design (section 4.1)

A key to successfully enable the sequential dosing function based on the principle of stress and strain concentration is understanding the structure-function relationships of the system. Particularly, how do cavities of different shapes, their combination, orientation and different depths in the substrate influence the stress distribution and SCF? In case of sealed cavities, is there a possibility to locally transfer the stress concentrated in the substrate at cavities sites to the sealing layer? How does the coating thickness influence the stress distribution at the

substrate-coating interface? These structure-function relationships will be computationally evaluated by a model based on finite element analysis (FEA). Substrates of different designs will be simulated to estimate the effect of the stress distribution at sites of cavities and at the coating-substrate interface and to quantify the SCF. Using the outcome of the simulation studies, most suitable design parameters for realizing an on-demand sequential dosing system will be defined, a prototype device will be fabricated with the defined reservoir geometries, and its performance will be evaluated experimentally.

Selection of substrate material and reservoir loading approach (section 4.1.2)

In order to allow deformation upon tensile load, a stretchable substrate is required, which also needs to be manufactured to contain micro-sized geometrical reservoirs. To fulfill this requirement, the photolithography technique should be applied that enables the fabricating of precise micro-shapes on a silicon wafer [11]. These micro-structures could be imprinted in a PDMS substrate to be obtained as films with micro-geometrical cavities that are open from top and closed from bottom. Besides, the suitable stretchability of PDMS and its transparency may be beneficial during substance loading and strain-induced release experiment, which may allow visualizing reservoirs from the back-side.

Realizing a multi-dosing of substances requires individual loading of the micro-reservoirs with different compounds. Therefore, a micro-injection technique should be applied for loading cavities with the compounds of interest. This method may allow loading reservoirs precisely and individually, including loading of specific cavity types with different substances. Dyes of different colors will be used as model compounds, which may enable the visualization of the on-demand stepwise dosing

Connective layer and coating materials (section 4.2)

To prevent the pre-stimulation release, the micro-geometrical reservoirs should be sealed with a coating layer. As described previously, the mechanical properties of the coating layer represent an important factor to allow translating the mechanical deformation at the site of cavities to a coating rupture. Therefore, a thin coating layer that is breakable upon application of a small strain would be ideal for the proposed application, as it may facilitate crack initiation followed by coating rupture. Polystyrene (PS), poly(methyl methacrylate) (PMMA) and

poly(cyanoacrylate) (polyCA) materials were considered for the coating based on their low tensile strength (low values of stress and strain at break) [115, 116].

Another important factor that may influence the coupling function is the substrate-coating adhesion as shown previously in Figure 12. The material suggested for the substrate is PDMS, which is a highly hydrophobic material, which may limit the adhesion of the polymer coating on its surface. In order to avoid a possible detachment of the coating, an intermediate layer which increases the binding between the coating and the substrate should be employed. Polydopamine (PDA) was selected for this purpose, since PDA is able to self-polymerize on various materials, including PDMS [117] and PCL [118], and exposing functional groups at the surface. Accordingly, PDA will be harnessed as an intermediate layer between the coating and the substrate, which is assumed to assure a strong adhesion (covalent bonds) by initiation of the polymerization of cyanoacrylate coating materials at the surface of the substrate. This assumption will be examined macroscopically by demonstration experiments. It will also be investigated at the molecular level by x-ray photoelectron spectroscopy (XPS) technique via monitoring the formation of covalent bonds between PDA and polyCA.

Induction of a sequential dosing by local strain and stress concentration (section 4.4)

An experimental setup should be designed to enable exploration and visualization of on-demand sequential dosing function in aqueous environments. To fulfill the requirements of a relevant system environment, studies will be performed in a water bath and under a microscope. For this purpose, a customized miniaturized-tensile setup will be fabricated. The setup should be employed for proof of principle on-demand sequential dosing studies.

For determining structure-function relationship, videos of a high speed microscope-camera will be evaluated to quantitatively correlate the compound release (effect) with the applied strain (input). A sequential initiation of the dosing (one after another) from the shaped cavities in a predefined order (as designed based on their SCF and StrCF) at specific strain values will indicate the feasibility of this concept.

3.2 Self-sufficient thermo-responsive dosing device

Concept

The stretching of bulk materials in one direction results in a reduction of dimensions in the two other directions. In contrast, through a specific device geometry, a biaxial expansion effect of materials with NPR structure can be applied via an in-contact tensile stretching. Conceptually, the creation of NPR skeletons made of a material that can undergo an active movement may enable free standing bi-axially expandable devices, which may be employed as functional multi-reservoirs for an on-demand dosing system. Those devices would be self-sufficiently switchable (neither electronic interfaces nor MEMs), allowing a mechanical opening of coated reservoirs.

For realizing this on-demand dosing system, three individual functions should be coupled: (i) conversion of the external stimulus to an active movement, (ii) biaxial expansion of the device and (iii) translating the mechanical deformation of the reservoirs to a coating rupture in order to obtain the desired effect, i.e., on-demand compound release. Figure 14 illustrates schematically the concept of sequentially coupled functions. In the first step (Figure 14 A), a SMP material will be employed as an actuator, which should enable translating the thermal energy (Figure 14 A, input 1) into a mechanical motion by the SME, i.e. releasing the stored mechanical stress by allowing entropy-elastic recovery of the switching domains as a driving force for the active shape switching (Figure 14 A, output 1). Integrating this molecular switching (output 1) into a polymer skeleton of a suitable 3D design, e.g. NPR design with re-entrant cells geometry (Figure 14 B, input 2), should allow to increase the angles of struts between the NPR-cells. This should lead to a biaxial expansion of the NPR skeleton (function 2) in consequence of the initial thermal stimulation, i.e. an on-demand deformation of the polymer skeleton (Figure 14 B, output 2). The cavities of the NPR skeleton can be employed as reservoirs, which can be loaded with a compound and coated on top. Here, a strong adhesion at the interface of the NPR skeleton and the coating (orange gear) should assure the transition of output 2 to input 3, i.e. the transition of the biaxial expansion of the NPR skeleton to the coating layer. That should cause crack induction and propagation, loss of coating integrity and opening of reservoirs (function 3) via coating rupture, which gives the final effect as an on-demand compound release to the device environment (Figure 14 D).

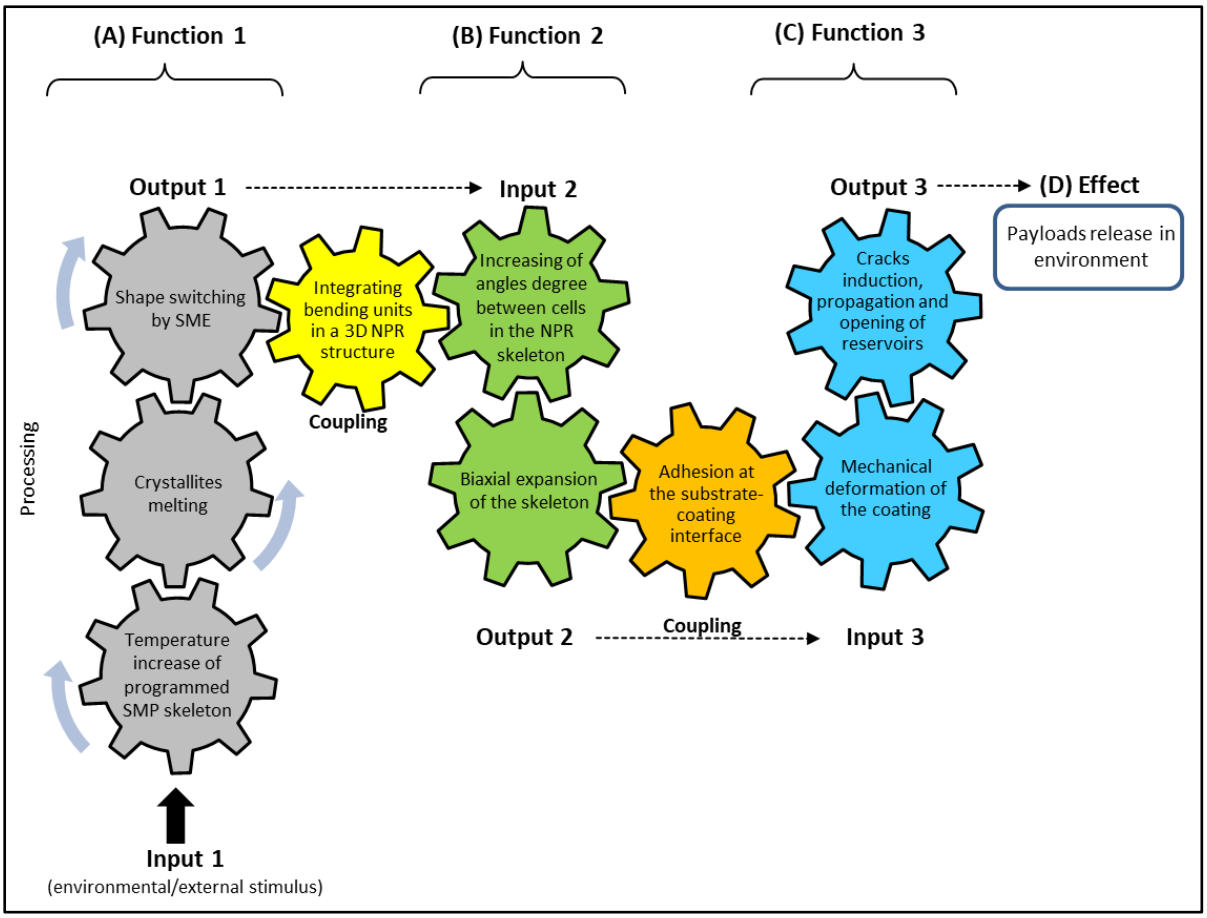

Figure 14. Concept of sequentially coupled functions of the multifunctional device for an on-demand release system. In the first function (A) SMP will be employed as an actuator that responses to the thermal energy of the stimulus by a mechanical motion based on the SME. Applying a heat source (input 1) on the programmed SMP skeleton above the T_{switch} will melt crystalline domains and thus remove the temporary netpoints (allowing segments to move), which facilitates the entropy-elastic recovery (recoiling of the switching domains) as a driving force for the active shape switching (output 1, function 1). Integrating this mechanical energy (yellow gear) in a 3D structure of NPR with re-entrant cells geometry (input 2) leads to the biaxial expansion of the NPR skeleton (output 2) upon the thermal stimulation (i.e. coupling function 1 to function 2). If the cavities of the NPR skeleton are loaded with a compound and coated on top, a strong adhesion at the interface of the substrate-coating (orange gear) assures the transition of the output 2 to input 3. This leads to mechanical deformation of the coating layer, coating disintegration and reservoirs opening due to the coating rupture (output 3, function 3), which gives the final effect (D) as an on-demand compound release in the environment.

Realizing this multi-functional system requires a consideration of the overlapping (frame conditions) of the input and the output. In function 1, the transition from input 1 to output 1 is time dependent as it involves energy provision with a certain heating rate as well as heat transfer within the materials, but also heat loss to the environment. These processes, if properly balanced, should allow reaching the switching temperature of the SMP. The magnitude of the output 1 depends on the characteristics of the used SMP (mechanical properties, extent of programming, shape-fixity and shape-recovery rate). The coupling of

output 1 (shape switching) to serve as input 2 requires an integration of switchable units with a predefined bending movement in specific positions of the polymer skeleton. According to the operation principle of SMP, the device requires introduction and fixation of stress towards a programmed state (here: bended angles). The magnitude of the output 2 (NPR value) depends on the dimensions parameters of the NPR design. Coupling output 2 to input 3, and thus function 3, requires the adhesion at the coating-to-substrate interface and the balancing of strain and force produced during substrate biaxial expansion (related to output 2 + output 1; characteristic of SMP) relative to the tensile strength of the coating. If the coating has a weak adhesion with the substrate, the coating may be detached during operation. If the coating is very flexible, the coating may be stretched rather than ruptured upon device stimulation. These input/output frame conditions will be considered during the stage of the device design and will be evaluated and quantified experimentally for enabling the system functionality.

Building upon the first concept, in this second part of the study, a polymer device of re-Hex-SMP design will be explored for an on-demand self-sufficient dosing system. The process for realizing the dosing system is schematically illustrated in Figure 15. A photolithography-replication method can be used to obtain a re-Hex design mold (Figure 15 A i - iii). The mold can be filled with a polymer network precursor followed by crosslinking, e.g. by UV light. Isolating the sample from the mold should make the desired SMP skeletons accessible (Figure 15 B i - iii), which should be able to store mechanical stress and release it upon stimulation. Then, the obtained skeleton can be treated for surface modification (Figure 15 B iv) to assure coating fixation on the skeleton. For implementing the SME, the skeleton should be programmed to a compressed state by a suitable technique (biaxial dimension reduction, Figure 15 C i-ii). The cavities can be filled with a compound followed by sealing from both sides (Figure 15 C iii - iv). Here, the modified surface of the skeleton should allow a strong adhesion at the interface of the coating and the device, which is required to assure the transfer of the mechanical deformation of the device to the coating layer.

The structure-function relationships in this system relies on three hierarchical levels. At the molecular level, a proper polymer network architecture should provide suitable mechanical and thermal properties to enable the system operation. At the morphological level, the crystalline domains of the polymer should enable the fixation of the temporary shape, i.e.

form temporary netpoints, which are necessary to create the SME that acts as a driving force in this system. Building on extensive knowledge of literature [119, 120], a basic characterization of the structures on these two levels will be performed. At the macroscopic level, the NPR design of the device, should allow an biaxial expansion (Figure 15 C iv - v), in which the generated strain (ε) and the shape-recovery force (F_{rec}) must exceed the tensile strength (strain and force at break, ε_B and F_B) of the coating layer leading to rupturing of the coating layer (Figure 15 C v) and thus a payload release. Operating such a system in an aqueous medium should allow for an active bolus release in a non-contact (Figure 15 C vi) mode from a polymer-only device, where the on-demand actuation of the device by increasing the medium temperature should determine the time of the onset of the bolus dosing.

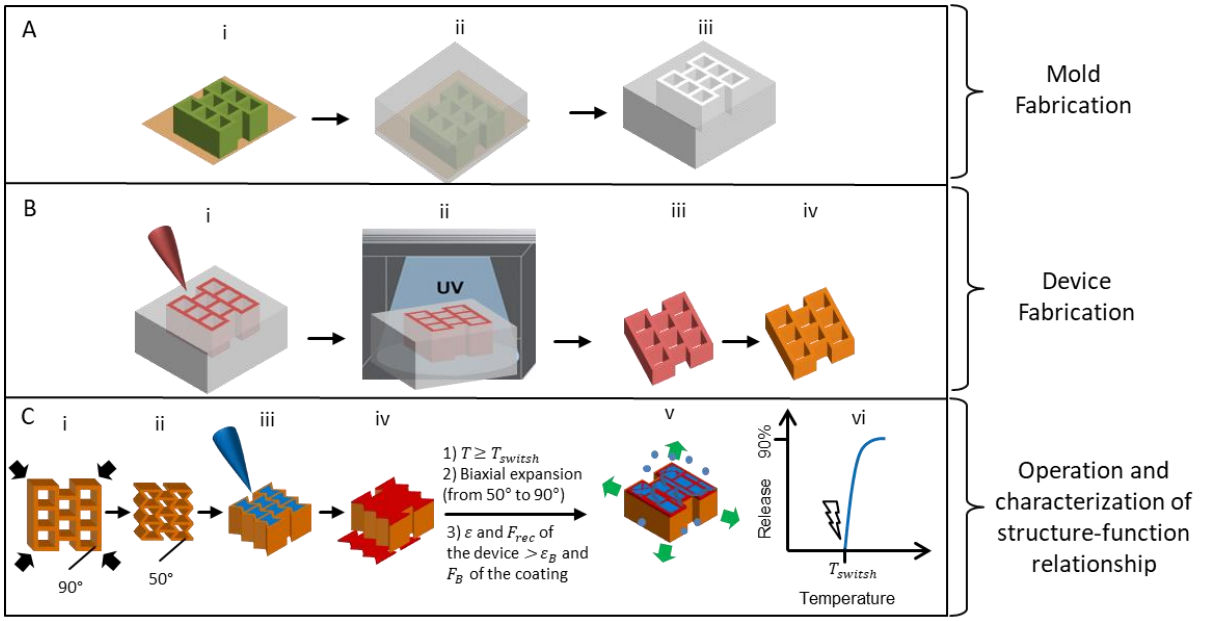

Figure 15. Schematic illustration of the process for realizing a thermosensitive self-sufficient cargo releasing device for an on-demand dosing based on the concept of the sequential coupling functions. A i-iii) A re-Hex mold can be obtained by the photolithography-replication method. B I - iii) The mold filled with a polymer precursor, followed by crosslinking and isolating the sample as SMP-skeleton. B iv) Surface modification of the SMP-skeleton by sample treatment. C I - ii) Implementing the SME by programming the SMP-skeleton (from e.g. angles of 90°) to a compressed mode for biaxial dimensions reduction (e.g. to angles of 50°). C iii - iv) loading the cavities with a compound then coating from both sides. C v – vi) Upon thermal stimulation of the device, force (F_{rec}) and strain (ε) will be recalled by the SME and the biaxial expansion of the device will be induced, which should transfer to the coating layer, exceeds its tensile strength (ε_B and F_B) and induces coating rupture, which allows a bolus compound release from reservoirs.

Strategy

Design parameter and structure-function relationships of re-entrant hexagonal structure (sections 5.1)

Enabling a thermosensitive with sufficiently moving could also be a cargo releasing device for an on-demand dosing system. Such a system requires a design that can accomplish both, carry a cargo and being able to produce a change in dimensions, e.g. by expansion, upon stimulation. By selecting structure capable of NPR behavior, these requirements should be fulfilled considering their porous structure and their ability of biaxial expansion. Particularly, re-entrant hexagon (re-Hex) structures are typically associated with a high magnitude of NPR compared to other designs (see Figure 5) and provide large cavities that may serve as reservoirs.

The shape deformation of the skeleton is required to produce a strain and force that should exceed the tensile strength (strain and force at break ε_b and F_b, respectively) of the coating layer. In order to realize the proper skeletons that fulfill this requiem, it is necessary to understand the effect of different design parameters, e.g. angle degree, wall length and thickness and substrate depth, on the produced strain, force and surface area alteration during the skeleton deformation. These structure-function relationships will be evaluated theoretically by applying the hinge model [52]. Accordingly, the most suitable skeleton design will be identified and fabricated from a polymeric material.

SMP as a temperature-responsive material of the device (section 5.2.1)

In order to enable an externally inducible dosing function from a self-sufficient device, the device should be capable of storing the mechanical stress and providing an active mechanical movement upon stimulation. Therefore, a temperature-responsive SMP was selected as device material, which translated a thermal energy to an active and predefined bending movement.

PCL was selected as a matrix material based on its slow degradability, which may be beneficial in terms of lifecycle management, and its hydrophobicity, which is preferred to avoid swelling in aqueous environment [121]. In order to obtain a network structure as required for realizing the SME, linear oligo(*ε*-caprolactone) [oCL] (8 KDa) was selected as a starting material due to its ability to form covalent semi-crystalline networks with a shape-memory effect with T_{switch}

slightly above the body temperature at high recovery rates [122]. oCL functionalized with IEMA end groups will be used as cross-linkable precursors, which should produce covalent network structures that serve as permanent netpoints defining the permanent shape. The network properties will be characterized by FTIR spectroscopy, swelling degree and gel content tests. The thermal properties will be characterized by DSC.

Stress introduction and storage in the device (programming process) (section 5.2.3)

In order to store a mechanical stress in the re-Hex-SMP device, a SME should be implemented by a programming process. Since a biaxial expansion is desired to rupture the coating over the reservoirs, the device should be programmed to a compressed state through a biaxial compression. For this purpose, a suitable programming method should be established and applied, which provides a controlled deformation by bending the walls of the device and changing the angles degree, whereas uncontrolled buckling should be avoided. Aided by templates to achieve specific temporary shape, the effect of programming on the shape switching function will be characterized. Inserting a re-Hex-SMP skeleton of, e.g., α = 90° in a PDMS mold of, e.g. α = 60°, then heating to $T>T_m$ followed by cooling to room temperature, and eventually isolating the skeleton from the PDMS mold should produce a programmed re-Hex-SMP skeleton with defined angles degree (e.g., in this case programmed angles of 60°). As the extent of programming (compressed skeleton) may influence the system function, the effect of the programmed angle degree of the skeleton on the surface area reduction, shape-recovery force and strain during the shape-recovery of the skeleton will be evaluated experimentally and will be compared with the mechanical properties of the coating layers. The SME properties will be characterized by calculating the shape-fixity rate, shape-recovery rate and determining the switching temperature.

Characterizing the shape-recovery force of re-Hex-SMP skeletons (section 5.2.5)

For coupling the functions of biaxial expansion function and disintegration of reservoir coating, suitable forces need to be created and transferred to the coating. Typically, in literature, the presented characteristics for shape-recovery of SMP is the recovery stress (stress = force/cross-section area) as the majority of the examined SMP samples are standardized to have a regular cross-section, as in the case for e.g. a film shaped sample. In this study, however, the device level is addressed. Here, the examined SMP samples have a

re-Hex design, which is composed of aligned cavity-cells (irregular cross-section area) and are programmed to a shape of reduced biaxial dimensions by simultaneously bending of several walls to a predefined angle degree. Therefore, in this study, the analysis on the device level will result in a shape-recovery force, which is defined as the force generated during thermal-induced shape-recovery (i.e. thermally-induce biaxial expansion) of the re-Hex-SMP skeletons. In order to investigate the effect of the programmed angle degree on the shape-recovery force, re-Hex-SMP skeletons will be programmed to a different angle degree and the force during shape-recovery will be measured experimentally as described in section 5.2.5.

Intermediate layer and device coating (section 5.3)

After programming and loading of the re-Hex-SMP skeleton with a substance of interest, a challenge is coating the skeleton in the programmed state as the coating process should not swell the skeleton nor induce the SME. Furthermore, the coating layer should be instantly formed and adhered to the skeleton. To fulfill these requirements, polyCA will be used as the coating material and PDA will be employed as intermediate layer to assure a good binding between the coating and the device (justified previously in section 3.1). Additionally, the coating parameters relationship between the number of coating cycles (number of times the sample was coated) and the overall thickness of the coating will be investigated. The impact of the polyCA side chains on the mechanical properties of the coating will be studied.

In-situ analysis of mechanical properties of coating layers (section 5.4)

Since the coating connected to the re-Hex-SMP skeleton should be a thin film, which is breakable by purpose, isolating the coating layer for determining the mechanical properties by conventional methods, e.g. in a tensile tester, is not possible. Alternatively, an in-situ micro-indentation method may be applied, which may allow for a non-destructive determination the mechanical properties of the coating. The micro-indentation test can be performed directly after the coating formation on the device without a need for coating isolation.

Structure-function relationship and overall device functionality (section 5.5)

Based on the individual features such as the recovery force of the skeleton, the force at break of the coating and the substrate-coating interface (covalent bonds), the coupling of the individual functions will be theoretically and experimentally evaluated. The structure-

functions relationships will be evaluated and quantified at the molecular-, micro- and macroscopic level by the previously described analysis. The data as obtained will be compared and the most suitable design parameters and coating material will be selected. For experimental confirmation, individual programmed re-Hex-SMP skeletons will be coated with different polyCA coating materials. Devices will be placed in an aqueous medium, the temperature will be elevated, the shape-recovery will be induced under the microscope and the experiments will be recorded as high speed videos. From the videos, the coating breakability and the characteristics of the coating rupture will be analyzed.

The triggered release function will be evaluated by employing cavities of programmed re-Hex-SMP skeletons as reservoirs, which will be loaded with a compound followed by coating the device from both sides with polyCA material by in situ polymerization of CA monomer solution. A dye will be used as a model compound for visualizing the release upon the device stimulation. The device will be placed in a water bath, the temperature of the solution will be increased and the experiment will be recorded as a video form which images can be extracted. From the images, the structure-function relationship of the device will be characterized and quantified. The onset of the device switching will be correlated to the applied temperature and the order of cavities opening will be monitored. Successful release will be indicated by the presence of the colored cargo in the solution, which can be quantified.

Chapter 4 Stress concentration in micro-structured materials for a sequential dosing function

4.1 Evaluating the structure-function relationships of the system

According to the strategy (in section 3.1), realizing a sequential dosing function from micro-structured polymeric substrates based on the principle of the stress and strain concentration requires an understanding, how the different design parameters may influence the function of the system? That includes the structuring of the micro-scaled cavities, the interface between substrate and coating as well as the dimensions and physicochemical characteristics of the coating layer. These structure-function relationships will be investigated in the following sections.

4.1.1. Evaluating design parameters for stress concentration by finite element analysis

4.1.1.1. Design description of substrates with micro-scaled cavities

In a computer-assisted approach, finite element analysis (FEA) was performed on substrates, which have different types and orientations of cavities. The evaluated geometrical shapes and their dimensions are shown in Figure 15 A. All cavities are placed in an area of 10 mm x 5 mm, denoted as the structured area (Figure 15 B). The overall substrate is designed with a length of 20 mm to allow for a space as needed in case of experimental application to fix the sample at its application site or in an analytical instrument, e.g. tensile tester. In the FEA, the substrate was defined as a silicon rubber, which has mechanical properties (shown in Table 1) that is very similar to the PDMS material (E ≈ 2.5 MPa, shear modulus ≈ 0.7 MPa , tensile strength ≈ 6 MPa [123]), which will be used as substrate for the experimental validation.

In order to investigate the effect of cavity shapes, orientation, depth, and their arrangement in the substrate on the stress distribution and the SCF, the structured area in the substrate is considered with three individual designs (Figure 15 D):

- Design 1: substrates contain cavities of identical shapes aligned in a vertical row, i.e. substrates with either only cavities of rectangles, only circles, or only rhombuses (Figure 16 D, left).
- Design 2: substrates composed of two types of cavities that are aligned in two parallel vertical rows (Figure 15 D, middle).

- Design 3: substrates containing cavities of several shapes (Figure 15 D, right).

The cavities are opened from the top and closed from the back side (Figure 16 C). The depth of the substrates ($D_{substrate} = 0.5$ mm) is here set to be constant, while cavities of various depths are considered and analyzed in section 4.1.1.3. As the concept of the study bases on the principle of stress concentration, all geometrical cavities were designed to exhibit identical surface areas (and volumes) to eliminate their effect on the SCF.

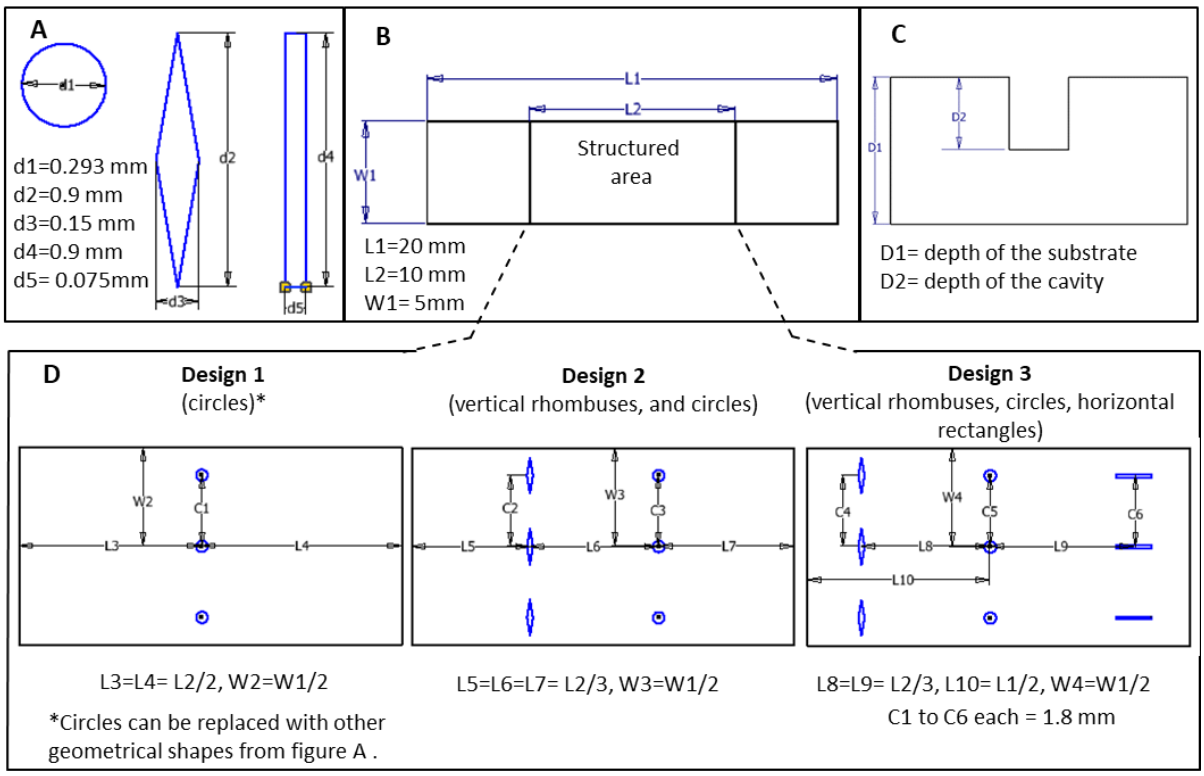

Figure 16. Schematic view of investigated designs. A) The geometrical shapes and dimensions of intended cavities. From left to right: circle, rhombus and rectangle. B) Top view of the substrate. The cavities will be imprinted in the area denoted as the structured area. C) Schematic side view of a cavity imprinted in the substrate. D) Exemplary dimensioning of the structured area as a magnified top view of three designs. Design 1: the structured area contains cavities of identical shapes aligned in a vertical row. Herein showed as circles, which can be substituted with rhombuses or rectangles of different orientation. Design 2: the structured area contains two types of geometrical cavities; left vertical rhombuses and right are circles cavities. Design 3: the structured area contains multiple types of geometrical cavities; right: vertical rhombuses, middle: circles and left: horizontal rectangles.

4.1.1.2. Evaluating the stress concentration factor of different geometrical cavities

In the first step, the stress concentration has been evaluated in a scenario for non-coated substrates containing different types of geometrical cavities. The stress concentration was investigated in the linear elastic range. In each design, the surfaces of the substrates and the cavities had a local elemental mesh size of 0.1 mm (experiment detail in 7.2.1). In each design

(1, 2 and 3), the substrate is constrained from the left side and subjected to a tensile load of 0.1 Newton (N) from the right side. Under the applied load, the von Mises stress intensity, which corresponds to the stress distribution in 3D (multi-axial stress state), is visualized at sites of each geometrical cavity as shown in Figure 16.

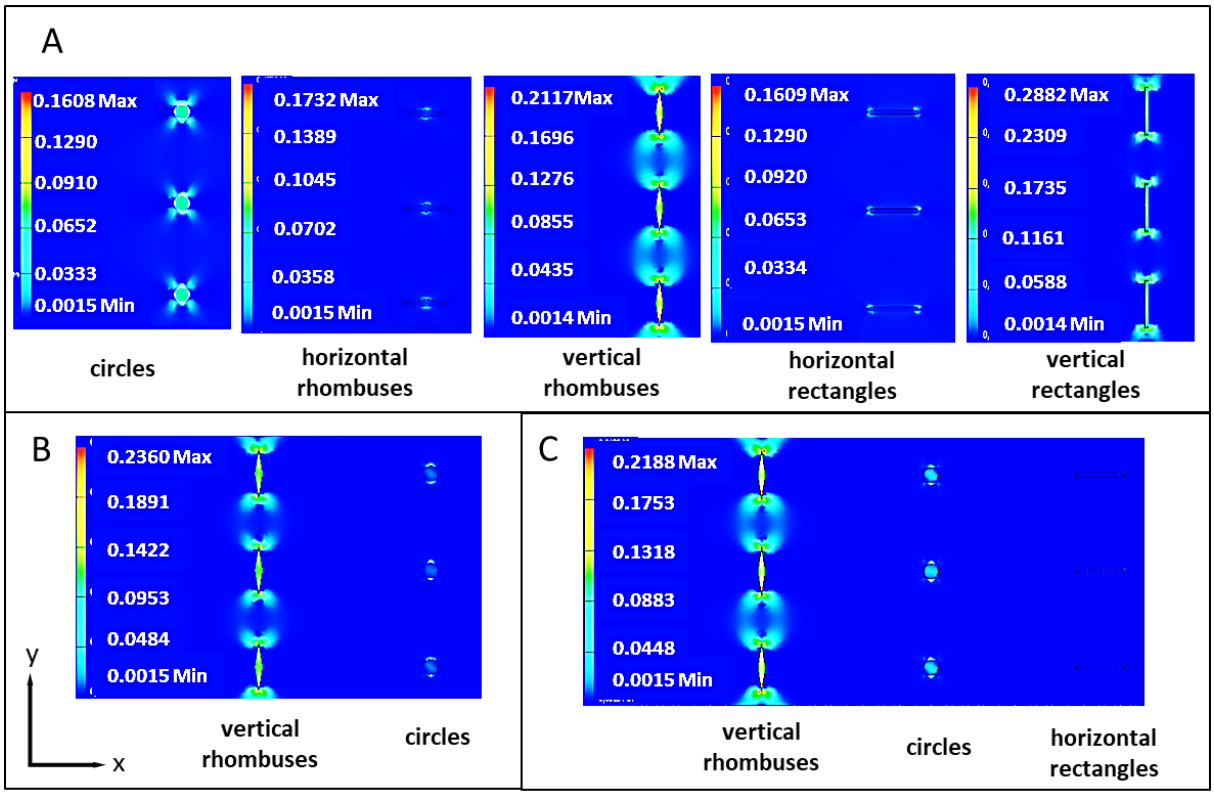

Figure 17. Von Mises stress analysis by FEA in substrate structured with micro-scaled cavities of different shapes under an uniaxial tensile load in x-direction. A) Substrates of design 1. From left to right, cavities shaped as circles, horizontal rhombuses, vertical rhombuses, horizontal rectangles and vertical rectangles. B) Substrate of design 2. Left: vertical rhombuses cavities and right circles cavities. C) Substrate of design 3. Left: vertical rhombuses cavities; middle: circles cavities; right: horizontal rectangles cavities. The applied load is 0.1 N. The colored scale bar represents the stress intensity (unit: MPa). For each FEA experiment n = 1.

The SCF of the geometrical cavities for the three models of Figure 17 was quantified (according to Equation 3) and represented in Figure 18. Substrates of design 1 showed that circle cavities displayed a SCF of 2.7, while horizontal rectangles and rhombus cavities exhibited a similar SCF of 1.5. Interestingly, a reorientation of the rectangular and rhombus cavities to a vertically direction elevated the SCF to 7.2 and 5.2, respectively. This increase in the SCF may be explained by their long axes being perpendicular to the direction of the applied load, which produces higher SCF as described by Equation 4 (compare section 1.2). Interestingly, when different types of geometrical cavities are combined in a substrate, as for designs 2 and 3, the order of the SCF has not been impaired, rather each type of geometry kept its initial range of SCF as shown in Figure 18. For instance, in case of model 2, the rhombus cavities displayed

higher SCF than circular cavities (SCF = 5.2 and 2.5, respectively). Furthermore, in case of multiple types of geometrical cavities in a substrate as for design 3, rhombus cavities displayed the highest SCF of 5.2, followed by circles with SCF of 2.5 and SCF of 1.5 for rectangles cavities (Figure 18).

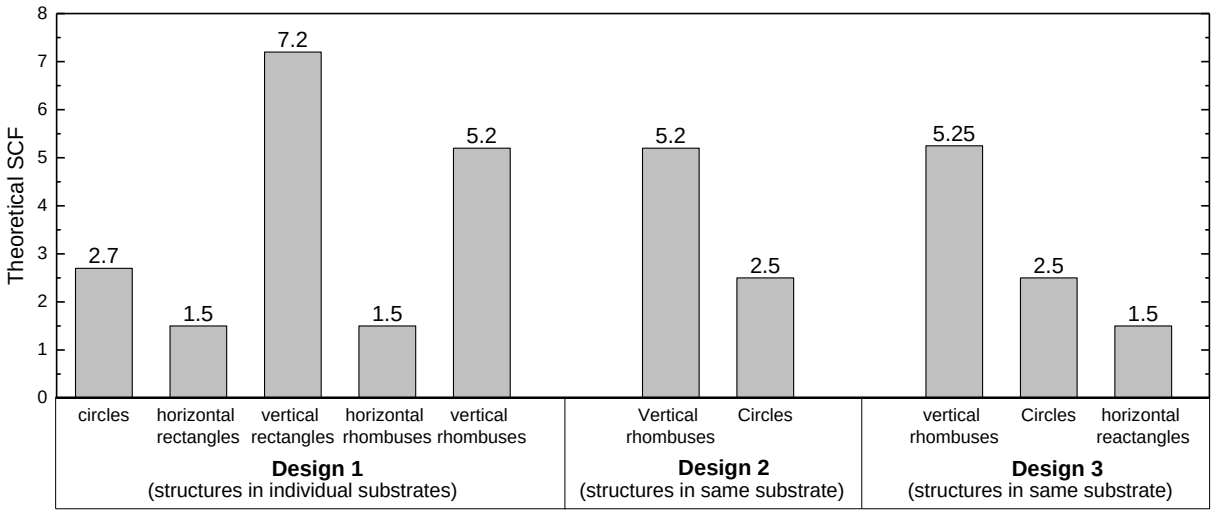

Figure 18. Theoretical SCF values at each geometrical cavity in the substrates of the different designs of Figure 17. From the FEA analysis, stress value at site of cavities was detected and applied in Equation 3 for calculation the theoretical SCF.

4.1.1.3. Effect of cavity depth on stress concentration factor

Design 2, which exhibited distinguishable values of SCF among the two shaped cavities, was selected for evaluation the effect of cavity depth (D_{cavity}) on the SCF. Different substrates of a constant thickness ($D_{substrate}$= 0.5 mm) with D_{cavity} ranging from 0.05 to 0.45 mm were computationally analyzed. The data are represented as a ratio of D_{cavity} to $D_{substrate}$ as shown in Figure 19, where D_{cavity} / $D_{substrate}$= 0 refers to the absence of any cutout in the substrate, while D_{cavity} / $D_{substrate}$ = 1 corresponds to a hole (cavity opened from both side). Data indicated that increasing the ratio of D_{cavity} / $D_{substrate}$ (increase the depth of cavities) elevates the SCF. For rhombus cavities, increasing D_{cavity} / $D_{substrate}$ from 0.1 to 0.9 increased the SCF from 1.9 to 5.5, respectively. Furthermore, this analysis showed the effect of D_{cavity} on the SCF. When cavities of circles and rhombuses both had D_{cavity} / $D_{substrate}$= 0.1, they concentrated the stress at close range (1.7 to 1.9, respectively), while the rhombus cavities concentrate the stress two fold higher than circular cavities when increasing D_{cavity} / $D_{substrate}$ to 0.9. Such a behavior can be fully attributed to the effect of geometrical shapes and orientation as all cavities had the same top surface areas and volumes.

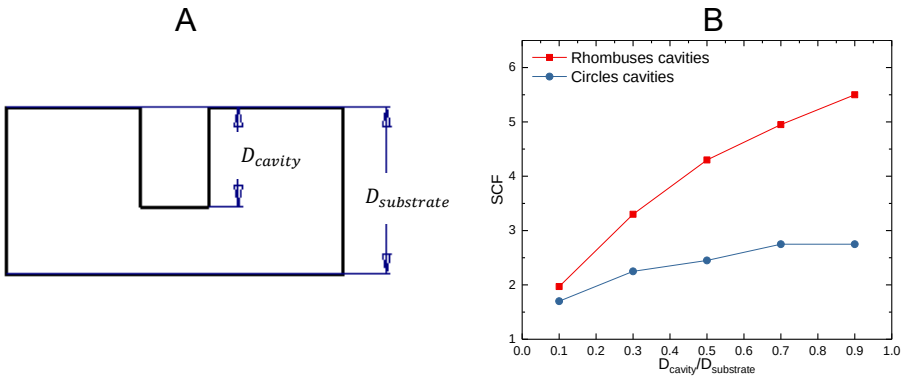

Figure 19. Effect of cavities depth in the substrate on the SCF analyzed by FEA. A) Schematic side view of a cavity imprinted in the substrate. D_{cavity} and $D_{substrate}$ refer to the depth of the cavity and the thickness of the substrate, respectively. B) Effect of depth of cavities on the SCF in substrates of design 2 (see Figure 16 D). X-axis represents the ratio of cavity depth and substrate thickness (D_{cavity} to $D_{substrate}$). Here, $D_{substrate}$ is constant = 0.5 mm. D_{cavity} is variable from 0.05 mm (D_{cavity} / $D_{substrate}$= 0.1) to 0.45 mm (D_{cavity} / $D_{substrate}$= 0.9). By FEA, each substrate was subjected to a uniaxial (x-direction) load = 0.1 N, von Mises stress value at site of cavities was detected and applied according to Equation 3 to calculate the SCF, which represent the y-axis in the graph b.

4.1.1.4. Evaluating the transfer of local stress from substrates to coating layers

A particular interest in this study is to computationally analyze the stress in coated substrates. This analysis should indicate if the local stress in the substrate may transfer into an alteration of the coating layer assuming prefect attachment. In such a system, the breakability of the coating will depend on the mismatch between the mechanical properties of the coating layer and the substrate, i.e. a stiff coating layer on a ductile substrate. The focus will be on stress distribution at the interface between the surface of the cavities and the coating layer. Coated substrates of design 2 were selected due to the distinguishable SCF of the geometrical reservoirs as concluded above from FEA. Poly(n-butyl cyanoacrylate) was simulated as a coating layer by implementing the mechanical properties of the substrate and the coating layer in the model as given in Table 1

Table 1. The mechanical properties of the substrate and the coating layer used in computational study.

Materials	E modulus (MPa)	Shear modulus (MPa)	Yield strength (MPa)	Tensile strength (MPa)	Poisson ratio
Substrate (silicon rubber)[(a)]	3	1.007	10.340	6.5	0.49
Coating (PBCA)	8000 [(b)]	0.125 [(c)]	0.79 [(c)]	0.9 [(c)]	0.4 [(d)]

(a) Mechanical properties were applied from the material library of the FEA software (AutoCAD inventor).
(b) Measured experimentally from section 5.4.
(c) From reference [124]
(d) From reference [125].

Herein, it is assumed that the coating layer covers only the structured area over the cavities. A uniaxial tensile load is applied on the substrate in x direction. After loading (0.1 N), the coating layers were isolated by the FEA software for visualizing and quantifying the von Mises stress at the interface. When the coating thickness is 1 µm, a locally concentrated stress appeared both at the interface facing the substrate and at the surface of the coating, i.e. transferred through the coating material as desired (Figure 20 A, top image). The interface of the coating displayed a higher local stress, which was concentrated at sites of geometrical cavities (Figure 20 A, bottom image). When the coating thickness was increased to 15 µm, the local stress was clearly reduced at the surface of the coating as well as the coating-substrate interface (Figure 20 B). The effect of the coating thickness on the SCF at the interface of coated and stretched micro-structured substrate is summarized in Figure 20 C. The SCF was here quantified based on the von Mises stress in the coating layer (not in the substrate). When the coating has a 1 µm thickness, the areas at the coating interface over the rhombuses and circles cavities displayed distinguishable SCF of ≈ 1.7 and 1.3 respectively. When the thickness increased to 15 µm, the SCF in areas over geometrical reservoirs appear to be equally ≈ 1.1 for rhombus and circular cavities. The reduced stress and SCF by increasing the coating thickness (when the applied force is constant) may be attributed to the increased cross-section area, which leads to lower force distribution per area and thus reduces the stress according to Equation 2.

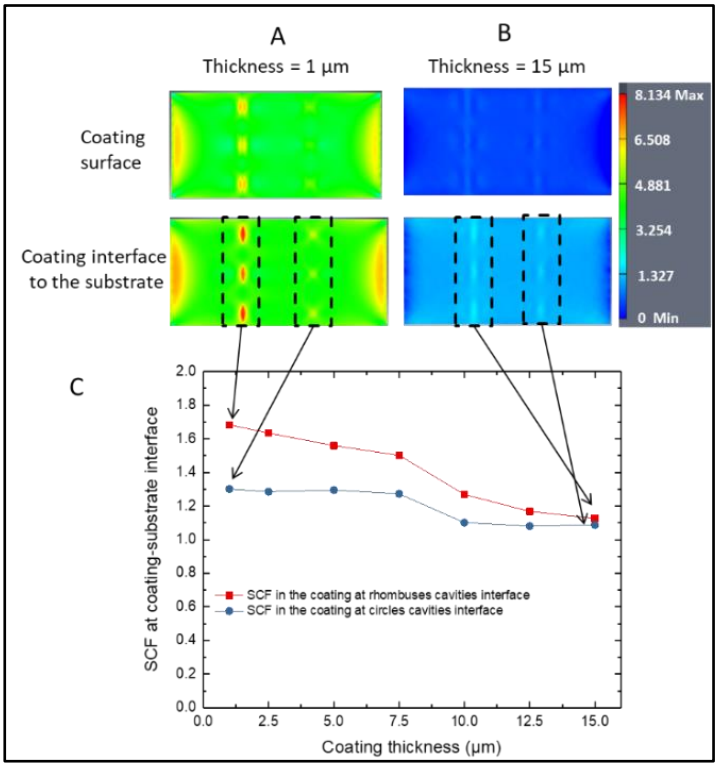

Figure 20. FEA of Von Mises stress in coating layers above substrates of design 2 (vertical rhombuses and circles cavities as in Figure 16 D) coated with PBCA. A) 1 µm coating thickness and B) 15 µm coating thickness. The colored scale bar represents the stress intensity (unit: MPa). Dashed squares indicate the area with local concentrated stress at interface over geometrical cavities. C) Effect of coating thickness on SCF at coating interface at sites of geometrical cavities. SCF quantified based on the stress in the coating layer.

The results indicated that the stress at the substrate-coating interface is higher than the stress at the coating surface. This is in line with the literature [126, 127], whereas evidence was given that in systems of stiff film supported on a non-structured ductile substrate, the cracks were initiated from the interface and propagate to the surface of the coating layer. Interestingly, an additional significant finding in the current exploration was that the raised stress at geometrical reservoirs in the substrate transferred locally with different magnitudes to the coating layer. The magnitude of the stress at the coating-substrate interface is found to be higher over non-circular cavities of a higher SCF, i.e. the stress in the coating at the interface over the rhombuses cavities is higher than over the circular cavities. This finding indicated conceptually that the coating layer will break sequentially first at the site of the rhombus reservoirs (high SCF) and then at circular reservoirs (low SCF), which supports the initial hypothesis.

4.1.2. Experimental evaluation of the strain concentration in substrates with micro-scaled cavities

Fabrication of substrates structured with micro-geometrical cavities

A soft photolithography replication method was employed to experimentally obtain micro-structured substrates as previously explored by FEA. PDMS was selected as a model material for substrates as it fulfills the requirements of high elasticity and transparency for monitoring the dosing initiation from the samples' back side. Briefly, the microstructures were templated from photoresins deposited on silicon wafers and subsequently illuminated through a foil mask. Those hardened structures served as negative template to be replicated in PDMS for obtaining substrates with the desired cavities (experiment detail in 7.2.2). The obtained PDMS substrates had average dimensions of 20 ± 0.1 mm length, 5 ± 0.1 mm width and 0.500 ± 0.09 mm thickness (n = 3). The cavities, which are opened from the top and closed from the backside as shown in Figure 21 B, were prepared with an average depth of 0.350 ± 0.05 mm (n =3), i.e. a ratio of $D_{cavity} / D_{substrate}$= 0.7 selected corresponding to a high SCF (compare Figure 19). The circular cavities exhibited a surface area of ≈ 8500 ± 55 µm^2 (n = 3), while rhombus cavities had a surface area of ≈ 9000 ± 200 µm^2 (n = 3).

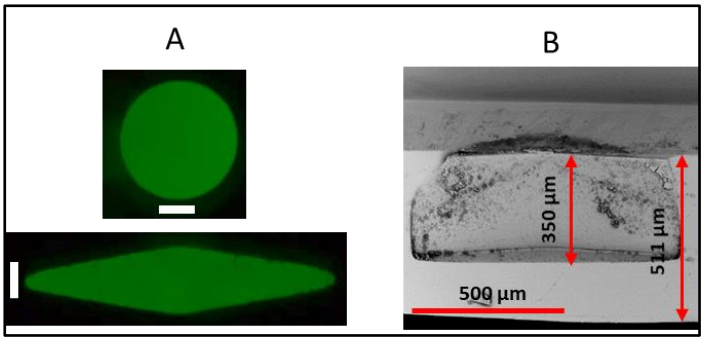

Figure 21. A) Top view of micro-geometrical cavities obtained as reservoirs in a PDMS substrate and loaded with a fluorescent dye (fluorescein sodium) to enhance the visualization of their boundaries. Top is a circle cavity; bottom is a rhombus cavity. Scale bar is 100 µm. B) SEM images at a cross-section of a rhombus cavity.

Experimental evaluation of strain concentration factor

In this part, the influence of cavity shape and orientation on the StrCF has been evaluated experimentally. For the fabricated substrates of design 1, 2 and 3, the StrCF for cavities was calculated according to Equation 5. The ε_{local} of each geometry is calculated based on the change of its width during stretching compared to its initial width as shown in Figure 22.

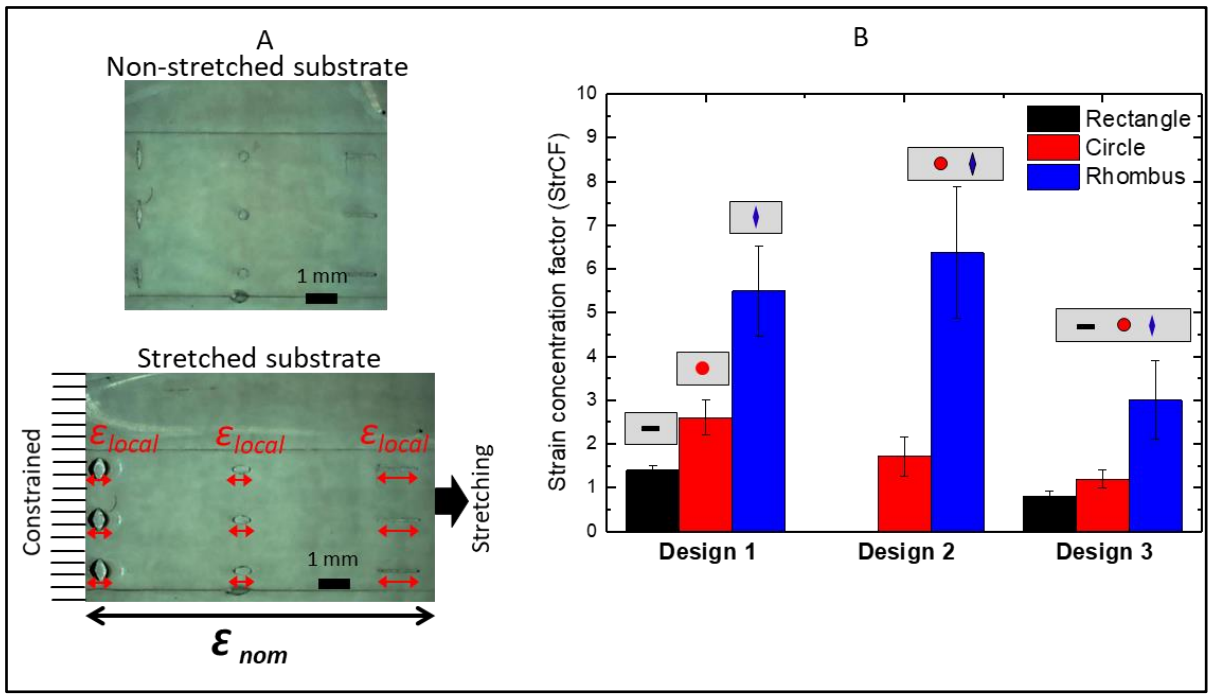

Figure 22. A) The principle of strain concentration. Top: PDMS substrate before stretching, which combines three geometrical cavities (from left to right: vertical rhombuses, circles and horizontal rectangles). Bottom: Stretched PDMS substrate ($\varepsilon_{nom} \approx 60\%$), indicating the local strain at each cavity (red arrows). B) Stretched substrate, experimentally determined strain concentration factor depending on different shapes of cavities and their combinations. StrCF calculated according to Equation 5. Data represented as mean ± SD (n = 3).

Results showed that in case of design 1 with single shapes only, the vertical rhombuses exhibited the highest experimental StrCF followed by circles and horizontal rectangles. In case of two types of cavities in a substrate (Figure 22 B, Design 2), the strain is highly concentrated at rhombus cavities as expected (StrCF = 6.3 ± 1.5; n = 3), while it is reduced at the circular

cavities (StrCF = 1.7 ± 0.4; n = 3) also compared to the data obtained for design 1. Combining all three types of cavities together in a substrate (Figure 22 B, Design 3) resulted in lower StrCF for all geometries, which may be attributed to a distribution of the applied strain among the cavities that reduced the concentrated strain for each of them. However, despite reduction of StrCF values, the order of StrCF is not affected, i.e. vertical rhombuses remained the shape of the highest magnitude with StrCF = 3 ± 0.9, followed by circles with StrCF = 1.2 ± 0.2 and then horizontal rectangles with StrCF = 0.8 ± 0.1.

In general, these experiments emphasized the effect of the type of geometrical cavities and their placement in flexible substrates on the strain concentration behavior. The results indicated that in addition to the stress concentration, also the local strain can be enhanced at the site of cut-outs. Despite the behavior of StrCF has before been studied in perforated substrates of low stretchability [128, 129], e.g. metal plates, the effect of differently shaped micro-cutouts in polymeric substrates on StrCF has not been addressed. In this study, by examining PDMS substrates (having a high stretchability) structured with cavities on the micrometer size range, the influence of cavity shape on the strain concentration was obvious and the StrCF could be experimentally quantified.

Based on these results and the previous FEA analysis, it can be concluded that placement of cavities in a polymeric substrate can be used as cues to direct the stress and the strain to specific sites, whereas the magnitude of SCF and StrCF can be modulated by the shape, depth and orientation of cavities. Cavities of anisotropic shapes, which have their long axes perpendicularly oriented to the direction of the applied tensile load, exhibited a high SCF at the surface. This result are in agreement with literature [22, 130], where the stress concentration under a tensile load was studied theoretically and experimentally in metal or resin plates perforated by holes. Additionally, this study explored substrates with combinations of differently shaped cavities in a single substrate. It was demonstrated (in respect to the given dimensions of the substrates designs) that combining two types of geometrical cavities, e.g. vertical rhombuses and circles (design 2) in a substrate does not affect the order of SCF and StrCF and gives a different magnitude at each type of cavity. Moreover, deeper cavities in the substrate (increasing the ratio of $D_{cavity}/D_{substrate}$) increased the magnitude of SCF. These findings have an important implication suggesting that the distinguishable values of SCF and StrCF in design 2 might enable the desired sequential

on-demand dosing initiation through function-function coupling. Therefore, this design was selected as a prototype device for further experimental investigations of coated systems.

4.2 Connective layer and substrate coating

According to the strategy (section 3.1), the geometrical reservoirs should be sealed with a polymer coating layer that is breakable upon stretching. In this context, two issues need to be considered:

1) The coating film should be breakable at a small strain. Therefore, a coating polymer with a low value of strain at break (ε_B) should be used. A polymer of a high T_g is preferred, where the coating is in the glassy state during stretching. Furthermore, a low coating thickness of a few micrometers only is desired, as it allows for a high distinguishable SCF at the coating-substrate interface (compare section 4.1.1.4), requires low strain to initiate cracks and allows for crack propagation through the coating layer.

2) Beside the coating properties, a key step to enable the sequential coating rupture is the interfacial adhesion of the coating to the substrate. The coating fixation depends on its adhesion on the substrate surface, where the adhesion strength relies on the type of the interaction between the coating and the substrate [131]. If the coating film has a weak interfacial adhesion on the substrate, it may be detached or delaminated before or during stretching [126], which leads to losing the functionality of the system. Therefore, an intermediate layer to enable a strong adhesion at the substrate-coating interface is desired to assure a local transfer of the stress and strain concentrated at cavities to the coating layer (described in 4.2.2).

4.2.1. Coating material selection

Based on their physiochemical properties, polystyrene (PS) (ε_B = 5%) [132], poly(methyl methacrylate) (PMMA) (ε_B = 3-4%) [132] and polycyanoacrylate (polyCA) (ε_B ranging from 0.05% to 4.5% based on polyCA material side chains; compare section 5.4) were identified as potential coating materials. In principle, a thin coating layer of PS or PMMA can be prepared by a spin coating of the polymer solution [133] and the thickness can be controlled by many parameters, e.g. polymer concentration, spinning speed and solvent evaporation rate. In case of PS or PMMA coating, their interaction with the substrate surface will base on a physical

interaction. This interaction may be weak and could result in detachment form the surface particularly when immersed in a solution, which induces peeling of the coating due to the capillary forces supporting creeping of fluid into the substrate-coating interface [134]. Therefore, a coating method is preferred, which can form a thin coating and conceptually allows a strong adherence to the device.

PolyCA may be used for the coating purpose since polyCAs are reported as applicable materials in biomedical field, having a good film forming feature, and breaking characteristics upon a small mechanical deformation [132, 135]. Cyanoacrylates undergo a rapid anionic polymerization upon contact with nucleophilic groups such as hydroxyl groups, which may allow in situ polymerization initiation from the surface of the device. Such an approach may provide covalent bonds between coating/device and assure a strong coating adhesion. For this purpose, a treatment of the device surface should introduce nucleophiles at the surface as explained in 4.2.2. Additionally, the film structure of polyCA layers formed at interfaces may enhance its breakability. PolyCA may form a bulk film composed of globule-like structures due to the numerous initiation sites [135]. Upon stretching, this globules structures may cause a non-uniform stress distribution in the coating layer and globule junctions serve as weak points, which may support coating failure (Figure 23).

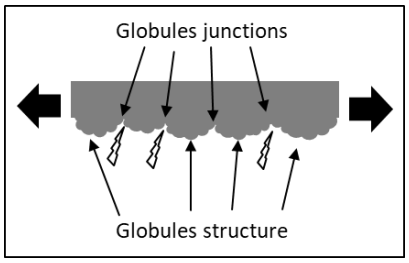

Figure 23.Schematic cross-sectional view of a coating layer with an inhomogeneous surface morphology (globules-like structures), which may facilitate the initiation of the coating rupture at the junction sites upon stretching due to a non-uniform stress distribution.

4.2.2. Substrate pre-treatment to form intermediate layer

Since CA-monomers undergo anionic polymerization in the presence of nucleophilic groups, it is a promising approach to initiate CA coating from the substrate to assure a strong adhesion between coating/substrate by covalent bonds. However, such a concept may require a substrate pretreatment to immobilize functional groups at the surface. It has been reported that polydopamine (PDA) can be applied as a surface modifier on various materials due to the ability of dopamine to self-polymerize on surfaces, including PDMS and PCL, in aqueous environments resulting in thin PDA film [117, 118]. This ability of PDA to adhere on different types of materials has before attracted the interest as immobilized initiator for surface-

initiated polymerization, e.g. radical polymerization of various monomers such as methacrylate, acrylate and styrene [136-138]., Of particular relevance, some studies indicated that catecholamine and amine groups, which are a part of the PDA structure, can initiate/accelerate the free radical polymerization of CA [139-141], which suggested that these functional groups may be available for further chemistry, e.g. surface-initiated anionic polymerization. Therefore, in this study, PDA has been explored as an intermediate layer on the substrate that should introduce nucleophilic groups, e.g. amine and alcohol groups as shown in Figure 24 A. These nucleophilic groups should initiate the in situ anionic polymerization of CA-monomer upon contact with the surface of the substrate as shown in Figure 24 B.

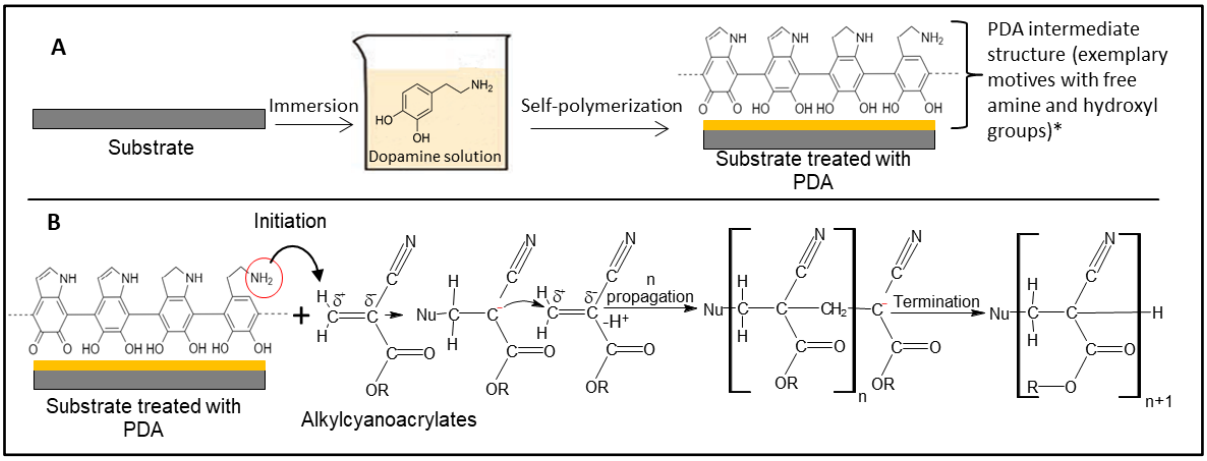

*Figure 24. Concept of using PDA as intermediate layer. A) A PDMS substrate is treated with PDA (yellow) to deposit functional groups at the surface (e.g. amine group, marked with red circles). B) Functional groups may initiate cyanoacrylate polymerization and assure a strong coating-substrate adhesion. * A multitude of PDA structures can be formed and that depicted structures stand exemplarily but not exclusively for motives known to be present in polydopamines.*

The validity of the concept was, at first, explored macroscopically by examining the ability of PDA to initiate CA polymerization as shown in Figure 25. Dopamine was polymerized to PDA particles in TRIS buffer (pH=8.5), which were then freeze-dried. Subsequently, 1.5 mg of PDA particles were mixed with 1 ml of neat ethyl cyanoacrylate (ECA) monomer. After 24 h, the liquid CA monomer had polymerized to a solid material, while the control (without PDA particles) remained a non-polymerized liquid.

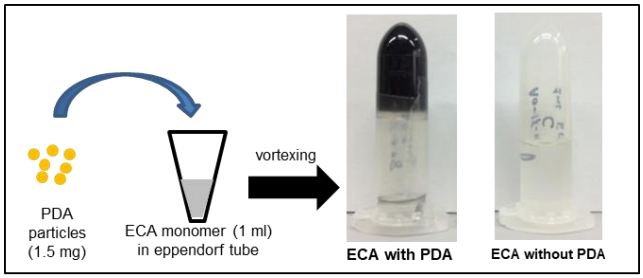

Figure 25. Demonstration experiment to evaluate the ability of PDA to initiate ECA polymerization. PDA particles (black) were mixed with ECA monomer, which is polymerized after 24 hour (black solid) compared to ECA-monomer without PDA (liquid).

Furthermore, the concept was supported by structural analysis at the molecular level. X-ray photoelectron spectroscopy (XPS) was applied to determine if there is a chemical reaction between PDA and ECA. In literature, PDA was proposed to exhibit a mixture of structures [142]. PDA may include hydroxyl group, primary amines (R-NH_2) and/or secondary or tertiary amines (Figure 26). The assumption for XPS data interpretation was that the nucleophilic groups of PDA initiated the polymerization of ECA-monomer, resulting in a change in the percentage of measured functional groups, e.g. reduction in percentage of NH_2 and C-OH of PDA.

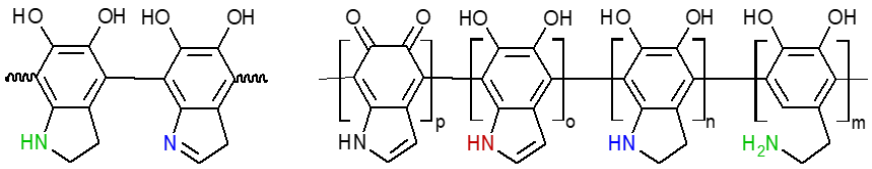

Figure 26. Structures of PDA suggested in literature [142].

As a reference in this study, PDA particles were prepared and examined by XPS. The amine groups were determined as: primary amine (17.3%, n = 1), secondary amine (70.9%, n = 1) and tertiary amine (11.8%, n = 1) as shown in Figure 27 A. On a scarifying layer of PEG, 150 µl of PDA suspension was spread over the PEG layer followed by solvent evaporation, which allowed forming a thin layer of PDA nanoparticles (experiment detail in 7.2.8). Thereafter, 50 µl of ECA monomer was spread over the PDA layer, which formed PDA-PECA film. The PEG layer was dissolved in water to detach the PDA-PECA film for XPS analysis from the PDA side (as the penetration depth of the XPS is ≈ 10 nanometer). After adding ECA-monomer onto the PDA layer, results showed noticeable change in the detected functional groups. For PDA-PECA films (Figure 27 B), the percent of primary amine was reduced to R-NH_2 = 3.7% (n = 1) and the percent of secondary amine (R-NH-R) was increased to = 94.4% (n = 1). This may suggest that primary amine groups contribute to the initiation of ECA polymerization, which leads to conversion of primary to secondary amines. Beside amine groups, it was also expected that ECA polymerization may be initiated by hydroxyl groups of PDA leading to a conversion of C-OH of PDA to C-O-C moieties. However, as the oxygen atom of alcohol has a binding energy in the same range of the oxygen atom of the ether group, the moieties of interest were not distinguishable.

In general, this result are in consistence with literature [141, 143, 144], whereas it has been reported that the polymerization of CA monomers can be initiated by catecholamine groups or aminated surfaces, e.g. by ammonia plasma treatment [145].

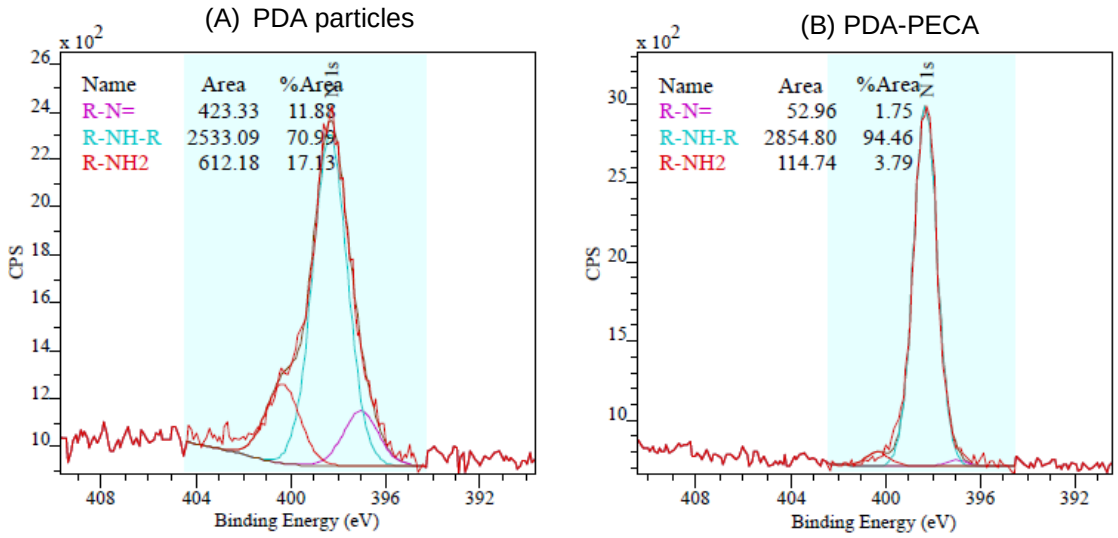

Figure 27. XPS results of A) PDA particles and B) PECA-PDA film. Noticeable change in the percentage of primary and secondary amine of PDA compared to PDA-PECA suggested that primary amine groups contribute to the initiation of ECA polymerization (conversion of the primary amine to secondary amine). For each measurement n = 1. Typical experimental error of XPS is 10%.

In conclusion, the macroscopic demonstration experiment as well as the XPS characterization indicated the ability of PDA to initiate ECA polymerization to form covalent bonds, which should lead to a strong adhesion between coating/substrate. Accordingly, each substrate was first treated with PDA, then loaded with substances, and thereafter coated with polyCA as described in the next section.

4.3 Compound loading and cavity coating

As described previously in the concept scheme (section 3.1, Figure 13 B), the cavities should be filled before preparing a coating layer. A micro-injection technique enabled loading each cavity individually with ≈ 25 nl aqueous dye solutions (methylene blue and fluorescein sodium) selected as model compounds (experiment detail in 7.2.4), which should allow visualizing the dosing initiation under an applied strain. Poly(n-butylcyanoacrylate) (PBCA) was used as a coating material due to its moderate brittleness among other examined polyCA (mechanical properties of different polyCA coating determined experimentally in section 5.4), that should allow cavities sealing, cracking resistance during sample handling and breaking upon intermediate strain.

The coating was prepared by twice spreading a solution of BCA-monomer (1% v/v in hexane) by a micropipette over the loaded cavities (dye liquid mixture of water/PEG_{200} in a ratio of 1:9; experiment detail in 7.2.4 and 7.2.5). Hexane was selected as a solvent because it dissolves the CA-monomer but not the formed polyCA. By applying this approach, a coating layer of PBCA was obtained over the geometrical cavities with a thickness of 2 ± 0.9 µm (n = 6) as determined by SEM (Figure 28). The coating, as expected, has an inhomogeneous surface morphology (globules structures) at substrate-coating interface, which may facilitate the coating failure at the globules junctions' as explained previously (compare section 4.2.1, Figure 23). These globular structures may be attributed to the numerous initiation sites and/or the interfacial dynamics underneath the coating layer during polymerization.

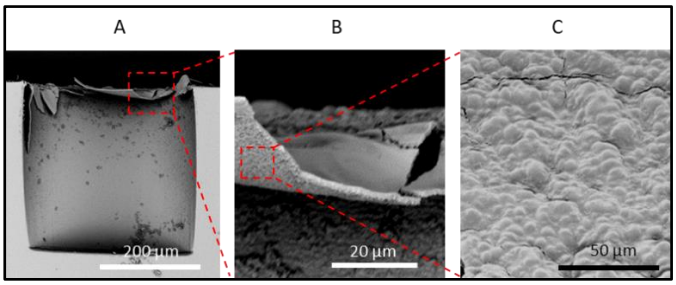

Figure 28. A) SEM image at cross-section after stretching of a cylindrical cavity coated with PBCA on top showing the broken coating. B) Magnified part of the coating layer. C) Surface morphology (globules structures) of the coating layer at the coating-substrate interface. Coating thickness = 2 ± 0.9 µm (n = 6).

4.4 Experimental demonstration and characterization of structure-function relationships

For functional evaluation of a sequential release of compounds, substrates with two types of cavities (design 2, shown in Figure 16) were treated with PDA, loaded with dyes (rhombus cavities loaded with methylene blue; circular cavities loaded with fluorescein sodium) and coated with PBCA as described in the previous section. The samples were inserted in a customized tensile device, which was placed in a water bath (25 °C) under a microscope with high speed camera and subjected to continuously increasing stretching (Figure 29 A) (experiment detail in 7.2.6).

In a first experiment, the samples explored in the tensile device had the circle-shaped cavities at the constrained side and the rhombus-like cavities at the movable side. Under an applied tensile load, the release was initiated first from rhombus reservoirs and then, upon further stretching, from circular cavities (Figure 29 B). In a second experiment, the orientation was inverted by placing the circular cavities close to the movable side and the rhombus cavities at the constrained side (Figure 29 C). In accordance with the concept, the release was again

initiated first at rhombus reservoirs and then at circular reservoirs, which confirmed the hypothesized principle of the study.

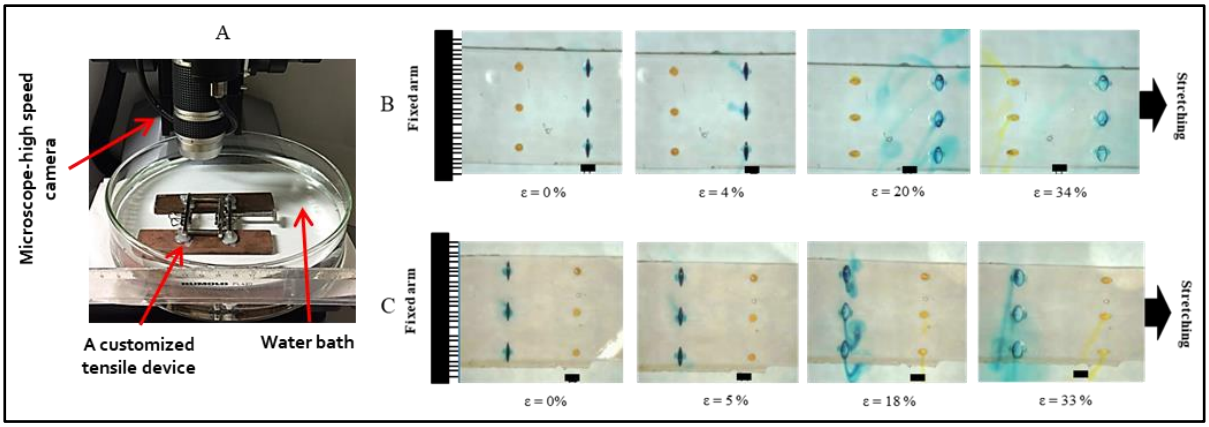

Figure 29. A proof of the principle of the step-initiation of dosing from micro-geometrical reservoirs due to the differential locally concentrated stress and strain at different geometrical structure. The geometrical reservoirs loaded with dyes (rhombuses cavities loaded with methylene blue; circular cavities loaded with fluorescein sodium), then sealed with PBCA and stretched in a water bath under a microscope with high speed camera. A) Experimental setup to microscopically monitor the device stretching in a water bath. B) Rhombus reservoirs at the movable arm. C) Circular reservoirs at the movable arm. In both cases, under a continues applied tensile strain, the release initiated first at rhombuses reservoirs then at circles. Scale bars = 500 µm.

In order to quantify the released from geometrical reservoirs and to correlate it to the corresponding strain, an in-situ quantification based on grayscale intensity has been applied [146] (experiment detail in 7.2.7). For a quantitative analysis, three cases of substrates are considered: (i) substrates containing only circle shaped reservoirs, (ii) substrates contains only rhombus shaped reservoirs and (iii) substrates containing the two types of shapes (Figure 17, design 2).

When the samples were stretched continuously, the release initiated at $\varepsilon \approx 1 \pm 0.4\%$ (n = 3) in case of substrates with only rhombus-shaped cavities, and increased by increasing the applied strain (Figure 30 A). In case of only circle-shaped cavities, the release was initiated at $\varepsilon \approx 3 \pm 1\%$ (n = 3) (Figure 30 B). When combining the two geometrical cavities (Figure 30 C), the release from the rhombus reservoirs was determined to initiate at $\varepsilon \approx 1 \pm 0.3\%$ (n = 3), then followed by initiation from circles reservoirs at $\varepsilon \approx 12 \pm 1\%$ (n = 3). The shift of release-initiating strain from $\varepsilon \approx 3\%$ to $\varepsilon \approx 12\%$ for circles in substrates containing either circles only or circles plus rhombus-shaped cavities can be attributed to StrCF. As demonstrated before (Figure 22 B, design 2), the StrCF of circles is reduced in this combination (as the strain distributed among cavities), which enables a lower concentrated strain and thus a clear separation of the coating breaking at rhombus and circular cavities.

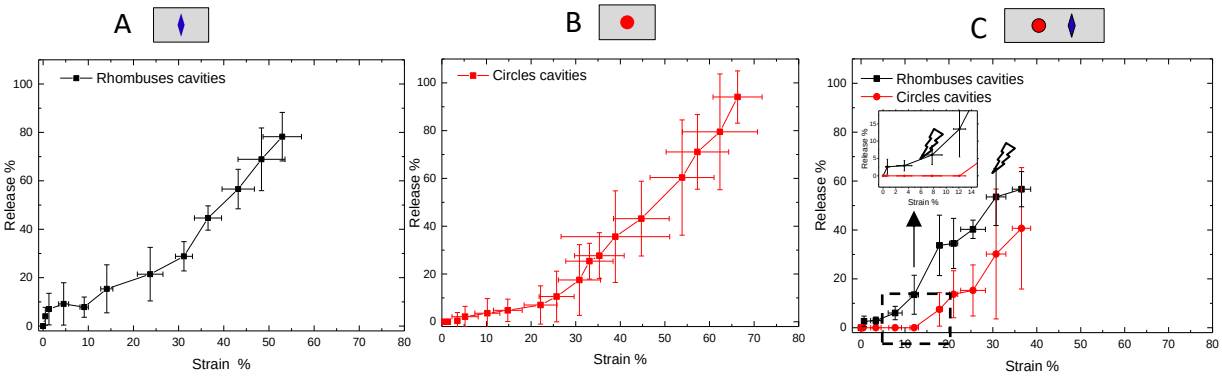

Figure 30. Release profiles from geometrical reservoirs in substrates under a tensile load. A) Release from substrates containing only rhombus cavities. B) Release from substrates containing only circular cavities. C) Structure-Function relationship of the system; release from substrates containing dual shape-reservoirs (rhombuses and circles), which leads to a step-initiation of dosing under a continuous stretching due to the stress and strain concentration principle. Inset shows a magnification with dosing initiation from rhombus cavities occurring first at ε ≈ 1% ± 0.3%, followed thereafter upon further stretching by the second initiation from circular cavities at ε ≈ 12% ± 1%. Data represented as mean ± SD (n = 3). Average strain rate ≈ 0.5%/s ± 0,2%/s (n = 3). Error of the customized tensile device is determined to be 11%

It is apparent from Figure 30 that the release of the dyes, once initiated, does not occur all at a time (bolus) when the crack is formed. Instead, in this continues stretching experiment with a deformation rate of ≈ 0.5 ± 0,2%/s (n = 3), the dye release is completed over a certain time that falls together with increasing ε. In principle, there are two possible contributions to release after the first crack was formed: (i) diffusion of dye from a PEG filled component (cavity) to the surrounding medium through a small slit (crack), while the rest of CA coating continue to act as diffusion barrier; (ii) further opening of the crack to increase surface area between medium and dye loaded cavity accountable for diffusion. Conceptually, with cracks initiation, the release by (i) is understood as the effect-determining step, while (ii) contributes to kinetics together with other parameters like viscosities of payload/medium, removal of boundary layers by stirring, or dissolution in case of solid payloads. Therefore, the initiation of release was here understood as proof-of-concept for function-function coupling in accordance with the conceptual Figure 12.

The concept of sequentially coupling the mechanical input (stretching) with a defined order of cavities opening for a controlled multi-dose initiation (output) from a single substrate has been successfully demonstrated. The realization of the concept was linked to structure-function relationships of the system on the device level. The cavities in the substrate served as reservoirs and as cues that can guide and rise the stress and the strain to the sites of interest when the substrate is stretched. At a defined magnitude of the applied tensile load, the

magnitude of the SCF and StrCF can be simultaneously modulated by the cavity structure combined in the substrate, e.g. vertical rhombuses and circular cavities as in case of Figure 30 C. When the applied strain in the substrate is ≈ 1%, the strain at the vertical rhombus cavities has been ≈ 6% and at circular cavities ≈ 1.5% due to StrCF of each shape (compare Figure 22 design 2).

Applying PDA as intermediate layer enabled a strong adhesion at the substrate-to-coating interface that allowed local transferring of this distinguishable values of SC and StrC from the substrate to the coating layer. However, due to the type of applied load (continuous stretching without intermediate stopping) with the manually realized strain rate (≈ 0.5 ± 0,2%/s, n = 3), the release was not been fully separated from each type of cavities in Figure 30 C. Based on this principle, complete separation of release might be realized by lower stretching rates with a rate-controllable electronic deformation system or by intermediate stopping of deformation.

During the system operation, the payload in the cavities is liquid, which allowed following the deformation of the substrate upon stretching as observed experimentally under the microscope (see Figure 29). Accordingly, it is assumed that filling has no major influence on the mechanics of the substrate. Along with the uniaxial load applied on the x-axis, the substrates also experience a lateral reduction in width (lateral strain along y-axis, denoted as ε_y) according to the materials Poisson's ratio. The lateral strain was characterized microscopically during stretching experiments. When the substrates were axially strained nearly at the maximum strain at ε_x ≈ 35 ± 2 % (n =3), the lateral compression was quantified to be ε_y = -11.8 ± 2.5 % (n = 3). As the coating is a very thin polymer film (compared to the substrate), it is assumed that the coating fully follows the lateral deformation of the substrate. In this context, it is anticipated that during the uniaxial stretching, first, cracks are initiated at the substrate-coating interface at cavities in accordance with the characteristic SC and StrC and propagate perpendicular to the direction of stretching. With further stretching, a minor transvers buckling (y-direction) will be occur as the substrate/coating experiences lateral compression (due to Poisson ratio). By increasing the strain, the cracks density (number of cracks per unit area) will increase until reaching the saturation phase (no more cracks are formed), while subsequently the distance between cracks increases via crack opening upon further applied strain [126].

Along with the design of the cavities in the substrate, it is also anticipated that altering mechanical properties of coating materials can modulate the output of the system. In Figure 30 C, the first and the second dosing initiated at strain of ≈ 1% and ≈ 12%, respectively, as the used PBCA coating has a moderate value of strain at break (determined experimentally in Chapter 5, section 5.4, Figure 46 C with respect to the given thickness) compared to other polyCA materials. In Figure 30 C, employing e.g. PMECA or PEECA (compare Figure 46 C) should delay the sequential initiation of dosing as the coating has a high stretchability.

In this study, the sequential dosing function was demonstrated (by the substrate of design 2) as a proof-of-principle, however, it is assumed that this function is not limited to the proposed design. Different composition of geometrical cues/reservoirs in a substrate may enable/disable this function. For instance, it is anticipated that cavities of vertical rectangles and circles in a single substrate should lead also to a sequential dosing function as, individually, they have distinguishable SCF values (compare Figure 17 A). On the other hand, compositions of, e.g. horizontal rectangles with circles, horizontal rhombuses with circles or vertical rectangles with vertical rhombuses in a single substrate will properly not enable the sequential dosing function because the cavities, individually, have very similar values of SCF (compare Figure 17 A). Beside the shape of the cavities, another option is the depth of the cavities in the substrate as it can modulate the SCF (shown in Figure 19 B). Combining two similar type of cavities of different depth in a single substrate, e.g. two rhombuses cavities with depth of $D_{cavity} / D_{substrate}$= 0.1 and $D_{cavity} / D_{substrate}$= 0.9, produces different SCF at each rhombus cavity (see Figure 19 B), which is anticipated to enable the sequential dosing function upon substrate stretching.

The situation considered in this work is fundamentally different from literature, which focused on notches-structured substrate/and or coating films to control the cracks initiation, propagation, periodicity, regimes and termination for micro- and nano-pattering [25, 26, 147, 148]. The finding in the current work adds to the knowledge that despite the coating is not structured and the substrate is not notched, the stress distribution in the coating layer can be controlled and localized by the underneath cutout-geometries, which determine the magnitude of the stress locally transferred to the coating layer by their shapes. Furthermore, here it is anticipated that the coating failure is initiated from the interface of coating-cavities and propagated transversely to the boundaries of the substrates. Moreover, it is assumed that

the magnitude of the locally transferred stress to the coating layer can be modulated by the mechanical properties of the coating materials and the substrate.

In this study, the sequential dosing concept goes beyond the existing principles of stretching-induced dosing, which typically allows only single-step release by opening pores via cracks in a diffusion barrier [106], or by a reduction of cavity volume due to lateral contraction upon stretching [107]. In contrast, the principle presented here allows a multi-step release of either the same or different types of substances from one substrate. The order of release initiation can be defined by the appropriate selection of the cavity shapes, which act as geometrical cues for stress and strain concentration.

4.5 Summary

This chapter described the design, fabrication, characterization and evaluation of tensile-on-demand sequential dosing from a single polymeric substrate. It was hypothesized that a single polymeric substrate containing various shaped micro-reservoirs sealed with a polymeric film should respond to a mechanical stretching by sequentially initiating the dosing from the reservoirs in a defined order based on the principle of stress and strain concentration.

In order to realize the function-function coupling for the sequential dosing effect, the different functions and their principle of coupling should be briefly stated for 1) the design of the substrate with distinct shaped reservoirs and their orientation was needed as they concentrated the stress and the strain differently at distinct sites of reservoirs, 2) the transition of these concentrated stress and strain locally form the substrate to the coating layer need to be ensured by a strong adhesion at the substrate-coating interface and 3) a hydrophobic coating polymer should seal the reservoirs temporarily and is breakable at a small strain.

The concept of this study was supported computationally via FEA, which has been successful in screening design parameters and guiding the experimental studies. The evaluation of the structure-function relationships by FEA revealed that combining two types of geometrical cavities, e.g. vertical rhombuses and circles (as for design 2 shown in Figure 16 D), in a substrate does not impair the SCF, rather preserves the different SCF values for each type of geometrical cavity. Moreover, deeper cavities in the substrate increased the SCF. The characteristics of the stress transition from micro-structured substrates to a thin breakable

film (substrate design 2) has been explored and analyzed by FEA when the substrate is subjected to a tensile load. The raised stress at geometrical reservoirs in the substrate transferred locally to the coating layer. The magnitude of the stress at the coating-substrate interface is found to be higher over non-circular cavities of a higher SCF, i.e. the stress in the coating at the interface over the rhombus cavities is higher than over the circular cavities. Additionally, the evaluation indicated that reducing the coating thickness from 15 µm to 1 µm raised the SCF at the coating-substrate interface. These design parameters were considered for the experimental evaluation.

Coating fixation was assured by employing the concept of PDA as intermediate layer for surface-initiated polymerization of CA coating on the surface of the substrate. The concept was confirmed by the XPS analyses, which indicated that the primary amine groups of PDA contributed to the initiation of CA polymerization. The cavities were loaded with dyes and coated in situ by adding a solution of BCA-monomer over the dye solution-loaded cavities leading to an in situ polymerization and forming a coating layer of PBCA with a thickness of 2 ± 0.9 µm (n = 6).

The substrate of design 2 (shown in Figure 16 D) was justified as a suitable design due the distinguishable values of SCF and StrCF of the micro-scaled cavities. Substrates of design 2 were fabricated from PDMS as prototype devices, treated with PDA, the cavities were loaded with dyes and sealed by PBCA. By subjecting the substrates to a continuous uniaxial tensile load in a water bath under a microscope, the first dosing was initiated from rhombuses cavities at $\varepsilon \approx 1\% \pm 0.3\%$ (n = 3), then, by further stretching, followed by initiation of dosing from circular reservoirs at $\varepsilon \approx 12\% \pm 1\%$ (n = 3). From these results, the hypothesis of concept 1 has been addressed and experimentally proven.

The respective shapes of cavities, their payload as well as the mechanical properties of substrate and coating open up a platform of parameters to broadly tailor the time-point and order of release. Therefore, on-demand sequential dosing systems or tensile sensor devices may be created for technical and biomedical applications.

Chapter 5 Self-sufficient thermo-responsive dosing device

In this chapter, the concept of coupling thermosensitivity (input) with an on-demand release (final effect) will be explored by employing a coated SMP skeleton in a re-Hex NPR structure. According to the strategy in section 3.2, by design, the system should have: 1) a device design of a high magnitude of NPR (high biaxial expansion ability to facilitate breaking of the sealing layer), 2) processability to be manipulated towards a compressed state, which should temporarily store force and (upon stimulation) translates this force into strain exceeding the value of force and strain at break of the coating layer (induce coating rupture), 3) a connecting layer between the substrate and the coating to assure the transfer of mechanical deformation between those materials, and 4) a coating that can break upon shape switching of the device. These structure-function relationships will be evaluated in the following sections.

5.1 Evaluating structure-function relationships of the re-entrant hexagonal (re-Hex) structure as biaxially expandable devices

Estimating of NPR and shape-recovery force from a re-Hex structures

The polymer skeleton with re-Hex geometry (Figure 31 A) should be produced from SMP in the permanent shape, which characterized by the permanent angle (α_{per}). The structure will then be bi-axially compressed (programmed) to a temporary shape with a temporary angle (α_{tem}). As a consequence of the degree of angle changing ($\Delta\theta$) (Equation 7), the value of NPR will be altered. In addition to the NPR value, the generated force during shape-recovery (biaxial expansion) is considered a key point to enable the functionality of the system by breaking the coating layer.

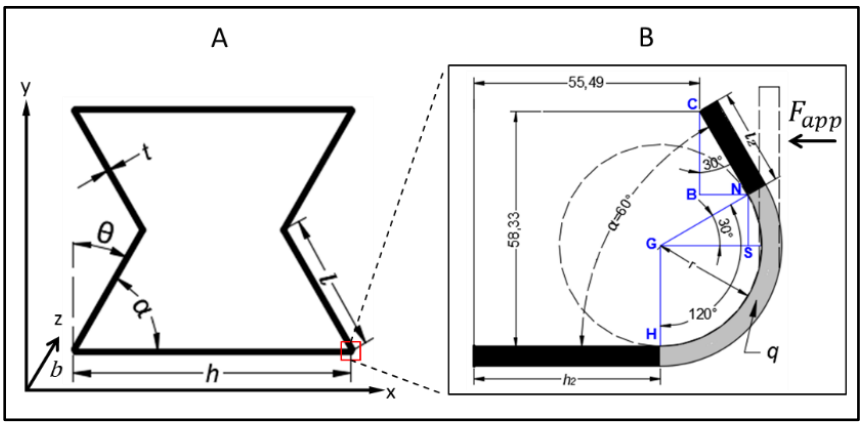

Figure 31. A) Cell geometry and coordinate system of a re-entrant hexagonal cell. B) Schematically magnified view of the hinge (bold black and grey) after exemplary cell deformation to α_{tem} = 60° by angle hinging due to a local wall bending under an applied load. The dashed circle represents the bending tool, which has a radius r. The gray curve represents the arc length of the hinge (q).

According to the hinge model (described previously in 1.3, Equation 11), in case of SMP device, the deformation during the device programming should occur only at angles, while other portions of the cell walls remain non-deformed. Accordingly, it was concluded that the effective polymer volume of a re-Hex substrate that is contributing to the SME is directionally linked to b, t, $\Delta\theta$ and q as shown in Figure 31 B. When higher F_{app} is required for programming in case of thicker skeleton walls and higher depth, a higher shape-recovery force (F_{rec}) is expected. It should be noted that the expected value of F_{rec} according to Equation 11 may not necessarily represents the eventually observed shape-recovery force. This is due to the fact that the force of shape-recovery also depends on the force-storage-capacity of the deformed polymer segments. In this study, the matrix of the device will be built of a PCL-based polymer network that is characteristic by its high shape fixity and high rate of shape-recovery and thus low dissipation of introduced mechanical energy. Based on that, it is assumed that F_{rec} is approximately equal to F_{app} (Equation 18).

$$F_{rec} \approx F_{app} \approx \frac{E\ b\ t^3\ l\ sin\ \Delta\theta}{6\ l^2 q} \qquad \text{Equation 18}$$

Figure 31 B illustrates the deformation at a hinge of the re-Hex structure upon wall bending (exemplary to α_{tem}= 60°) via a bending tool of known radius (r) (Figure 30 B, dashed circle). As parts of the length l (shown in Figure 31 A) contributes to the hinging (Figure 31), the remaining length l_2 is used to replace l in Equation 18, thus F_{rec} can be expressed as:

$$F_{rec\ (per\ hinge)} \approx F_{app} \approx \frac{E\ b\ t^3\ l_2\ sin\ \Delta\theta}{6\ {l_2}^2 q} \qquad \text{Equation 19}$$

The arc length of the hinge q is considered a key value as it corresponds to the part of the polymer networks that contributes to the deformation. The value of q can be calculated by considering the hinge as a sheet, which has a known length before bending (Equation 20).

$$hinge\ \ length = h + l \qquad \text{Equation 20}$$

After bending, as h and l will be altered to h_2 and l_2 (shown in Figure 31 B), accordingly q can be calculated by Equation 21 and Equation 22:

$$hinge\ length = h_2 + q + l_2 \qquad \text{Equation 21}$$

$$q = hinge\ length - h_2 - l_2 \quad \text{Equation 22}$$

Quantifying the value of q requires measuring the length of h_2 and l_2, which can be determined by calculating the bending allowance of the hinge as described in reference [149]. Accordingly, by the illustrated information in Figure 31 B, l_2 can be calculated as:

$$l_2 = \frac{\overline{CB}}{\cos \angle BCN} = \frac{\overline{CB}}{\cos 30} \quad \text{Equation 23}$$

where $\overline{CB}$ can be calculated as:

$$\overline{CB} = 58.33 - \overline{NS} - r \quad \text{Equation 24}$$

and $\overline{NS}$ can be calculated as:

$$\overline{NS} = \overline{NG} \cdot \sin \angle NGS = r \cdot \sin 30 \quad \text{Equation 25}$$

By the same approach, the length of h_2 can be calculated by Equation 26:

$$h_2 = 55.49 + \overline{NB} - \overline{SG} \quad \text{Equation 26}$$

where:

$$\overline{NB} = l_2 \cdot \sin 30 \quad \text{Equation 27}$$

$$\overline{SG} = \overline{NG} \cdot \cos \angle SGN = r \cdot \cos 30 \quad \text{Equation 28}$$

By substituting the value of l_2 and h_2 from Equation 23 and Equation 26 in Equation 22, the value of q can be determined. Equation 22 is applied to calculate the q value as needed to estimate the $F_{rec\ (per\ hinge)}$ according to Equation 19.

Equation 19 was applied as a model to theoretically evaluate the effect of different design parameters on $F_{rec\ (per\ hinge)}$ and provide guidelines for possible experimental designs of re-Hex structures made of SMP (Table 2). As the re-Hex design is intended to be fabricated from PCL-diIEMA network due to its elasticity and high recovery rate [122], the PCL networks value of E = 3.5 MPa (at 70 °C during shape-recovery) [75] is applied in Equation 19 to estimate $F_{rec\ (per\ hinge)}$. Furthermore, for quantifying the q value, r = 0.2 mm is applied as it represents the virtual value during the experimental programming by PDMS molds (as described in section 5.2.3). It should be considered that F_{app} will be negative during compression as $\Delta\theta$ is negative, while $F_{rec\ (per\ hinge)}$ will be positive when the cells expand.

As shown by the values calculated in Table 2, increasing of h/l from 1 to 2 (design No. 1 and 3) doubles the NPR from -0.25 to -0.64, respectively, when other parameters are constant. It should be noted that experimentally, when h/l > 2 (long h and/or short l), the magnitude of NPR may be decreased due to hindering the bending of angles during compression. Therefore, the ratio of $h/l = 2$ has been selected further in this study.

Table 2 further shows the effect of the parameters t and b, where doubling the wall thickness from 0.15 to 0.3 mm (design No. 4 and 6) resulted in an increase of the estimated $F_{rec\,(per\,hinge)}$ from 0.30 mN to ≈ 2.9 mN. Despite Equation 19 indicates that $F_{rec\,(per\,hinge)}$ is strongly related to the skeleton wall thickness t (power of 3), increasing t to the macro-scale will at the same time reduce the magnitude of NPR [150]. That may be attributed to a situation where thicker walls may hinder wall bending and reduce the relative change of angles during compression, thus negatively affecting the magnitude of NPR. Therefore, in the design applied in this study, t was optimized to 0.3 mm, which allows enhancing $F_{rec\,(per\,hinge)}$ and dose not impair the auxetic behavior. Furthermore, increasing the depth of the samples from 1 to 2.5 mm (Table 2, design No. 7 and 9) elevated the theoretically possible $F_{rec\,(per\,hinge)}$ up to 14.4 mN.

Table 2 also summarizes the effect of $\Delta\theta$, i.e. higher deformation during programming, when the other parameters remain constant. Decreasing $\Delta\theta$ from -20° to -40° (design No. 10 and 12, respectively) enhanced the magnitude of NPR approximately 2 folds and simultaneously increased the estimated $F_{rec\,(per\,hinge)}$ from ≈ 14.5 to ≈ 27 mN. Importantly, a design with α_{per} = 90° has a square permanent shape and produces the highest magnitude of NPR. When α_{per} > 90°, the shape will have a conventional hexagonal design and will exhibit a positive Poisson's ratio (ν), which is not desired.

Table 2. Evaluation of structure-function relationships of re-Hex cell by hinge deformation model. Effect of parameters variation of the re-Hex cell on NPR and estimated shape-recovery force of a given fixed programmed (compressed) shape providing guidelines for experimental design selection. Gray shaded values in each part of the table represent the variable parameters.

Design NO.	$\Delta\theta$ (a)	*h/l*	*t (mm)*	*b (mm)*	α_{per}	α_{tem}	NPR (b)	$F_{rec\ (per\ hinge)}$ (c) (mN)
1		1					- 0.25	0.04
2	- 20°	1.5	0.1	0.5	70°	50°	- 0.44	0.07
3		2					- 0.64	0.10
4			0.15					0.30
5	-20°	2	0.2	0.5	70°	50°	- 0.64	0.85
6			0.3					2.88
7				1				5.77
8	-20°	2	0.3	1.5	70°	50°	- 0.64	8.66
9				2.5				14.43
10	-20°				70°		- 0.64	14.43
11	- 30°	2	0.3	2.5	80°	50°	- 1.00	21.10
12	-40°				90°		- 1.48	27.13

(a) $\Delta\theta$ is negative in programming (compression) and positive in shape-recovery (cell expansion).
(b) Calculated according to Equation 7.
(c) Calculated according to Equation 19.

To enable the functionality of the system, the skeleton should be designed to provide high values of NPR and F_{rec} upon actuation. The shape-recovery force generated by a SMP as a characteristic of a polymer need to be considered [151]. The shape-recovery force can be increased by incorporation of inorganic nanocomposites, e.g. carbon nano-tubes and carbon nano-fibers [151, 152]. However, such fillers may impair the SME and reduce the fixity of the temporary shape and the strain-ratio of shape-recovery [153]. The selected PCL-based network material has a suitable elasticity enabling substantial deformation (bending), the extent of which is controllable by the volume of the material in the hinges of the individual skeleton cells. By applying the hinge model, the effect of the parameters of $\Delta\theta$, t, b and h/l on NPR and F_{rec} , respectively, were quantitatively evaluated. It was detected that decreasing $\Delta\theta$ and increasing t and b during programming should lead to enhanced values of NPR and F_{rec}. This effect was facilitated in the design number 12 from Table 2, which was selected as standard re-Hex-SMP device in this study due its theoretical large extent of NPR = -1.48 and $F_{rec\ (per\ hinge)}$ = 27.13 mN. As a reference, also design 3 was used in some studies, which also included the fabrication of devices with multiple cells and the exploration of techniques for their programming.

5.2 Shape-switchable re-entrant hexagon (re-Hex)-SMP skeletons

5.2.1. Synthesis of SMP substrate shaped as re-Hex skeleton

According to the strategy (section 3.2), the device should be used in a compressed state that stores stress and subsequently releases this stress via biaxial expansion upon stimulation. A linear oCL (8 kDa) functionalized with 2-Isocyanatoethyl methacrylate (IEMA) end-group (chemical structure shown in Figure 6 D), denoted as oCL-diIEMA, was used to produce the desired network structure by photo-induced radical polymerization of methacrylate moieties in melt.

Re-hex structures with cell geometries according to designs 3 and 12 (from Table 2) were first fabricated on silicon wafers by the photolithography technique. Thereafter, the structures were replicated in PDMS, which were used as molds. The SMP structures were synthesized by filling the precursor (oCL-diIEMA) in the PDMS molds followed by UV-light irradiation (λ = 250 - 400 nm) in the molten state (experimental details in 7.3.1. and 7.3.2). Since the precursors should undergo a radical polymerization during UV-light irradiation, the presence of oxygen may inhibit the polymerization due to the high reactivity of molecular oxygen toward radical species, which may terminate the course of the cross-linking. Therefore, the synthesis of the re-Hex networks in PDMS molds was performed in a nitrogen atmosphere, which was an efficient method to overcome the inhibition effect of oxygen [154]. By this approach, samples of designs number 3 and 12 were obtained as re-Hex-SMP skeletons with different orientations.

Figure 32 A shows schematically a re-Hex cell geometry in the permanent shape of design number 3 (see Table 2) and the corresponding experimentally obtained re-Hex-SMP skeletons with multiple cells. In skeletons in Figure 32 A, each cell had dimensions of h = 3.1 ± 0.1 mm, l = 1.5 ± 0.1 mm, b = 0.45 ± 0.01 mm, t = 0.1 ± 0.01 mm and α_{per} = 69 ± 1° (n = 6). Figure 32 B shows schematically a re-Hex cell geometry in the permanent shape of design number 12 (see Table 2) and the corresponding experimentally obtained re-Hex-SMP skeletons with multiple cells. Here, each cell had dimensions of h = 3 ± 0.1 mm, l = 1.5 ± 0.1 mm, b = 2.55 ± 0.03 mm, t = 0.3 ± 0.02 mm and α_{per} = 90 ± 1° (n = 6). All obtained multi-cell skeletons showed smooth surfaces without macropores in their struts and exhibited homogeneity in their dimensions.

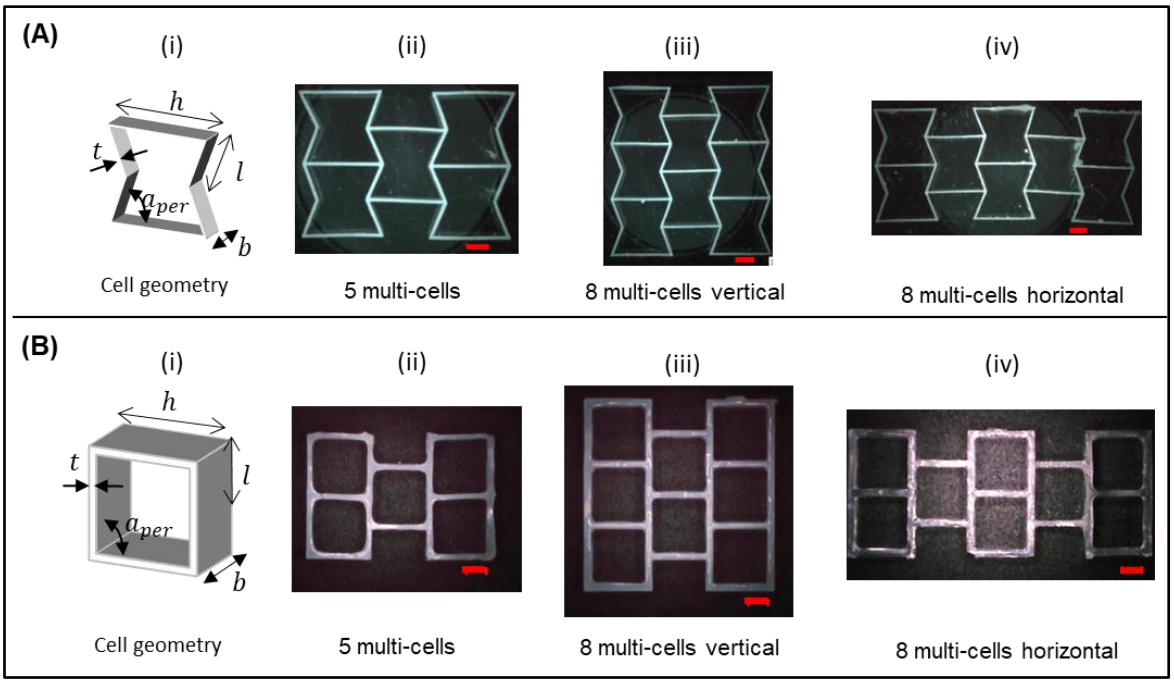

Figure 32. A i) Schematic illustration of a re-Hex cell geometry in the permanent shape of design No. 3 (from Table 2). A ii-iv) Re-Hex-SMP skeletons with cell geometry of design No. 3 obtained as 5 multi-cells, 8 multi-cells vertical and 8 multi-cells horizontal. In all skeletons, each cell has dimensions of h = 3.1 ± 0.1 mm, l = 1.5 ± 0.1 mm, b = 0.45 ± 0.01 mm, t = 0.1 ± 0.01 mm and α_{per} = 69 ± 1° (n = 6). B i) Schematic illustration of a re-hex cell geometry in the permanent shape of design No. 12 (from Table 2). B ii-iv) Re-Hex-SMP skeletons with cell geometry of design No. 12 obtained as 5 multi-cells, 8 multi-cells vertical and 8 multi-cells horizontal. In all skeletons, each cell has dimensions of h = 3 ± 0.1 mm, l = 1.5 ± 0.1 mm, b = 2.55 ± 0.03 mm, t = 0.3 ± 0.02 mm and α_{per} = 90 ± 1° (n = 6). Scale bar is 1 mm.

Characterization of network properties

FTIR analysis was performed to detect the conversion of the functionalized precursor to cross-linked networks. FTIR spectroscopy of precursors (Figure 33 A) showed a peak at 815 cm^{-1} corresponding to the out-of-plane bending vibration of methacrylate endgroups (=CH_2). After crosslinking, the peak disappeared, which indicated the conversion of methacrylate end-groups to form a crosslinked network structure. Furthermore, the thermal properties of the obtained re-Hex-SMP skeleton were characterized by DSC to determine the T_m (Figure 33 B). The materials showed a T_m ≈ 48 °C (n = 1, instrumental error is ± 1 °C), which is above the physiological temperature, as desired. In swelling studies with dichloromethane at room temperature (≈ 25° C) (experiment detail in 7.3.3), the network of skeletons exhibited a degree of swelling Q ≈ 114 ± 4% (n = 3) and a high gel content G ≈ 98.5 ± 0.3% (n = 3), which indicated a successful linkage of the methacrylate endgroups moieties into covalent netpoints. Despite here the samples were crosslinked in a structured mold with a high depth, the network properties agreed with a previous work [79], in which oCL-IEMA applied as precursors in a rectangle film for SMP crosslinking in melt.

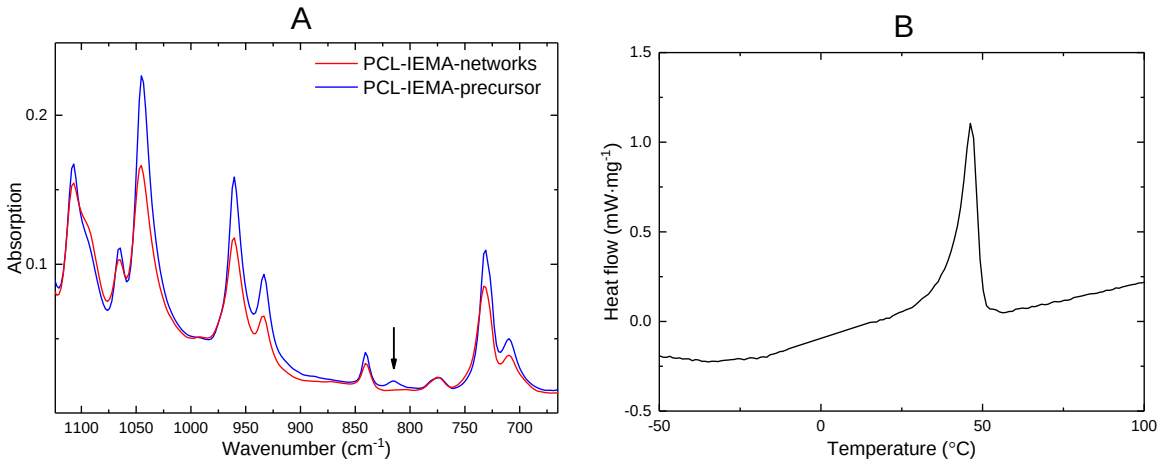

Figure 33. A) A) FTIR spectroscopy of the precursor compared to the corresponding formed network structure. The Peak at 815 cm^{-1} (arrow) assigned to the out-of-plane bending vibration of =CH2 of methacrylate endgroups. B) DSC thermogram of obtained re-Hex-SMP indicating T_m ≈ 48 °C (n = 1, typical experimental error is ± 1 °C).

5.2.2. Programming by lateral compression

In order to enable on demand shape switching, mechanical stress should be introduced and stored inside the re-Hex-SMP device by the SME, which should enable a thermally induced actuation. As the anticipated active dosing effect of the device is depended on the biaxial expansion of the reservoir, it is necessary to obtain a defined temporary compressed shape (biaxially reduced dimensions) by an adequate programming process.

SMP scaffolds such as porous foams are typically programmed by compression. Due to the specific design of re-Hex-materials, as studied for design 3, a uniaxial compression was assumed to result in a biaxial size reduction. However, when applying such a compression on re-Hex-SMP skeletons with multiple cells, an undefined and inhomogeneous deformation was observed in different cells of the skeletons. Specifically, samples composed of 5 and 8 cells showed bulging and structural distortion upon lateral compression (Figure 34).

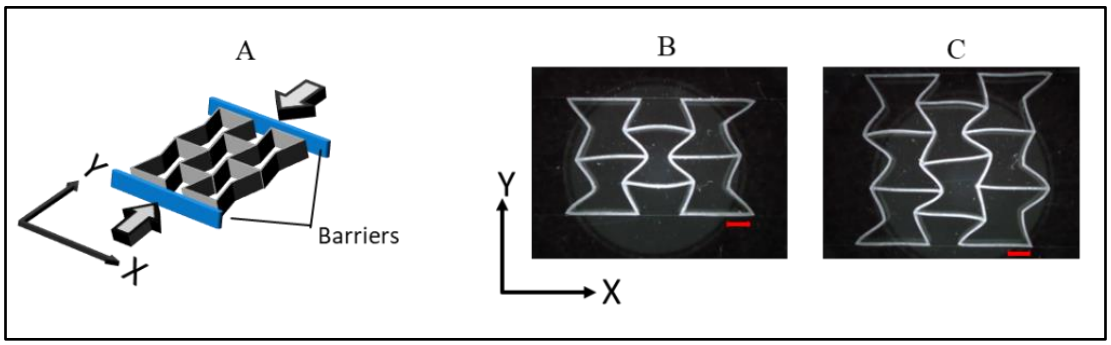

Figure 34. A) Schematic illustration uniaxial compression approach for programming of re-Hex-SMP skeletons. Arrows indicate the compression load. (B, C) Images of distortion of re-Hex-SMP skeletons (with design No. 3, Table 2) of 5 (B) and 8 (C) cells under the applied lateral compression. Scale bar is 1 mm.

This failure (uncontrolled deformation) may be attributed to inhomogeneity of the stress distribution through the substrate under an applied compression load. As the re-Hex substrate consists of jointed struts, the compression load produces a stress on inclined and horizontal walls of each cell. Figure 35 provides a detailed schematic view on re-Hex cells under compression. The compression force translates in a rotational motion of the inclined wall (Figure 35 C), which subsequently produces a shearing motion on the horizontal walls (Figure 35 D) [154, 155]. The rotational deformation apparently produced wave-like motion along the x-axis and simultaneously causes a shearing movement along y-axis (Figure 35 E). A combination of these two types of motions have likely caused the inhomogeneity of stress distribution and hence structure distortion during programming by lateral compression. This is in line with reports on undefined deformation or crushing of re-Hex substrate under load [154, 155]. Therefore, an alternative programming technique was required that could overcome this challenge.

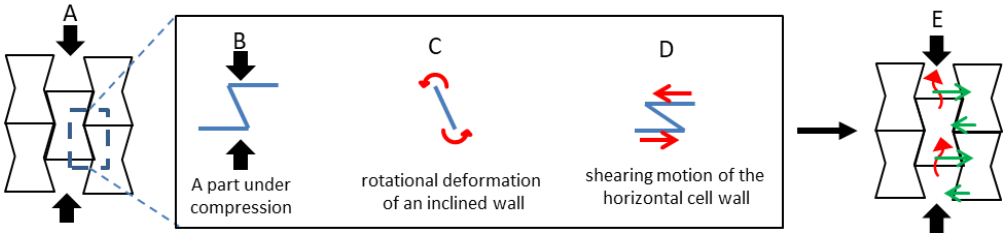

Figure 35. Schematic analysis of possible reason for structure collapse during programming by lateral compression. A) A re-Hex-SMP skeleton during programming. B) A part of a cell under compression. C) Rotational deformation of an inclined wall. D) Shearing motion of the horizontal cell wall. E) Combination of 2 types of motion through the substrate.

5.2.3. Programming by aid of polydimethylsiloxane (PDMS) molds

In order to allow a controlled and defined biaxial size reduction (programming) of re-Hex-SMP skeleton, a technique, which stabilizes the cells and prevents walls buckling was required. For this purpose, a deformation method was established by using a PDMS mold. This technique applies restrictions on walls along their long axis while simultaneously allowing to change the angle α.

In this method, a PDMS template was imprinted with the intended programmed structure, e.g. re-Hex programmed to α_{tem}= 50° (experiment detail in 7.3.4). The deformable re-Hex-SMP substrate of the permanent shape was inserted in the imprinted PDMS template at room temperature (≈ 25 °C). Thereafter, the cold-deformed device was heated (≈ 80 °C) allowing melting of switching domains for elastic deformation followed by cooling (≈ 25 °C) to fix the

temporary shape. Eventually, the programmed structure could be collected from the PDMS mold as shown in Figure 35. The obtained temporary shapes of re-Hex-SMP substrates were characterized by the desired biaxial reduced dimensions with angles altered from α_{per} = 70° to α_{tem}= 50° ± 2 (n = 3) (Figure 35 A). This approach showed an applicability to various designs of re-Hex scaffolds, including designs with orthogonal walls (α_{per}= 90°), which were also programmed to a defined compressed temporary shape (Figure 36 B).

Characterization of SME properties

As the re-Hex-SMP skeletons are programmed by a controlled wall bending, the SME could be quantified by the bending test according to Equation 16 and Equation 17. The skeletons displayed $R_{f,bending}$ = 98.9 ± 1.2% and $R_{r,bending}$ = 99 ± 1% (n = 6). The switching temperature (T_{switch}) was determined by thermally inducing the shape-recovery of programmed skeletons (α_{tem} ≈ 50°) by heating experiments in water, monitoring the shape switching and correlating it with the applied temperature. Accordingly, the T_{switch} measured to be ≈ 49 ± 1 °C (n = 3) (experiment details in 7.3.5).

In conclusion, a controlled programming technique by usage of PDMS molds was established. This process enabled producing a defined, controlled and reproducible temporary shape of re-Hex-SMP skeletons, which subsequently should allow for a defined active biaxial expansion by shape-recovery forces. Accordingly, this mold-based programming method was further applied in this study.

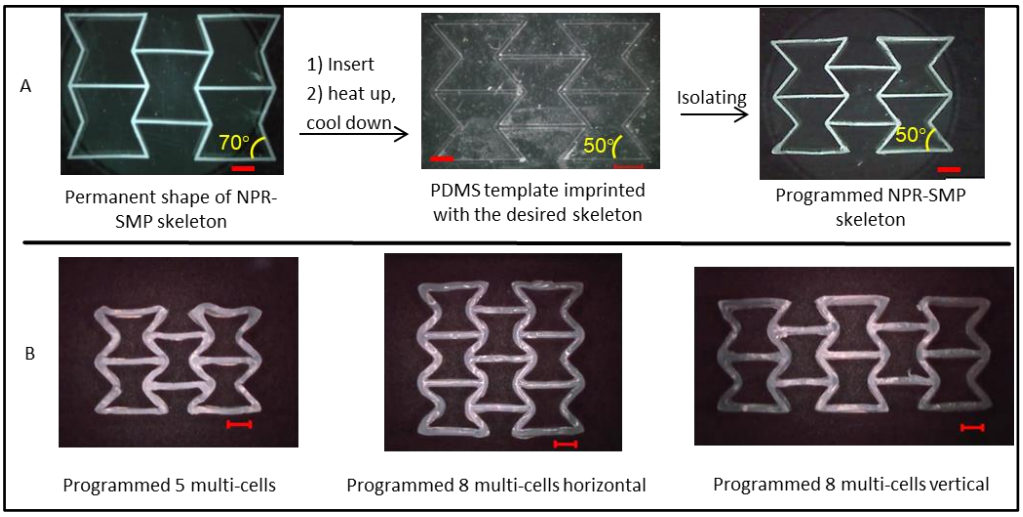

Figure 36. The principle of programming by using a PDMS template. A) Re-Hex-SMP skeleton (cell geometry No. 3, Table 2) programmed from α_{per} = 70° to α_{tem} = 50° ± 2° (n = 3). B) Re-Hex-SMP skeleton (cell geometry No. 12, Table 2) programmed from α_{per} = 90° to α_{tem} = 50° ± 2° (n = 3). $R_{r,bending}$ = 99 ± 1% and $R_{f,bending}$ = 98.9 ± 1.2 % (n = 6). Scale bar is 1 mm.

5.2.4. Effect of angle deformation degree on negative Poisson's ratio and surface area reduction

This part experimentally evaluated the dependency of NPR, surface area, biaxial strains and shape-recovery force on the deformation degree of angles during programming of re-Hex-SMP devices, while section 5.1 estimated the effect of these parameters applied in a theoretical model for design selection. During the programming, each cell deforms from α_{per} = 90° to a predefined degree of α_{tem} (Figure 37), which determines the applicable $\Delta\theta$. After programming, the geometry of each cell had changed from a square (sq) to a re-Hex shape (two symmetrical isosceles trapezoids). The surface area (SA) of each shape was calculated assuming different α_{tem} (Equation 29 and Equation 30). Mathematically, $sin\ \alpha_{tem} < sin\ \alpha_{per}$ and $cos\ \alpha_{tem} > \alpha_{per}$, thus $SA_{re\text{-}Hex}$ is always smaller than the correlative initial SA_{sq}. Accordingly, the percentage of the surface area reduction (SAR%) was calculated (Equation 31). The NPR was calculated experimentally based on the overall change of biaxial dimensions of the scaffold (Equation 6).

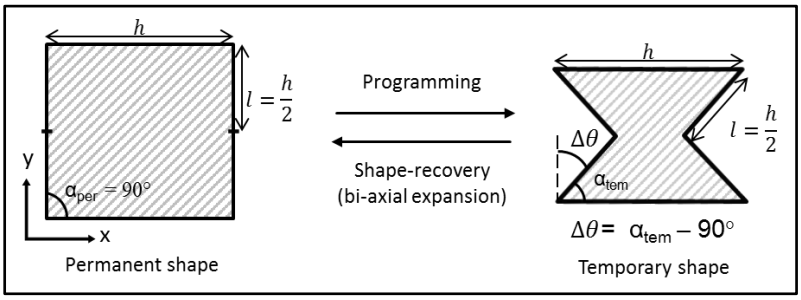

Figure 37. Schematic illustration of geometry change and angle deformation degree (Δθ) during programming/shape-recovery of design No. 12. A) A cell of a square permanent shape. B) A programmed cell of temporary re-Hex. Gray shaded area represents the surface area.

$$SA_{sq} = [l \cdot sin\,\alpha_{per}\,(h - l \cdot cos\,\alpha_{per})]\ x\ 2 \qquad \text{Equation 29}$$

$$SA_{re-Hex} = [l \cdot sin\,\alpha_{tem}\,(h - l \cdot cos\,\alpha_{tem})]\ x\ 2 \qquad \text{Equation 30}$$

$$SAR\% = -\frac{SA_{permanet(sq)} - SA_{temporary(re-hex)}}{SA_{permanent\ (sq)}}\ x\ 100 \qquad \text{Equation 31}$$

As expected, decreasing $\Delta\theta$ reduced NPR values, the magnitude of which is quantitatively demonstrated in Figure 38 A. For a substrate of 8 vertical cells, varying $\Delta\theta$ from -20° to -40° decreased NPR from -0.7 to -1.7, respectively (≈ 2.5 folds). A device of 8 vertical cells exhibited

a higher transverse strain (change in y axis) compared to the axial strain and hence a higher NPR magnitude than other devices. Along with the change of NPR value by altering $\Delta\theta$, also the SAR% is affected (Figure 38 B). In general, decreasing $\Delta\theta$ resulted in decreasing SAR% values. Varying $\Delta\theta$ from -20° to -40° decreased SAR% from -15 to -35, respectively (≈ 2.3 folds). This is preferred in this study as a lower SAR% during programming will lead to a larger increase of the SA during the shape-recovery.

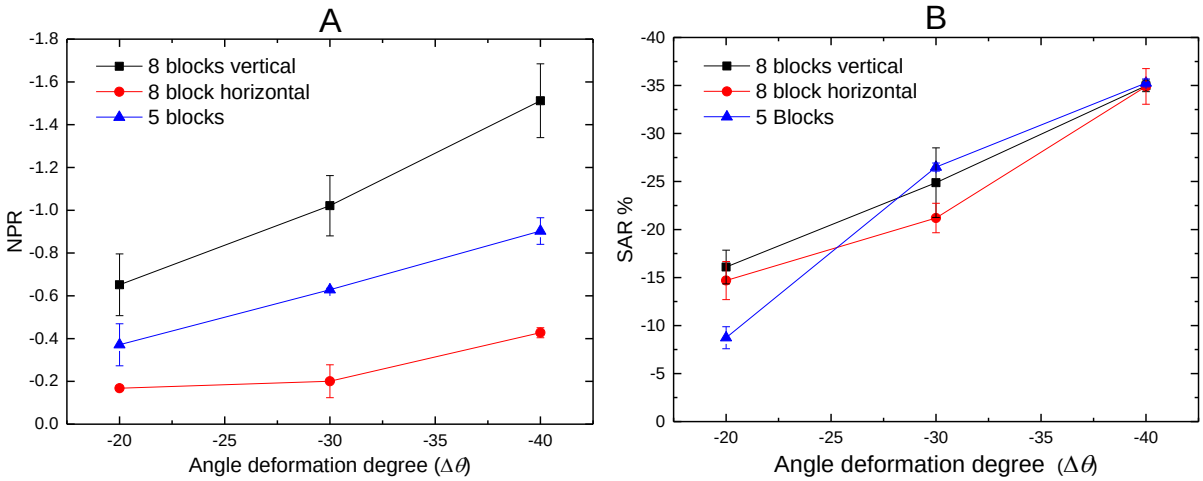

Figure 38. Experimental evaluation of Δθ effect of various re-Hex-SMP skeleton on A) NPR and B) SAR%. Data represented as mean ± SD (n = 3).

In conclusion, by systematically altering $\Delta\theta$, values of NPR and SAR% could be modulated as confirmed experimentally. A substrate of vertical 8 cells with $\Delta\theta$ = -40° exhibited the highest magnitude of NPR and SAR%. Therefore, this structure will be used further in this study.

5.2.5. Effect of angle deformation degree on shape-recovery force and biaxial strains

Concept to determine recovery forces on device level

To allow a coating rupture by the biaxial expansion of re-Hex-SMP devices, the force during the shape-recovery of the device should exceeds the tensile strength (force and strain at break) of the used coating material. Therefore, measuring the force during shape-recovery of re-Hex-SMP scaffold is of interest in order to fabricate a device that achieves the desired function.

Measuring the recovery stress during shape-recovery of SMP-bulk films is widely reported in literature, usually employing tensile testers by inducing shape-recovery while the strain is fixed [36, 37]. Alternative techniques include the use of strain gauges,

microelectromechanical systems (MEMS), e.g. force sensor tips or micro-gripper [38], or analysis of the SMP´s ability to lift a specific weight during shape-recovery [39]. However, the aforementioned approaches appeared not suitable to measure the force of re-Hex-SMP devices. This is because fixation of the re-Hex-SMP scaffold with a hook or clamps in a tensile tester prevents the free biaxial expansion and probably causes sample bending during shape-recovery. Therefore, an alternative measuring set-up was assembled, which allowed measuring the shape-recovery force of re-Hex-SMP skeleton in air environment. As shown in Figure 39, the set-up consists of a hotplate, on which the re-Hex-SMP skeleton was placed horizontally and was in tangent with the tip of a load cell. A barrier directed the sample movement towards the sensor tip when strain free shape-recovery was induced (experiment detail in 7.3.6).

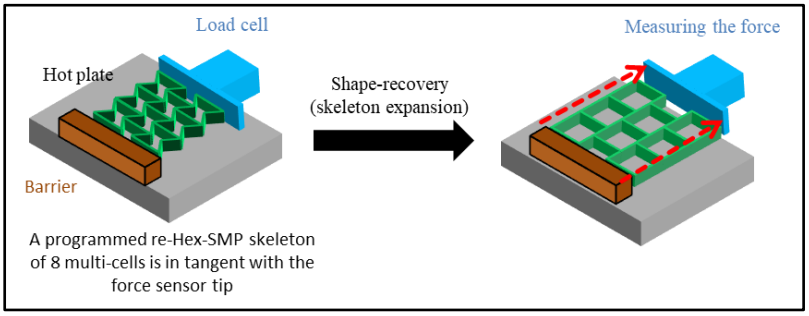

Figure 39. A schematic illustration of experimental setup for measuring the shape-recovery force of re-Hex-SMP skeletons.

As mentioned in the strategy (section 3.2), the values typically presented in literature are the stress during shape-recovery, and not the recovery force. The majority of the SMP examined in literature have a regular cross-section by using film shaped samples, which allow to calculate the stress = force/cross-section area. However, this approach was not applicable in this study as the re-Hex-SMP skeleton composes of aligned cavity-cells (irregular cross-section); therefore, the shape-recovery of the scaffolds will be characterized by the force created on the device level.

Effect of $\Delta\theta$ on the force and biaxial strains of re-Hex-SMP device during shape-recovery

As the re-Hex-SMP device of 8 vertical cells (shown in Figure 36 B, corresponds to design No. 12 in Table 2) showed the highest NPR magnitude, it has been selected for the experimental evaluation of the strain and force produced via the biaxial expansion during shape-recovery. This analysis showed that decreasing the value of $\Delta\theta$ (increasing hinge bending) during programming will increase the force of shape-recovery. For the re-Hex-SMP device of 8 vertical cells, decreasing the $\Delta\theta$ = - 20° to $\Delta\theta$ = - 40° increased the released force of the

skeleton from ≈ 35 ± 18 mN (n = 6) to ≈ 334 ± 70 mN (n = 6), respectively as shown in Figure 40 A. The force of a single cell and of one angle (hinge) can be calculated by dividing the force determined for the entire scaffold by the number of its cells and its angles. For instance, from the re-Hex-SMP device of 8 vertical cells with $\Delta\theta$ = - 40°, the force of a single cell and of a single angle were calculated to be ≈ 41 ± 8.7mN (n = 6) and ≈ 7 ± 1.4 mN (n = 6), respectively, as shown in Figure 40 A. The error bars of the force calculated per cell and per angle (labeled with asterisk in Figure 40 A) represent the propagation of SD of the measured force form the corresponding skeletons (8 multi-cells vertical). The propagation of SD was calculated according to Equation 43 in section 7.4.

Furthermore, the produced bi-dimensional strains during shape-recovery were characterized. Lower, i.e., more negative $\Delta\theta$ showed increased biaxial strain. At the level of an individual cell, re-Hex-SMP skeletons programmed to $\Delta\theta$ = - 20° produced a strain in x- and y-axis of ≈ 20 ± 5% and ≈ 5 ± 1%, respectively, during the shape-recovery. Interestingly, for the same skeletons, reducing $\Delta\theta$ during programming from -20° to -40° (higher deformation) produced a strain in x and y axis during the shape-recovery up to ≈ 103 ± 12% and ≈ 16 ± 1.6%, respectively, as shown in Figure 40 B.

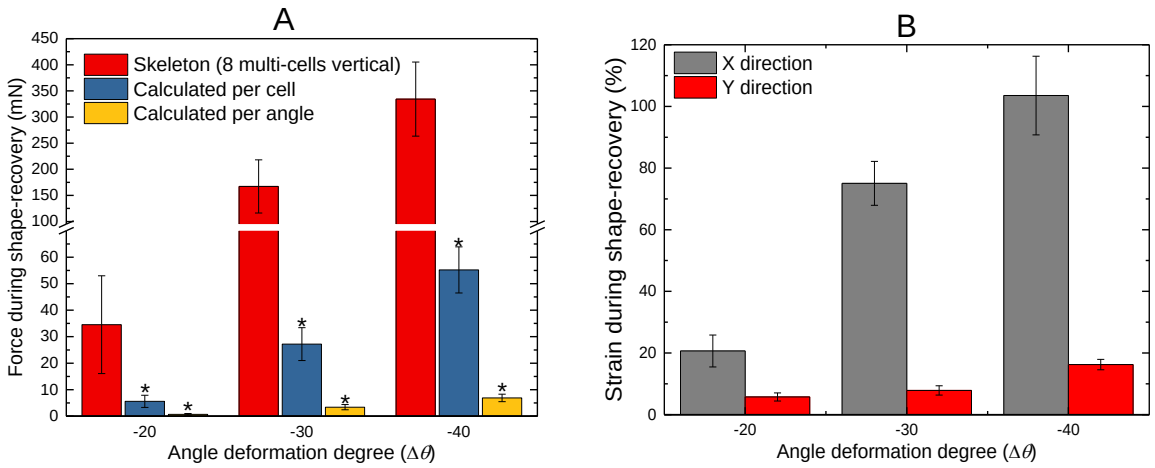

Figure 40. Switching force and biaxial strain of re-Hex-SMP skeletons (design No. 12 with 8 vertical cells) depending on $\Delta\theta$ applied during programming. A) Force during shape-recovery (n = 6) as measured for the skeleton, from which the values per cell and per angle were calculated. Error bars labeled with asterisk (*) represent the propagation of SD of the measured force form the corresponding skeletons. B) Biaxial strains during shape-recovery (data represent the strain at individual cells) (n = 6); Data represented as mean ± SD. Typical experimental error of the load cell is ± 1 mN.

To enable the functionality of the system, the skeleton should be designed to provide high values of NPR and F_{rec}upon actuation. By applying the hinge model as a guideline for the experimental design (see Table 2), it was detected that increasing t and b and decreeing $\Delta\theta$

during programming should enhance values of NPR and F_{rec}. In this section, the dependency of NPR, $F_{rec\ (substrate)}$ on $\Delta\theta$ was explored and experimentally quantified. Results showed that decreasing $\Delta\theta$ from -20° to -40° (higher angle bending) increased the magnitude of NPR from -0.7 to -1.7, SAR from -15% to -35% and $F_{rec\ (substrate)}$ from 34 mN to 334 mN, which is preferred for the device functionality. When considering the initial task to maximize the shape-recovery force and the NPR upon stimulation, the presented results have provided evidence on how this task can be solved. As programmed substrates (vertical 8 cells) of $\Delta\theta$ = -40° showed the highest magnitudes of NPR, SAR%, shape-recovery force and biaxial change of dimensions, they were further explored as switchable multi-reservoir devices.

5.3 Coating of re-Hex-SMP devices

5.3.1. Formation of intermediate layer

The formation of a breakable coating layer over the cavities of the re-Hex-SMP skeleton in the compressed (programmed) state has been identified as a scientific and technical challenge. Beside the requirements on terms of mechanical properties, the coating material should be hydrophobic, neither promote swelling nor inducing shape-recovery and should form a confluent sealing layer of relatively low thickness.

Based on the previous discussion in section 4.2, PDA was applied as an intermediate layer. The re-Hex-SMP skeleton was treated with PDA by immersing in a dopamine solution (experimental details in 7.3.7), which resulted in the surface modification of all walls of the skeleton. After the treatment, the color of the skeleton has been changed to brownish, which visually confirmed the polymerization of dopamine to PDA (Figure 41 A and B) (experiment detail in 7.3.7). Additionally, transmission electron microscopy (TEM) (Figure 41 C) of a cross-section of the treated device visualized the PDA layer, which was determined to have a thickness of 180 ± 53 nm (n = 1 with 11 measuring values). Moreover, the formation of a PDA layer on devices was confirmed by FTIR. The red line in the FTIR spectrum (Figure 41 D) refers to the PDA-coated device (re-Hex-SMP device-PDA; n = 1) and is compared to a uncoated control. Two small peaks at wavenumber of 1520 cm^{-1} and 1622 cm^{-1} may be assigned to N-H bending vibration and suggested the presence of aromatic amines (see Figure 26) in the deposited PDA film, while the broad band from 3000 to 3500 cm^{-1} refer to O-H and/or N-H stretching vibrations of PDA [156].

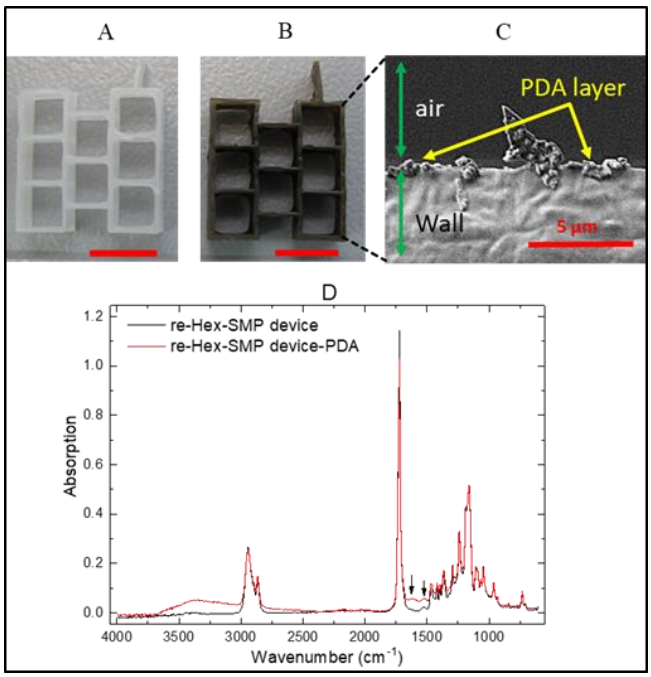

Figure 41. A) A macroscopic image of re-Hex-SMP device before treatment with PDA and B) after PDA coating (brownish), the grip is for skeleton handling. Scale bar is 5 mm. C) TEM image at a cross-section of the coated device showing the PDA layer on the surface of the wall. PDA thickness is 180 nm ± 53 (n = 1 with 11 measuring values). D) FTIR spectroscopy of the re-Hex-SMP device (n = 1) before and after treatment with PDA. Peaks at 1520 cm^{-1} and 1622 cm^{-1} (arrows) refer to N-H bending of aromatic amine in the deposited PDA film. The broad band from 3000 to 3500 cm^{-1} was assigned to O-H and N-H stretching mode.

5.3.2. In-situ polymerized coating: coating materials and thickness

Various CA-based materials with different side chains were considered in this study. Table 3 shows the chemical structures of the evaluated CA-coating materials, which should be characterized for determining the suitable polyCA to be applied as sealing layer of reservoirs in the switchable device. The polyCA coating materials will be characterized in term of (i) the effect of the number of coating cycles on coating thickness and (ii) the effect of polyCA side chains on breakability of the coating as the nature of the side chains affect the molecular packing and thus affect the polymer's mechanical and thermal properties [116].

Table 3. Chemical structure of cyanoacrylate monomers used in this study for application of the coating.

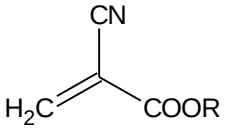

	CA-monomer	R	Monomer abbreviation	polyCA abbreviation
1	Methyl CA	$-CH_3$	MCA	PMCA
2	Ethyl CA	$-CH_2-CH_3$	ECA	PECA
3	Butyl CA	$-CH_2-CH_2-CH_2-CH_2$	BCA	PBCA
4	Methoxyethyl CA	$-CH_2-CH_2-O-CH_2$	MECA	PMECA
5	Ethoxyethyl CA	$-CH_2-CH_2-O-CH_2-CH_2$	EECA	PEECA

To avoid premature coating breaking during the coating formation steps and to enable device handling for the on-demand dosing study, the re-Hex-SMP skeletons were refabricated with a grip (see Figure 41 B). The PDA treated re-Hex-SMP skeletons were filled manually by a

micropipette with a molten (40 C°) PEG (Mw = 1000; PEG_{1000}), which then solidified in the reservoirs at room temperature. The coating of polyCA was formed by casting a CA-monomer solution (in hexane) over the loaded reservoirs followed by evaporating the solvent (experimental details in 7.3.8). Hexane was chosen as solvent because it dissolves the CA-monomer but does not freely dissolve the formed polyCA. Besides, hexane does neither swell nor induces the shape-recovery of the device.

Effect of number of coating cycles on coating thickness

Coating the re-Hex-SMP device with several cycles may be advantageous to achieve the desired thickness of polyCA layer and to fill any potentially uncoated areas and spaces that might have remained from the previous coating cycle. It is significant to understand how the number of coating cycles affects the coating properties. For each CA-monomer (concentration of 1% v/v in hexane), the corresponding polyCA was formed on re-Hex-SMP devices (experiment detail in 7.3.8). By applying increasing numbers of coating cycles, e.g. 1, 2, 4, 8 and 16 cycles, the different coating thickness was determined at cross-sections by scanning electron microscopy (SEM) (Figure 42 A). The formed coating layer characterized by a bulk film structure with an inhomogeneous surface morphology as shown in Figure 42 B. The dependency of the coating thickness on the number of the coating cycles is presented in Figure 42 C. Results indicated that coating thickness systematically increased with increasing the cycle number in a nearly linear relation. For instance, 8 coating cycles of PBCA resulted in a thickness of ≈ 6 ± 1.5 µm, while 16 cycles gave ≈ 12 ± 2.5 µm.

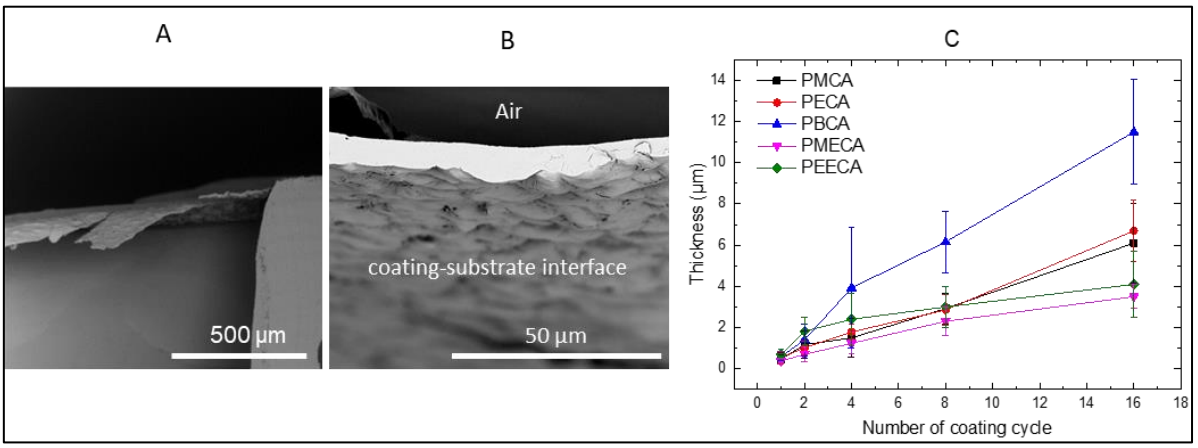

Figure 42. A) Exemplary SEM image of PECA coating after 16 coating cycles over the re-Hex-SMP device. B) Magnified view of the coating layer showing the inhomogeneous surface morphology (globules structure) at the interface of the previously filled cavity and the coating. C) Effect of the number of coating cycles on coating thickness for various CA-polymers. Data represented as mean ± SD (n = 6).

Despite all examined polyCA films were prepared under the same condition and with same concentration of the monomer solution, the formed coating films exhibited different thicknesses at a specific coating cycle number. For instance, at 16 coating cycles, PBCA and PECA exhibited an average thickness ≈ 12 ± 2.5 µm and ≈ 7 ± 1.5 µm, respectively. This variation in thicknesses among obtained polyCA may be attributed to the effect of the spreadability of CA-monomers (due to the interfacial tension) and their rate of interfacial polymerization as reported in literature [157]. On a hydrophilic surface, herein PEG and PDA, CA-monomers with longer alkyl side chains (more hydrophobic), e.g. BCA, have a lower spreadability and a lower rate of polymerization than shorter side chains, which gives a film with a higher thickness. In contrast, for MECA and EECA as hydrophilic monomers with an ether group, a higher spreadability and higher rate of polymerization are assumed having led to films with lower thicknesses.

As the change in temperature may alter the mechanical properties of polyCA and thus may affect their breakability during the thermally induced shape-recovery of the device, the thermal properties of polyCA coating materials were evaluated by DSC (experiment detail in 7.3.11) and summarized in Table 4, confirming lower T_g for PCA with more flexible side chains.

5.4 In-situ analysis of mechanical properties of the coating layers

Experimental setup

Understanding how different parameters affect the coating properties and breakability is a key step to rationalize and control the functionality of the system. Therefore, the mechanical properties of the coating such as the strain a break (ε_B) and force at break (F_B) should be analyzed under conditions predictable for the final device.

The mechanical properties of polyCA have been studied in literature [158, 159] often by measuring the shear stress via applying CA monomer as glue between two sides of specimens, which are subjected to a tension load. In this study, as the coating layer should be a breakable thin film, which is fragile by purpose. Handling such very thin free-standing films for determining the mechanical properties by conventional methods, e.g. by a tensile tester, is not possible. Additionally, the interest is in determining the mechanical properties of polyCA coating as-formed, i.e. the polyCA membrane fixed at the boundary of the re-Hex-SMP skeletons. For this purpose, a setup was specifically adapted for examining the mechanical

properties of the coating layers directly after formation on the re-Hex-SMP skeletons in situ by a micro-indentation technique (experiment detail in 7.3.10). To allow for such a measurement, a MEMS micro-force sensing probe connected to a micromanipulator, which allows for micro-movement (micro-indentation), was employed under an inverted microscope (Figure 43).

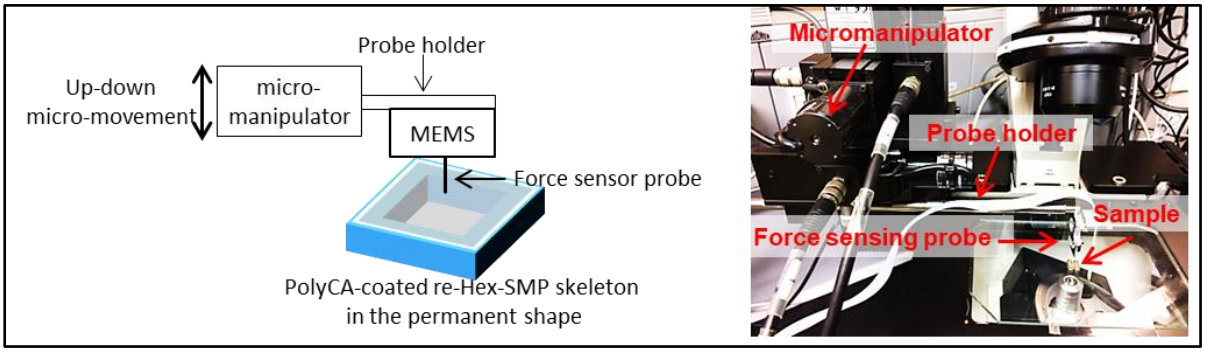

Figure 43. Principle of mechanical characterization of coating layer. Left: Schematic illustration of micro-indentation setup. Right: Experimental setup.

Applied model for analyzing E modulus of polyCA coating materials

To allow for both experimental handling and data analyzing by a suitable model, a geometry should be selected that is closely related to the used re-Hex-SMP skeleton and at the same time is not too complex. Therefore, the coating is treated as a clamped thin membrane of square shape corresponding to the cell geometry of devices in their permanent shape. Load-unload indentation experiments were performed on the membrane to determine the deformation type of thin polyCA layers, i.e. distinguish elastic or plastic deformation. The coting layer was formed by first filling the cavity of the re-Hex-SMP with a molten PEG_{1000}, which will be solidified at room temperature (≈ 25° C). Then, e.g., an ECA monomer solution was spread over the solidified PEG_{1000} in a total of 16 coating cycles (experimental detail in 7.3.10). Dissolving the PEG in water resulted in a free-standing PECA membrane over the cavities of the re-Hex-SMP skeleton. The PECA coating membrane was indented up to 25 µm in 3 cycles to obtain the load-displacement curves (Figure 44). The results showed that by releasing the applied load, the measured force returned to zero, which indicates an elastic recovery of the membrane to its initial state.

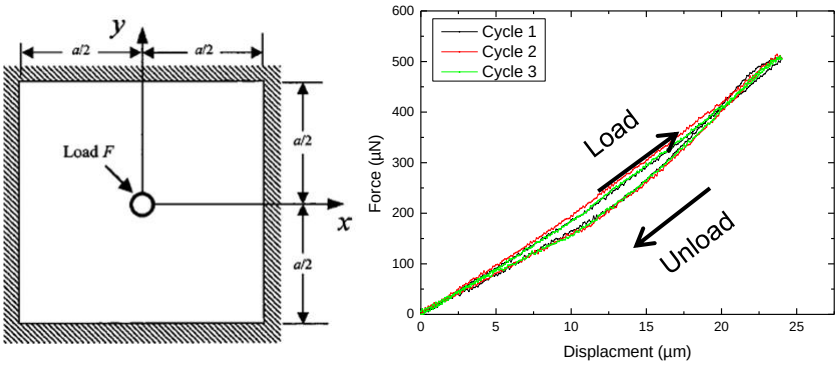

Figure 44. Left: Schematic illustration of the geometry of a polyCA coating membrane upon indentation on a cell of the re-Hex-SMP in the permanent shape (square shape). Right: Load-unload curve by indentation of PECA coating membrane (formed by 16 coating cycles) on a cell of a re-Hex-SMP device. The coting layer was formed by first filling the cavity of the re-Hex-SMP with a molten PEG_{1000}, which solidifies at room temperature. Then spreading a ECA monomer solution over the solidified PEG (16 coating cycles). Dissolving the PEG in water leads to free-standing PECA membrane over the cavities of the re-Hex SMP skeleton.

Based on load-unload curves, a linear elastic bending model of a square plate clamped at edges was applied for data analysis [160]. According to Equation 32, the centered displacement (w_0) is linked to the applied force (F), the side length (a) of the square and the variables ϑ and k.

$$w_0 = \vartheta \frac{F a^2}{k} \qquad \text{Equation 32}$$

where ϑ is the numerical factor that depends on the geometry and is ϑ = 0.005602 for square-shaped films. k is the bending rigidity defined according to Equation 33.

$$k = \frac{E h^3}{12(1-\nu)} \qquad \text{Equation 33}$$

where ν is the Poisson's ratio of the coating material, assuming $\nu = 0.4$ for CA-based material [125], and h is the thickness of the coating membrane. Substituting k in Equation 32 gives Equation 34. Accordingly, E can be calculated as given in Equation 35.

$$w_0 = \frac{\vartheta\ F\ a^2\ 12\ (1-\nu)}{E\ h^3} \qquad \text{Equation 34}$$

$$E = \frac{\vartheta\ F\ a^2\ 12\ (1-\nu^2)}{h^3\ w_0} \qquad \text{Equation 35}$$

Effect of polyCA side chain on E modulus

The quantitative in-situ analysis of the E modulus of polyCA coating membranes by the selected setup clearly demonstrated the effect of different side chains on the E modulus of polyCA (Figure 45). Increasing the length of the side chain decreases the E modulus.

Introducing an ether group in the side chain as shown for PMECA and PEECA, also reduced the E modulus of the polymer. That may refer to the flexibility of ether linkage as the lack of the substitution of the chain with hydrogen atoms at oxygen ether links provides more free space and promotes ease of rotation and consequently enhances polymer flexibility [161]. In this study, the applied micro-indentation technique allowed determining the mechanical properties of polyCA materials in form of thin membranes, which is considered as a challenge due to the material`s properties that restrict the analysis of free-standing samples by conventional techniques so far. The obtained results by this technique are consistent with the literature [116, 159], in which the mechanical properties were determined in a tensile tester by measuring the shear stress of polyCA when acting as glue between metal plates.

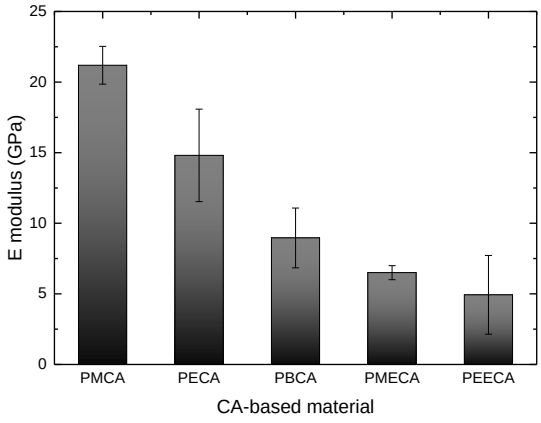

Figure 45. Elastic modulus of polyCA films (made of 16 coating cycles) with different side chain. Data quantified by Equation 35. Data represented as mean ± SD (n = 3).

Determining the force and the strain at break

In the next step, ε_B and F_B should be determined by indenting the coating at the middle of the square-shaped frame until breakage. To quantify the ε_B, the centered displacement of the coating should be converted to a strain value. That was achieved by applying the pythagoras's theorem of a triangle ($hypotenuse^2 = \text{adjacent}^2 + \text{opposite}^2$). During the indentation at the center of the coating membrane, since the coating is fixed at the boundary, the membrane will be stretched to form a triangle shape at a cross-sectional view (red triangle in Figure 46 B). The opposite and the adjacent of the triangle are known values, which refer to the half length of the membrane (a/2) and to w_0, respectively. The hypotenuse of the triangle correlates to the stretched length a/2 of the coating membrane. Therefore, the strain can be calculated according to Equation 36:

$$Strain\ \% = \frac{(2\ x\ hypotenuse) - a}{a} x\ 100 = \frac{\left(2x\sqrt{(0.5\ a)^2 + \ (w_0)^2}\ \right) - a}{a}\ x\ 100 \qquad \text{Equation 36}$$

Based on Equation 36, the results were presented as a force against percentage strain as shown in Figure 46 C. The coatings from PMCA and PECA were concluded as the most brittle among the examined polyCA as they displayed the lowest F_B values (2.4 ± 1.6 mN and 4.1 ± 2.2 mN, respectively) and lowest ε_B (0.4 ± 0.05% and 0.3 ± 0.2%, respectively). As PBCA has a longer and thus more flexible side chain resulting in a presumed less order packing, it displayed large deformability and exhibited ε_B of 0.85 ± 0.3% and F_B of 4.5 ± 2.0 mN. PolyCAs that contain alkoxy group in their side chain, i.e. PMECA and PEECA, displayed even higher F_B (≈ 7.3 ± 1.9 mN and 7.6 ± 0.3 mN) and higher ε_B (4.6 ± 0.5% and 1.5 ± 0.3%, respectively) due to their flexibility.

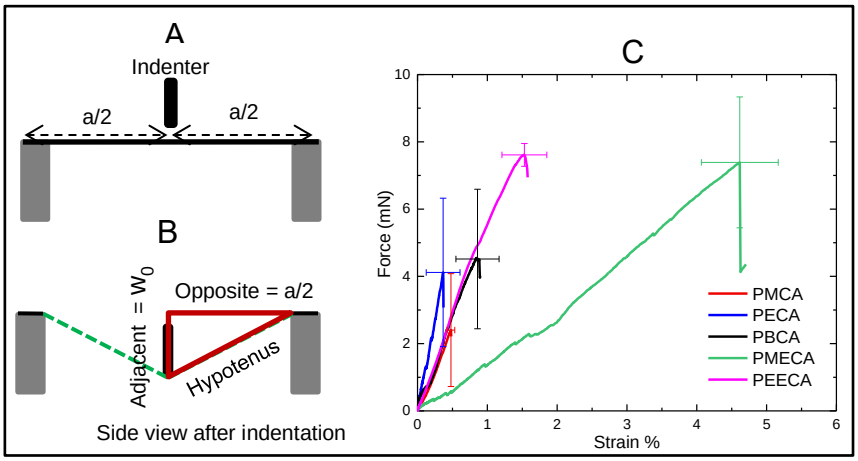

Figure 46. Principle of determining the strain during indentation based on pythagoras's theorem. A and B are schematic side view of the coating membrane before and after indentation, respectively. The hypotenuse represents a half of the strained membrane length. C) Force against the strain by membranes indentation up to break. Each polyCA membrane was obtained by 16 coating cycles. Data represented as mean ± SD (typical experimental error of the force sensor probe is 0.5 mN).

Table 4: Summary of polyCA coating characterization. Data represented as mean ± SD.

polyCA	Thickness (µm)[a]	T_g (°C)	E modulus[a] (GPa)	F_B[a] (mN)	ε_B[a] (%)
PMCA	6.1 ± 1.9	n.d. [b]	17.1 ± 4.1	2.4 ± 1.6	0.47 ± 0.05
PECA	6.7 ± 1.5	122 [c]	15.8 ± 3.0	4.1 ± 2.2	0.36 ± 0.2
PBCA	11.5 ± 2.5	99 [c]	8.0 ± 1.6	4.5 ± 2.0	0.85 ± 0.3
PMECA	3.5 ± 0.5	68 [d]	6.5 ± 0.5	7.3 ± 1.9	4.6 ± 0.5
PEECA	4.1 ± 1.5	62 [d]	4.5 ± 0.9	7.6 ± 0.3	1.5 ± 0.3

[a] Measured for films with an average thickness of 16 coating cycles.
[b] Not detectable.
[c] Heating rate is 10 K·min^{-1}
[d] Heating rate is 20 K·min^{-1}

5.5 Functional evaluation of re-Hex-SMP dosing system

5.5.1. Balancing produced and demanded force and biaxial strain to break the coating

Of particular interest is comparing the force and the strain that were obtained during the shape-recovery of non-coated re-Hex-SMP devices at different $\Delta\theta$ values with the demanded F_B and ε_B to break polyCA coating layers. As shown in Figure 47 A, the y-axis strain (green bars) produced from a cell of re-Hex-SMP skeleton with $\Delta\theta$ = -20° is in the range of the strain at break (red bars) of PMECA coating and the strain was slighter higher for cells of re-hex SMP with $\Delta\theta$ = -30° and -40°. The x-axis strain (Figure 47 A, blue bars) produced during the shape-recovery of an individual cell of re-Hex-SMP skeletons of different $\Delta\theta$ clearly exceeds the strain at break of different polyCA materials. Interestingly, the force produced from re-Hex-SMP skeleton of $\Delta\theta$ = -20° (Figure 47 B) is only in the range of F_B of PBCA coating and even less than the F_B of PMECA and PEECA films. This indicates that re-Hex-SMP skeleton of $\Delta\theta$ = -20° may not enable the function of the systems. On the other hand, individual cells of re-Hex-SMP of $\Delta\theta$ = -30° and -40° produce forces that should exceed the previously determined F_B of all examined polyCA coating membranes.

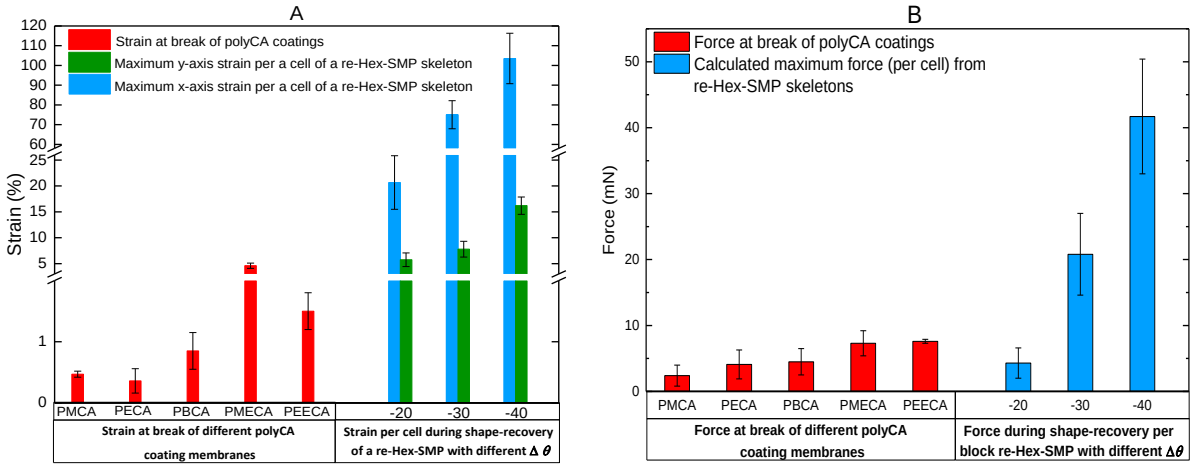

Figure 47. Strain and force that are produced during shape-recovery of a re-Hex-SMP cell with different Δθ values in comparison to strain and force that are required to break polyCA coating membranes. A) Strain comparison. B) Force comparison. Data as obtained from model studies in section 5.2.5 and 5.4.

Figure 47 indicates, conceptually, the ability of SMP-NPR device of $\Delta\theta$ = -40° to induce coating failure during shape-recovery. However, the question remains, if stimulation of a coated re-Hex-SMP device allows transferring the strain and force from shape-recovery to the coating layer and thus induce coating rupture? This question was experimentally answered by

exploring programmed re-Hex-SMP devices of 8 vertical multi-cells, which were coated with different polyCA (16 coating cycles) (experimental detail in 7.3.9). By stimulating the shape switching of the devices in an aqueous environment, all devices were able to undergo biaxial expansion and recover their permanent shape (Figure 48). These experiments indicated that the coating process and materials do not impair the SME effect. Additionally, the results emphasized the validity of a part of the hypothesis, which is the transfer of the mechanical deformation of the device to a failure of the coating.

Coatings made from PMCA, PECA and PBCA were completely ruptured after shape-recovery, as expected. Interestingly, PMECA and PEECA were stretched over the cavities without rupturing. This behavior is surprising as it is in contrast to expectations based on comparing the data of mechanical analysis by micro-indentation in relation to surface area change of the SMP skeletons upon switching (compare Figure 47). This behavior may refer to the aqueous environment (water) that may act as a plasticizer, particularly for PMECA and PEECA allowing for hydrogen bonding by ether groups in their side chains, thus result in a reduced T_g [135]. Additional reason might be the thermal effect as the device switching occurs at T_{switch} ≈ 49 °C, which is close to the onset of T_g of coating films and may alter their mechanical properties, while the analysis of PCA mechanics was conducted at room temperature. A further examination of polyalkoxy-CA deformation by the micro-indentation test at an elevated temperature (at $T = T_{switch}$) may provide a comprehensive explanation for the stretching behavior of PMECA and PEECA upon device stimulation.

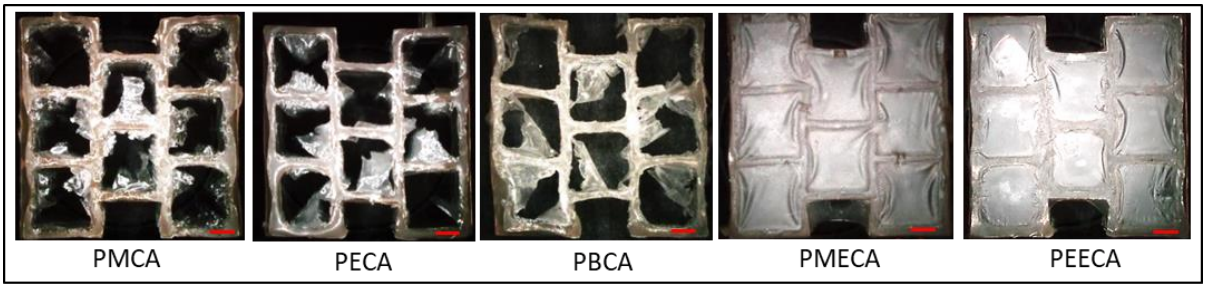

Figure 48. Images after shape-recovery in aqueous environment for re-Hex-SMP substrates coated with different polyCA (each coating is formed by 16 coating cycles). PMCA, PECA and PBCA coating were ruptured after shape-recovery. While PMECA and PEECA were stretched over the cavities after shape-recovery. Scale bar = 1 mm.

The most observed scenario of coating failure upon a thermal stimulation under water is shown in Figure 49 (experimental details is in 7.3.9). The first step of coating rupture is cracks initiation. Upon stimulation, the angles of the device previously programmed to 50° started

to open up and recover to the permanent shape of 90°, which led to initiation of coating cracks at corners sites (Figure 49 B and C). With further opening up of angles, the cell bi-axially expanded and the coating experienced a biaxial stretching causing a diagonal-like propagation of the cracks from the corners to the center of the cell eventually leading to a total rupture of the coating layer (Figure 49 D and E). It is well known that biaxial stretching results in about 45-60% lower tensile strength compared to uniaxial stretching [162], which here has been successfully facilitated to induce rupturing. Additionally, before stimulating the re-Hex-SMP device (Figure 49 A), the coating layer has an anisotropic shape as it adapted the shape of each re-Hex cell, i.e. the coating layer has a re-entrant hexagon shape, which causes a non-uniform stress distribution upon biaxial stretching. In this context, it should be noted that the site of crack initiation and the path of the crack propagation is not always identical. That may refer to the morphology (globular structure) of coating-substrate interface (see Figure 42 B), which has a distribution of weak spots at different globules-junction sites statistically formed during CA polymerization.

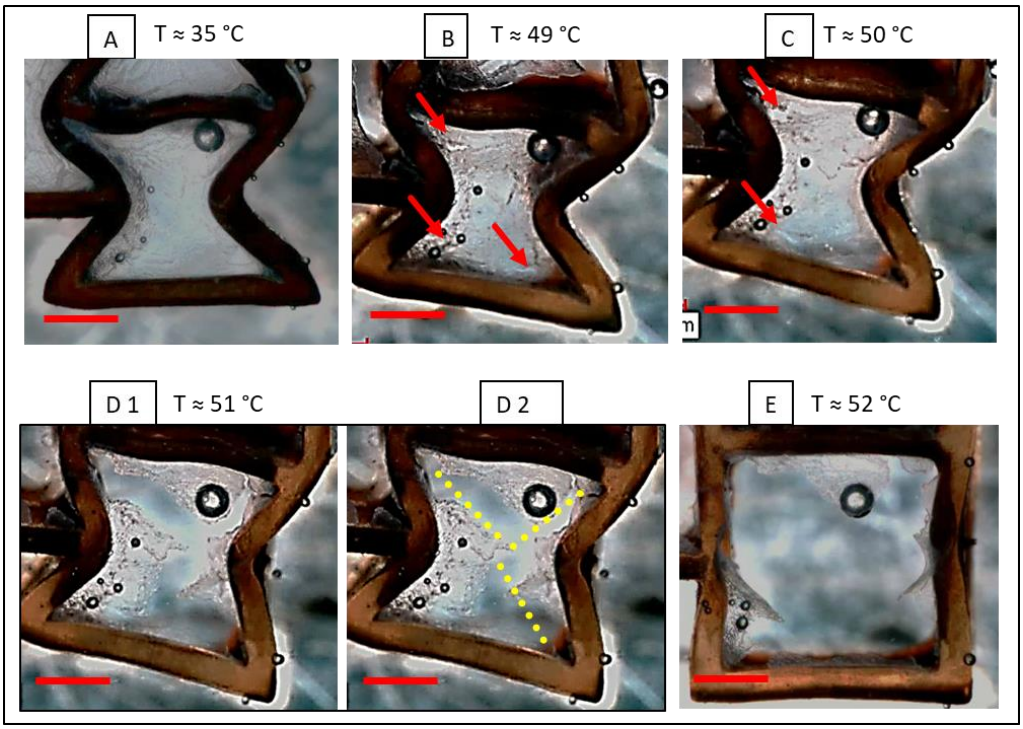

Figure 49. Microscopic images showing the steps of the coating failure upon a thermal stimulation of a coated re-Hex-SMP device. A) Microscopic image of the PBCA coating (16 coating cycles) over 1 cell of a programmed (from 90° to 50°) skeleton with 8 cells-SMP. B and C) Images of cracks initiating in the coating layer at sites of corners (red arrows) and propagation to the middle of the cell as a result of the biaxial expansion of the cell. D 1 and D 2) Microscopic images of total coating rupture. D 2 is identical to the image D 2 with the yellow dashed lines indicating the diagonal-like propagation/rupture. E) Image of the re-Hex cell recovered to the permanent shape (90° angles) with totally ruptured coating layer. Temperature ramping rate was 6.5 K/min. Scale bar is 1 mm.

5.5.2. On-demand compound release

The ability of a free-standing device to rupture its sealing layer on-demand may enable a self-sufficient, reservoir-based dosing system, which can be triggered in a non-contact mode to initiate compound liberation.

At first, the structure-function relationships of the re-Hex-SMP skeletons were evaluated at the level of an individual cell, e.g. comparing F_{rec} and biaxial strain to the mechanical properties of the coating materials (see Figure 47). It was assumed that 1 cell of re-Hex-SMP skeleton is able to break the coating of PBCA and thus should allow compound release. To demonstrate such a system, one-cell re-Hex-SMP devices were programmed to a compressed state of $\Delta\theta$ = -40° (from α_{per} = 90° to α_{tem} = 50°), treated with PDA, and loaded with a dye (methylene blue) as a model compound to visualize the onset of dosing. A loading mixture of methylene blue (30 mg/ml in water) with a molten PEG_{1000} (40 °C) was prepared at a volume ratio of 3:7, respectively, which gives a liquid mixture at room temperature. Each reservoir (cell) was loaded manually with 10 µl of the loading solution by a micropipette. Devices were placed for 24 h under the fume hood for water evaporation, which produced a blue and solidified PEG matrix in each reservoir. Thereafter, the devices were coated from both sides with PBCA (16 coating cycles) (experimental details in 7.3.12). The single-cell devices were subsequently held at the grip and immersed in an aqueous medium under stirring (Figure 50 A). Increasing the temperature (heating rate 6.5 K/min) of the solution up to the switching temperature (Figure 50 B and C, T ≈ 50 °C) activated the SME and induced shape-recovery as visible by the biaxial expansion of the substrate. The initiation of a dye release could very clearly be observed. This indicated the shape switching of the SMP device has been sequentially coupled with coating failure as planned during the design stage, which confirmed the hypothesis of this study to implement an on-demand dosing function via micro-structured free-standing polymer devices (Figure 50 D).

It should be noted that the PEG-based filling is liquid at the switching temperature, suggesting that it can easily follow deformations of the scaffolds during shape switching. Based on the compound release video showed in Figure 49 and 50 compared to previous experiments with unloaded scaffolds (Figure 48), it is demonstrated that the filling had no relevant influence on

shape-recovery capability, suggesting neither effects on the SME performance nor on the force and biaxial strain produced during the shape-recovery.

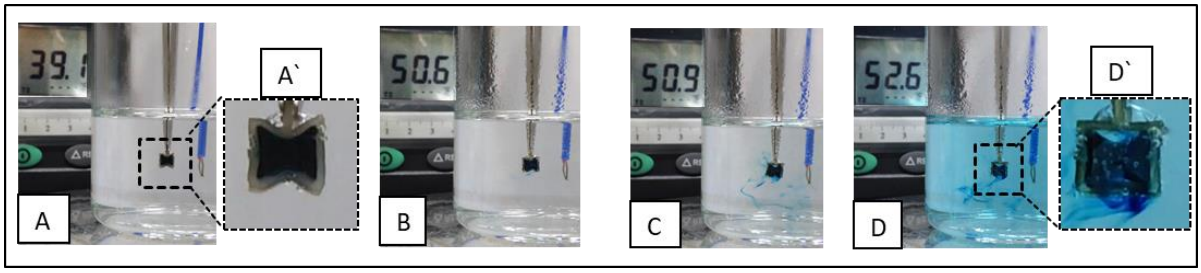

Figure 50. Experimental demonstration of functionality of the on-demand dosing system at level of 1 cell-re-Hex-SMP with Δθ = -40° (programmed from 90° to 50°). A) A cell is loaded with a blue dye (methylene blue), coated from both sides with PBCA (16 coating cycles) and placed in a water bath on a hot plate. A`) A magnified view of the re-Hex cell. B-D) Heating experiment (heating rate 6.5 K/min). When the temperature reached the switching temperature, shape-recovery (biaxial expansion of the cell, image B-C) was induced, cell deformed from a re-Hex shape to a square shape causing coating failure and payload release. D`) is a magnified view of the re-Hex-cell after shape-recovery (biaxial expansion).

As the function of the dosing system was linked to the fundamental re-Hex-SMP cell design, connecting multiple cells together should not impair the functionality of the system. In other words, the system should be scalable with re-Hex-SMP devices of multi-cells design, despite there are some jointed walls and angles. In order to proof that, a re-Hex-SMP device of 8 vertical multi-cells was programmed to a compressed state of $\Delta\theta$ = -40°, treated with PDA and loaded with a dye (methylene blue) (experimental details in 7.3.12). The device was immersed in an aqueous medium and subjected to heating as shown in Figure 52, which demonstrated the on-demand dosing function from multi-cells re-Hex-SMP device upon a thermal stimulation. That confirmed experimentally that the number of the cells in the re-Hex-SMP device (e.g. 5 cells or 8 cells, see Figure 32) had no influence on the system functionality.

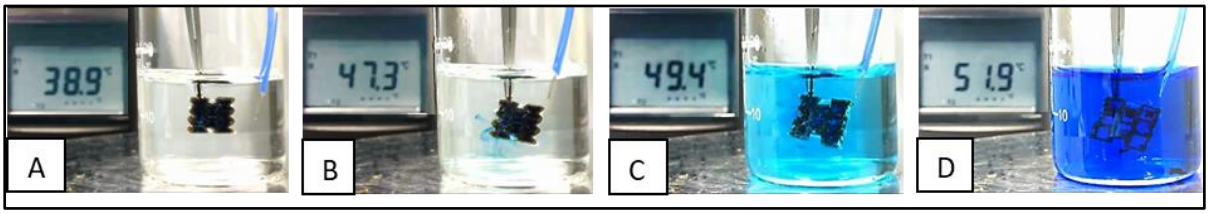

Figure 51. Experimental demonstration of on-demand dosing function of re-Hex-SMP switchable device of 8 vertical multi-cells. A) A device is loaded with a blue dye (methylene blue), coated from both sides with PBCA (16 coating cycles) and placed in a water bath on a hot plate. B-D) Heating experiment (heating rate 6.5 K/min). When the temperature reached the switching temperature, shape-recovery by biaxial expansion of the device (onset in image B) is induced.

During the on-demand dosing from the re-Hex-SMP devices of multi-cells, it was observed that the cells at the outer corners of the devices (Figure 52, cells with number 1) start the shape-recovery slightly before the cells in the middle (Figure 52, cells with number 2). This observation may be explained by heat transfer kinetics from the medium to the material as linked to the surface contact area (SCA) of the respective cells with the aqueous environment. Cells of number 1 have a higher SCA (red lines) with the heated water bath than cells of number 2 (green lines).

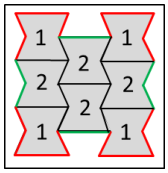

Figure 52. Schematic view of a loaded and coated re-Hex SMP showing the surface contact area of the cells in a simplified 2D model. Cells at the corner (cell with number 1, red lines) have higher surface contact area than cells with number 2 (green lines).

Timing of on-demand dosing function of re-Hex-SMP switchable device

The self-sufficient dosing system may conceptually enable on-demand release at freely chosen time points. Figure 53 shows release profiles of a model compound (blue dextran) from re-Hex-SMP devices, which were stimulated at different time intervals: after 6 h (black curve), 12 h (red curve), 24 h (blue curve), 48 h (pink curve) and 72 h (green curve) of immersion into water (experimental detail in 7.3.13). Each curve represents the release pattern of three independent devices. As shown, all devices had approximately 15 - 20% of release before stimulation. This may be attributed to an amount of the payload remaining at outer edges of the device during compound loading (as the loading was performed manually) and/or due to compound diffusion from minor coating inhomogeneities or cracks formed in the coating layer during devices handling.

After triggering shape switching of the devices, the payload is released in a bolus mode (from ≈ 20% to ≈ 90%). The approximated 10% of unreleased compound might be attributed to the adsorption of the loaded dye to the coating material, which was observed macroscopically in all devices after release experiments (pale blue color of coating films after 96 h).

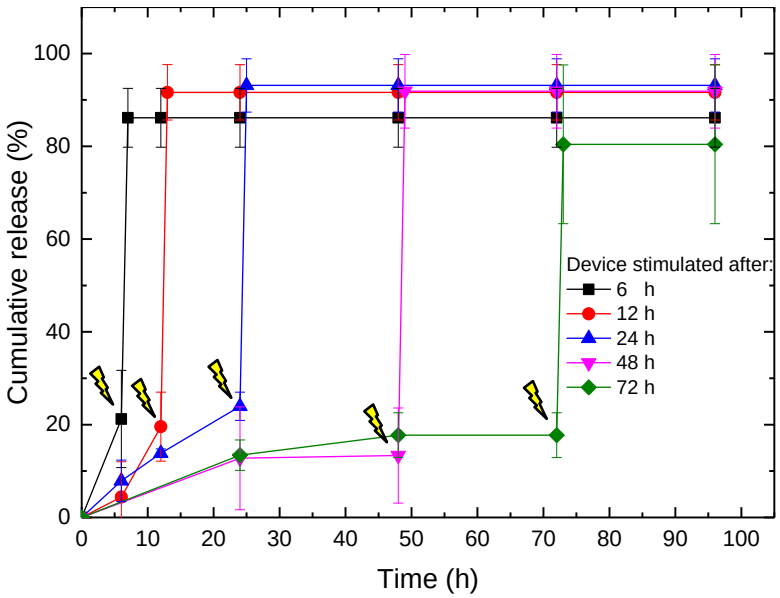

Figure 53. Controlled on-demand dosing from re-Hex-SMP switchable devices with PBCA coating (16 coating cycles). Each curve represents the release of three devices (n = 3). Devices are stimulated after 6 h (black curve), 12 h (red curve), 24 h (blue curve), 48 h (pink curve) and 72 h (green curve). Data represented as mean ± SD.

It should be noticed that the system is functional at the level of an individual re-Hex cell (as demonstrated in Figure 50), however, the function from multi-cells skeletons was presented here as a demonstration of multi-reservoirs devices. The parameters of the design play a key role for enabling the system functionality. Here, the re-Hex structure with parameters of design number 12 ($\Delta\theta$ = -40°, see Table 2) was successfully employed and enabled the desired function. However, similar designs with only one different parameter may be speculated to be non-functional such as design number 10 ($\Delta\theta$ = -20°, see Table 2), for which it is anticipated that the coating breakage is unlikely upon a thermal stimulation (shape-recovery/biaxial expansion) as it produced low F_{rec} as evaluated experimentally (see Figure 47).

In this study, the structure of re-Hex was employed as a prototype design (with respect to the given design parameters) of the device due to its high extent of biaxial expansion and high volume of cavities, which served as switchable containers. However, the concept of the study is not limited to the proposed design. Other NPR structures may be employed with considering the values of bi-axial strain and F_{rec} in relation to the coating materials employed in each case. Along with the design of the device, according to the concept of function coupling (shown in Figure 14 C), modulating the characteristics of the coating (e.g. mechanical properties) may alter the output of the system function as in case of PMECA and PEECA

(shown in Figure 48). In such cases, it is anticipated that stimulating the device will induce shape switching but not a bolus release as the coating will not break but rather be stretched.

Comparing with on-demand dosing systems of multi-reservoirs designs in literature, reported mechanically-induced dosing systems are not free-standing and the dosing is initiated by the aid of integrated materials, e.g. MNPs [111] or electrical interfaces [112, 113]. In contrast, the concept of self-sufficient on-demand dosing devices based on NPR and SMP structures investigated in this study facilitated compound release in a non-contact mode by mechanical opening of reservoirs via biaxially expandable polymer-only devices without electronic parts.

5.6 Summary

The study presented in this chapter described the design, fabrication, characterization and demonstration of a thermally triggerable self-sufficient dosing device based on the concept of sequentially coupled functions. The devices consisted of re-Hex-SMP skeletons, a connecting layer between the skeleton and the coating, and a breakable sealing polymer.

The structure-function relationship of the re-Hex cell geometry was evaluated by employing the hinge model. The effect of the cell parameters on the magnitude of NPR, shape-recovery force was estimated, which provided a guideline for the experimental design of the re-Hex skeletons. Results indicated that design number 12 from Table 2 should provide the highest magnitude of NPR and shape-recovery force.

The matrix of the skeleton was constructed from oCL-IEMA as precursors, which were crosslinked in PDMS molds of a re-Hex design, providing re-Hex-SMP skeletons in the permanent shape. The SME was implemented by programming the skeleton to a compressed state (e.g. programming from α_{per} = 90° to α_{tem} = 50°) via the method of PDMS templates. The effect of the degree of the programmed angle was explored experimentally. Results showed that higher bending of the skeleton walls during programming (lower degree of the programmed angles) increased the magnitude of NPR and shape-recovery force, which is preferred for the device functionality.

The walls of the re-Hex-SMP skeletons were treated with PDA, which enhanced the coating adhesion on the skeleton by contribution to the polymerization initiation of CA-monomer at the surface of the skeleton. PolyCA with different side chains were applied as instantly formed

coating layers. The mechanical properties of the coating layer over the cells of the re-Hex-SMP skeleton were determined in-situ by a micro-indentation method. By this approach, the values of E modulus, force and strain at break were determined for different polyCA materials and were compared with the force and the strain produced during the shape-recovery of re-Hex-SMP skeletons. The breakability of the coating layers was investigated experimentally by thermally stimulation of programed (compressed) re-Hex-SMP skeletons coated with different polyCA materials. It was demonstrated that the mechanical deformation (biaxial expansion) of each skeleton was transferred to the coating layer and induced rupture for coating of PMCA, PECA and PBCA, while PMECA and PEECA were stretched over the skeletons (not broken).

Based on the previous evaluation, re-Hex-SMP skeletons programed to α_{tem} = 50° and PBCA were justified for demonstrating the triggered dosing function of the system. The skeletons were loaded with a blue dye and coated with PBCA. The devices were stimulated in an aqueous solution by increasing the temperature. When the T_{switch} was reached, the devices expanded bi-axially, induced the coating failure and allowing the payload release, which could be visually monitored by a color change to a blue solution. This triggered dosing ability was evaluated for an on-demand release possibility by stimulating different devices at different time intervals up to 72 h. For all devices, the payload is released in a bolus mode (from ≈ 20% to ≈ 90%) after triggering. However, around 20% pre-stimulation release is observed, which is attributed to coating inhomogeneities or cracks that are generated during sample preparations and handling of devices.

Chapter 6 Conclusion and Outlook

In this thesis, the concept of a sequential coupling of functions in polymer-based devices has been explored in order to realize on-demand release systems. According to this concept, each function such as thermally induced active movement, or stress induced opening of reservoirs has its own input/output. A sequential coupling of individual functions to achieve the desired final release effect was shown to be possible by applying a number of guiding principles: (i) defined structure-function relationships on the molecular, morphological, and device level to control the individual functions, (ii) matching frame conditions to connect the output of one function and input of the next function (e.g., similar length scales), and (iii) the mechanical stability of the connection between the different components of the multi-material system (e.g., polymer scaffold and coating) mediated by device design.

Both concepts presented in this thesis were realized by considering specific design criteria, in particular (i) the dimensions of the overall device such as thickness or cutout-to-strut material ratio defining the volume of cavities for cargo embedding, (ii) the shape of the cutouts/cavities accounting either for stress concentration or for biaxial expansion ratios, (iii) the position of placement and relative arrangement of cavities to each other allowing sequential dosing and orchestrated self-sufficient actuation, respectively , and (iv) eventually the concept to temporarily enclose and release the cargo through, on the one hand, a material efficiently acting as a diffusion barrier and, on the other hand, showing tight interconnections and a mechanical mismatch for coating rupture.

A key element has been the specific design of cavities in the devices, which at the same time served as reservoirs and as cues that can direct the stimulus and convert it to a desired output (stress concentration or biaxial expansion). For instance, in the sequential release system, combining at least two distinct shapes of cavities exhibiting a SCF ratio of at least 1:2.2 enabled distinguishable values of stress concentration, which is the essential parameter for the sequential release effect in a single substrate. In the self-sufficient dosing device, the re-Hex design provided devices with a high magnitude of NPR and enabled, upon device stimulation, the desired expansion feature. At the scale of an individual re-Hex cell, the volume of SMP material in the switching position (the bended angles) represented ≈ 58% of

the total cell material, which accounted for strain and force of the device that are ≈ 100 fold and 8 fold higher than the strain and force at break of the coating layer, respectively.

In terms of device function, the coating design has been equally important as the geometrical features of the devices to not only conceptually but also practically allow a coupling of the mechanical deformation of the device and the coating rupture/cargo release. This can be assured by employing an intermediate PDA layer that provided not only a strong adhesion at the interface but also initiated the in situ polymerization of the coating material. Furthermore, the coating process was shown suitable not to impede the device functions (e.g. no undesired swelling of the device or inducing of shape-recovery).

For devices with cavities (reservoirs) of distinct shapes (e.g., circles, rhombuses), the potential of stress concentration within a polymeric substrate was explored (Chapter 4). Facilitating this concept, a mechanical input (stretching) led to a sequential opening of reservoirs for release, which could be useful in various applications. While studied here with dyes as model compounds, the release of dyes as optically visible “reporter” for structural changes within complex systems may serve as an indicator of potential constructional failure. When exchanged with active substances, such as catalysts or drugs, the release of these compounds may allow inducing desired effects at the time point of interest in closed systems. Stress concentration, the magnitude of which can be modulated by altering various experimental parameters and device properties, e.g. cavity shape, dimensions and mechanical properties of the substrate, appears to be an interesting approach also for further fundamental research.

In another example (chapter 5), the thermal-induced shape switching of an SMP matrix (via SME) was combined with a biaxial expansion (via a NPR design) of the multi-reservoirs device, which was coupled to a mechanical rupture of the sealing layer that gave the final effect as a pulse release of the payload. Both, the NPR behavior and SME, are not intrinsic materials properties, rather they rely e.g. on the geometrical device design, the polymer structure, and processing procedures, all being well tailored to respective needs. Accordingly, it is anticipated that based on desired applications, e.g., the temperature of operation or type of dimensional changes, various options of polymer materials and NPR designs may be considered in the future in order to make different extents of expansion or T_{switch} assessable.

Such a system may be applicable as a thermal-warning-indicator or thermal-self-dosing system in the biomedical field and the food industry, e.g. as an intelligent food packaging. Furthermore, the device might be applied as a closed reaction system, in which each reservoir is loaded with different substances, which can react together only upon device stimulation. In the biomedical field, multifunctional devices with capacity of transition to a larger application-relevant shape and controlled dosing (e.g. of contrast agents, drugs) could be an inspiration for translational research in the context of minimally invasive interventions, with the cardiovascular field being one of the most challenging sectors.

It is anticipated that the concept of coupling functions presented in this study is not limited to the explored devices. The functions investigated here might be coupled together in different orders and/or additional functions may be implemented for creating a new effect or expanding the applicability of these devices. For instance, while not studied here, connecting the thermal-induced shape switching (SMP) function and the stress concentration behavior may potentially enable a sequential dosing effect from a single substrate by external stimulation (non-contact stretching).

Overall, the concept of coupling functions addressed in this study can be employed as a platform for rational device designs. If a suitable transition between individual functions is realized, multi-functional polymeric systems can be created through sequential function coupling.

Chapter 7 Materials and methods

7.1 Materials

Negative photoresist (SU-8 2150) and developer (mr-Dev 600) were purchased from Micro resist technology GmbH, Germany. Silicon wafers (Prime CZ-Si wafer 3 inches, thickness = 381 ± 25 µm, 2-side polished, p-type Boron TTV < 10 µm, 1- 10 Ohm.cm) were purchased from MicroChemicals GmbH, Germany. PDMS (Sylgard 184) purchased from Dow Corning GmbH, Germany. Hexane (CHROMASOLV, for HPLC, > 97.0% (GC)), 2-isocyanatomethacrylate (IEMA), Isopropanol (ACS reagent) and blue dextran ($\bar{M}$w 2,000,000) were purchased from Sigma-Aldrich, Germany. Fluorescein sodium was from Scharlau Chemie S.A, Spain. Methylenblue (MB) and Dopamine hydrochloride were purchased from Alfa Aesar, Germany. Poly(ethylene glycol) (PEG) with $\bar{M}$w of 200 (PEG_{200}) and 1000 (PEG_{1000}) were purchased from Acros Organics, Germany. Dichloromethane (DCM; ACS reagent) was from Merck KGaA, Germany. Methyl cyanoacrylate (Loctite 493), ethyl cyanoacrylate (Sicomet 40) and methoxyethyl cyanoacrylate (Loctite 460) were from Henkel AG & Co, Germany. Samples of n-butyl cyanoacrylate (Cyberbond 7000) and ethoxyethyl cyanoacrylate (Cyberbond 5005) were kindly donated by Cyberbond Europe GmbH, Germany. Water used in all experiments was ultra-pure water.

7.2 Methods of system 1: Stress concentration in micro-structured materials for a sequential dosing function

7.2.1. Analysis of stress concentration by a computational model

The stress distribution and quantification were analyzed by the Finite Element Analysis (FEA) method via the Autodesk Inventor software (version 2018.2). The stress concentration was investigated in the linear elastic range. The input parameters in the FEA software for the substrate and the coating layer are summarized in Table 5.

For evaluation the SCF of cavities shapes and positioning in substrates, all substrates were designed with dimensions and geometry as shown in section 4.1.1, Figure 16. All cavities had a depth of 0.45 mm in the substrates. All substrates had a thickness of 0.5 mm (accordingly, each substrate had a cross section area of 5 mm x 0.5 mm = 2.5 mm^2). In each design, the surfaces of the substrate and cavities had a local elemental mesh size of 0.1 mm. On the x-

axis, each substrate was constrained from the left side and a uniaxial stretching force of 0.1 N was applied on the right side. The von Mises stress was determined in the substrate and at each cavity and applied in Equation 3 for quantification of the SCF.

The effect of cavity depth on the SCF was analyzed for the substrate of design 2 (shown in Figure 16). The depth of the substrate was kept constant at 5 mm and the depth of cavities was varied between 0.05 mm and 0.45 mm. In each case, the substrate was constrained from the left side and subjected to a uniaxial stretching force of 0.1 N from the right side. The von Mises stress was determined in the substrate and at each cavity and applied in Equation 3 for quantification of SCF.

The stress analyses at the coating-substrate interface were performed for substrates of design number 2 (shown in section 4.1.1, Figure 16) with a coating on the top. The substrates had a constant thickness of 0.5 mm and cavities had a constant depth of 0.45 mm. Coated substrates with a coating thickness of 1 µm, 2.5 µm, 5 µm, 7.5 µm, 10 µm, 12.5 µm and 15 µm were considered. In each case, the coating layers were treated as a thin body, which has a bonded contact type with the substrates. The applied mechanical properties are shown in the result section 4.1.1.4, Table 1. Each substrate was constrained from the left side and subjected to a uniaxial stretching force of 0.1 N from the right side. After stretching, in each case, the coating layer was isolated computationally from the substrate and the von Mises stress at the coating-substrate interface was determined in the coating layer and at the substrate surface at the site of cavities. The detected nominal stress in the coating layer values were applied in Equation 3 for quantification the SCF in the coating.

Table 5. Summary of the input parameters in the FEA software and the output of the simulation study.

Input parameters in the simulation software	General objective and settings		Study type	Static analysis	
			Modeling	linear elastic range	
			Design objective	Single point	
	Substrate (corresponds to Figure 17)	Assigned material of the substrates	Name	Silicone rubber	
			Mechanical properties	Yield Strength	10.34 MPa
				Tensile Strength	6.5 MPa
				Young's Modulus	3 MPa
				Poisson's Ratio	0.49
				Shear Modulus	1.007 MPa
		Mesh settings	Average element size (fraction of model diameter)	0.1 mm	
			Minimum element size (fraction of average size)	0.2 mm	
			Local element size of all surfaces of substrates and cavities	0.1 mm	
			Grading factor	1.5	
			Maximum turn angle	60 degree	
			Create curved mesh elements	Yes	
		Operating conditions	Constraint type	Fixed Constraint at left side of the substrate	
			Load type	Force	
			Magnitude	0.1 N from the right side of the substrate	
	Coating layer (when applied on the substrate, correspond to Figure 20)	Assigned material of the coating	Name	Poly(***n***-butyl cyanoacrylate)	
			Mechanical properties	Yield Strength	0.79 MPa
				Tensile Strength	0.9 MPa
				Young's Modulus	8000 MPa
				Poisson's Ratio	0.4
				Shear Modulus	0.125 MPa
		Coating type	Thin layer (shell)		
		Mesh setting	Average element size in shell is 0.05 mm		
		Operation condition	Contact type of the coating layer (shell) on the substrate is bonded		
Output of the study		Stress distribution visualization and quantification	Nominal of von Mises stress in the substrate was quantified		
			Maximum of von Mises stress at site of cavities was quantified		
			Nominal of von Mises stress in the coating layer at the coating-substrate interface was quantified		
			Maximum of von Mises stress in the coating layer over the site of cavities at the coating-substrate interface was quantified		
Calculated values			From the output of the study, SCF of different cavities and at coating-substrate interface was calculated by equation 3		

7.2.2. Fabrication of micro-geometrical patterns and structured substrates

On silicon wafers, patterns with microscale features were created as master molds and then replicated in polydimethylsiloxane (PDMS). This process involved the design of photomasks with patterns corresponding to each substrate's design (design 1, 2 and 3 shown in Figure 16) using Autodesk (AutoCAD) software, which were than externally printed on polyester films (photomasks) at high resolution (128K dpi) by JD Photo Data company (United Kingdom). Silicon wafers were spin-coated with 3 ml of SU-8 2150 photoresist at 500 rpm for 10 s with acceleration of 100 rpm/s followed by 1000 rpm for 30 s with acceleration of 300 rpm/s.

Thereafter, the photoresist-coated silicon wafers were heated on a programmable hotplate (HP 30 A, BlackHole Lab, France) at 65 °C for 15 min, followed by 100 °C (ramping rate ≈ 1.5 °C/min) for 4 h. The photomask of the desired substrate design was placed on the silicon wafer and exposed for 45 s to a UV-light irradiation (mercury arc lamp 365 nm, intensity 114 mW/cm^2, Solar simulator system, Abet technology) with using a UV filter (cut-on 365 ± 7 nm, Laser Components GmbH, Germany). After exposure, the silicon wafers were heated at 65 °C for 10 min then at 100 °C for 50 min. Thereafter, the structures were developed by immersing the silicon wafers in the developer (mr-Dev 600) for 15 min under shaking 50 rpm/min. Then, the silicon wafers were rinsed with isopropanol and dried with air stream.

PDMS base and curing agent (Sylgard 184) were mixed together with a weight ratio of 10:1, respectively, poured onto the patterned silicon wafer and degassed under vacuum for 10 min. The mixture was cured in an oven at 100 °C for 35 min and thereafter carefully peeled from the pattern, which produced a PDMS template imprinted with geometrical cavities. The dimensions of the substrates were characterized microscopically, while the depth of the cavities in the substrates was determined by SEM (Phenom G2 pro, Phenom-World B.V, Germany).

7.2.3. Formation of the intermediate layer (polydopamine)

The intermediate layer was prepared by treating PDMS substrates with dopamine to form a polydopamine (PDA). PDMS substrates were placed in a plastic petri dish (94 x 16 mm, Greiner Bio-One GmbH, Germany). A solution of dopamine hydrochloride (2 mg/ml in a TRIS buffer, 10 mM, pH = 8.5) was added in the dish (2 ml solution for each substrate), which was closed with the lid and was shaken at 50 rpm (shaker GFL 3014, GFL Gesellschaft für Labortechnik GmbH, Germany) for 24 h. Thereafter, PDMS substrates were rinsed with water and dried under an air stream.

7.2.4. Loading of micro-scaled cavities

After the PDMS substrate were treated with PDA, the cavities were loaded under an inverse microscope (Leica DMI6000 B, Germany) by a micro-injection system, which consisted of a micro-syringe pump controller (Micro 4) and a micro-injector (ultra micro pump 3 - UMP3) (World Precision Instruments GmbH, Germany). The micro-injector was connected with a

micromanipulator (SM 3.25, Märzhäuser Wetzlar GmbH, Germany). A micro-syringe without a needle (Hamilton SYR 100 µl/1710RN) was connected with a capillary glass (1 mm outer diameter) with an orifice of 30 µm (grinded by a sand paper), through which the material was dosed. The capillary glass was inserted in each cavity, which was injected with ≈ 25 nl compound (injection rate: 5 nl/s). Circular cavities were injected with a mixture of fluorescein sodium (40 mg/ml in water) with PEG_{200} in a volume ratio of 1:9, respectively. Rhombus shaped cavities were loaded with a mixture of methylene blue (30 mg/ml in water) with PEG_{200} in a volume ratio of 1:9, respectively.

7.2.5. Coating of micro-scaled cavities and coating characterization

After the cavities were loaded, 5 µl solution of n-butyl cyanoacrylate (1% v/v in hexane) was added (by a micropipette) 2 times (5 min interval between each cycle) over the cavities at room temperature (≈ 25 °C) and then the substrate was placed under a fume hood for 1 h for solvent evaporation.

For characterization of the coating, the coated sample was frozen by immersion in liquid nitrogen followed by a cut at the cavities sites by a razor blade. The cut substrates were immersed in a dish containing 50 ml of water to remove the payload in the cavities. Isolated samples were placed under the fume hood overnight for water evaporation. Thereafter, samples were treated in vacuum (5 x 10^{-2} mbar) for 24 h and sputter coated with gold (thickness of 5 nm, 5 x 10^{-2} mbar, 10 - 20 mA, 90 s; SC7640, Quorum Technologies Ltd, UK) and examined by scanning electron microscopy (SEM; Phenom G2 pro, Phenom-World B.V, Germany) for determining the coating thickness and coating morphology. Image analysis was performed by ImageJ program (version 1.49, National Institutes of Health, USA).

7.2.6. Customization and calibration of a miniaturized tensile tester

A customized miniaturized tensile tester was assembled manually. Two clamps (size = 13 mm, Mauly paper clamps, Germany) were fixed by a glue (Wiko 05 transparent epoxy glue, Gluetech, Germany) on the arms of tubing clips of Hofmann pattern (40 mm, TH.Geyer, Germany). One clamp was fixed on the middle of the distal stable arm and the other clamp was fixed on the middle of the movable arm (Figure 54 A). These clamps are used as jaws to hold the sample. The tubing clips of Hofmann pattern have a screw in the middle (Figure 54

A). By rotating the screw (clockwise or counterclockwise), the movable arm moves forward and backward, which increases or decreases the distance between the two clamps.

Calibration of the customized tensile tester

For determining the precision of the device, the screw was rotated and the distance between the arms was measured by a vernier caliper (limit-tools Company, Germany) before and after rotation. Each full rotation of the screw gave an average strain (increase distance between the arms) of 5.4 ± 0.2% (determined from n = 5 individual rotations).

In order to control the rate of the stretching (i.e. the rate of rotating of the screw), the stable arm behind the screw was marked with a tick and the surface of the screw (has a diameter ≈ 1.5 cm) was marked with a circle with 12 ticks similar to a clock (Figure 54 B). The screw was rotated continuously (manually) in an approximate rate of one tick per second (rotating the screw until the next circle-tick on the screw matches the tick on the stable arm behind the screw during one second). This corresponds to one full rotation of the screw per 12 s, i.e. a strain of 5.4%/12s, which calculated as a deformation rate of + 0.45 ± 0.01%/s (n = 5, uncertainty is a propagation of SD according to Equation 43). This value of the strain rate (0.45%/s) is applied later in Equation 38 for calculating the percent error of the customized tensile tester.

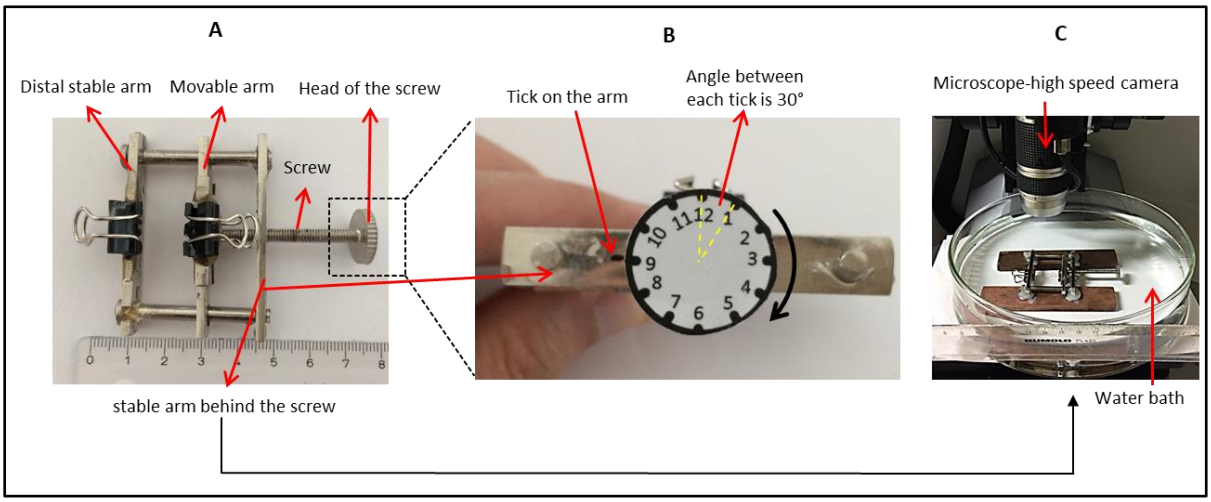

Figure 54. A) An overview of the custom-build tensile device. B) A magnified view of the head of the screw showing the circle with 12 ticks and the tick on the stable arm behind the screw used to standardize the manual deformation procedure. C) Image of the tensile device placed in a water bath under the microscope as an experimental setup to microscopically monitor the stretching-induced sequential dosing from the substrate.

7.2.7. Characterization of the strain-induced sequential dosing function

After loading the cavities, the coated samples (see 7.2.5) were introduced in the customized tensile tester and placed upside-down under a high speed camera-microscope (Keyence VW-9000 with VW-300 C, Germany) in a water bath (1 L) at ambient temperature (≈ 25 °C) (Figure 54 C). The substrate was stretched continuously by rotating the screw at a speed of approximately 1 tick per second (as describes previously) and the experiment was recorded as a video. From the recorded video, the average strain rate (change in strain per time) was calculated according to Equation 37, where $\Delta\varepsilon$ and Δt are change in strain and change in time, respectively. The experimental average strain rate was ≈ 0.5%/s ± 0.2%/s (n = 3 individual stretching experiments), which is applied as the measured value in Equation 38 for calculating the percent error of the device. Accordingly, the error of the customized tensile device was determined to be ≈ 11%.

$$\text{average strain rate} = \frac{\Delta\varepsilon}{\Delta t} \qquad \text{Equation 37}$$

$$\%\ \text{error} = \left|\frac{measured\ value - accepted\ value}{accepted\ value}\right| x100 \qquad \text{Equation 38}$$

The recorded video was converted to snapshots images (1 image per second). The images were used in ImageJ software for determining the value of the applied strain and the accompanied lateral compression from y-axis (due to passion ratio) by measuring the dimensions of the sample (length and width) before and after stretching (initial image and image during stretching). From the images, the dosing initiation (dye release) from the rhombus cavities and the circular cavities was detected and correlated to the value of the applied strain.

Quantification of compound release based on the principle of grayscale

For release quantification, the images collected from cavities during deformation experiments were converted to gray images (8 bit, by imageJ software) using the grayscale to estimate the release kinetics as shown in Figure 55 A. By this approach, a loaded reservoir appeared as a dark, almost black color according to the grayscale (Figure 55 B) while an empty reservoir (as control cavities) appeared as a brighter color (Figure 55 C). During the tensile

strain-release experiment, the percentage of the release was determined by measuring the mean gray values of the cavities and applying them in Equation 39.

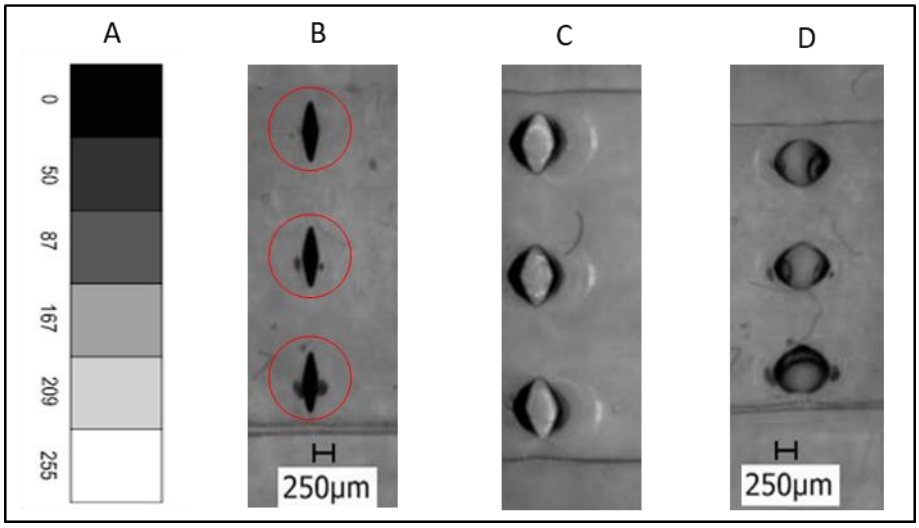

Figure 55. An image of the universal grayscale. Black = 0 gray value. White = 255 gray value. B) Initial gray value in cavities (remarked with red circles), i.e. loaded cavities before stretching (0% release), e.g. gray value = 50. C) A control gray value of cavities (unloaded cavities = 100% release), e.g. = 209 gray value. D) A Gray value of cavities during tensile-release experiment, e.g. at 3% strain cavities has a gray value = 167 averaged over the area of the cavity.

$$\%\, release = \frac{Mean\ gray\ of\ reservoirs\ during\ tensile\ strain\ -\ initial\ mean\ gray}{Control\ mean\ gray\ -\ initial\ mean\ gray} x\ 100 \qquad \text{Equation 39}$$

7.2.8. Preparation of PDA-poly(ethyl cyanoacrylate) sample for analysis by X-ray photoelectron spectroscopy

PDA nanoparticles were synthesized by self-polymerization of dopamine hydrochloride solution (2 mg/ml in TRIS buffer, 10 mM, pH=8.5) in a falcon tube (45 ml) under shaking (50 rpm/min) for 24 h. The obtained suspension was centrifuged (8500 rpm/15 min) (Heraeus Biofuge Stratos, Germany), the supernatant was removed, the particles were washed with water (30 ml) and centrifuged again. This step was repeated 3 times to remove any trace of non-polymerized dopamine. Finally, the particles were frozen in liquid nitrogen and then subjected to the lyophilization using the freeze-dryer Alpha 1-2LD plus (Christ, Germany) for 24 h.

On a scarifying layer of PEG_{1000}, 150 µl of PDA suspension (2 mg/ml in hexane) was spread over the PEG layer. The sample was placed in vacuum for 6 h to evaporate the solvent, which formed a thin layer of PDA nanoparticles. Thereafter, 50 µl of neat ECA monomer was spread

over the PDA layer then the sample was placed under the fume hood for 24 h. The PEG layer was dissolved in water to detach the PDA-PECA film from the surface for XPS analysis, which was conducted at the PDA side of the film. The film was rinsed with water, dried under the fume hood, vacuumed for 24 h and then analyzed by XPS from the PDA side as described below.

X-ray photoelectron spectroscopy

XPS measurement (axis ultra, Kratos Analytical LTD, United Kingdom) was performed with an aluminum-monochromator-x ray source with an energy of 1486.6 eV at a resolution of 160 eV pass energy (survey spectra) or 10 eV pass energy (regional spectra) with 3 scans at 250-330 ms (step 0.5 eV or 0.1 eV, respectively). Survey spectra as well as high resolution regional spectra of relevant elements (carbon, oxygen and nitrogen) were recorded. The curve fitting was performed assuming a Gaussian peak shape. The measurements performed at two different location of each sample. The spot size was 300 µm x 700 µm.

7.3 Methods of system 2: Self-sufficient thermo-responsive dosing device

7.3.1. Fabrication of re-Hex patterns and molds

Photomasks with patterns corresponding to the re-Hex structures (designs with 5 cells, 8 vertical cells, 8 horizontal cells) were designed by Autodesk (AutoCAD) software and were externally printed at high resolution (128K dpi) by JD Photo Data company (United Kingdom).

Skeleton of re-Hex design number 3 (in Table 2) was fabricated by spin coating 3 ml of SU-8 2150 photoresist on a silicon wafer (Prime CZ-Si wafer 3 inches) at 500 rpm for 10 s with acceleration of 100 rpm/s followed by 1000 rpm for 30 s with acceleration of 300 rpm/s. Thereafter, the photoresist-coated silicon wafers were heated on a programmable hotplate (HP 30 A, BlackHole Lab, France) at 65 °C for 15 min, followed by 100 °C (ramping rate ≈ 1.5 °C/min) for 4 h. The photomask of re-Hex design number 3 (in Table 2) was placed on the silicon wafer and exposed for 45 s to a UV-light irradiation (mercury arc lamp 365 nm, intensity 114 mW/cm^2, Solar simulator system, Abet technology) with using a UV filter (cut-on 365 ± 7 nm, Laser Components GmbH, Germany). After exposure, the silicon wafers were heated at 65 °C for 10 min then at 100 °C (ramping rate ≈ 1.5 °C/min) for 50 min. Thereafter, the structures were developed by immersing the silicon wafers in the developer (mr-Dev 600)

for 15 min under shaking 50 rpm/min. Then, the silicon wafers were rinsed with isopropanol and dried with air stream.

Skeleton of re-Hex design number 12 (in Table 2) was fabricated in a glass petri dish (soda-lime glass, 60 x 15 mm, Duran group, Germany). An amount of SU-8 2150 photoresist, which is equal to 3 mm thickness, was casted in the petri dish. The dish was heated to 100 °C for 24 h (ramping rate ≈ 1.5 °C/min, hotplate HP 30 A, BlackHole Lab, France,) in the dark. The photomask of the re-Hex design was placed on the photoresist and the UV filter was placed on the top as a cap of the dish. Thereafter, the sample was exposed to an intermittent UV-light radiation. The sample was irradiated 6 times, each is 45 s with 5 min interval between each irradiation. After exposure, the petri dish was heated at 95 °C for 30 min. The structure was exposed to the developer solution for 3 min (repeated 10 times) to completely dissolve the uncross-linked photoresist. After developing, the structure was rinsed with isopropanol and heated at 95 °C for 1 h in order to harden the photoresist.

PDMS base and curing agent (Sylgard 184) were mixed together with a weight ratio of 10:1, respectively, poured onto the patterned glass petri dishes and silicon wafer and degassed under vacuum for 10 min. The mixture was cured in an oven at 65 °C for 2 h and thereafter carefully peeled from the pattern, which produced a PDMS mold imprinted with the re-Hex design.

7.3.2. Producing of re-Hex-SMP networks

Oligo(ε-caprolactone)-diols (CAPA 2803, Perstorp, UK) with a number average molecular weight ($\overline{M}_n$) of 8 KDa was functionalized with IEMA (degree of IEMA functionalization 97% , typical error of the NMR is 10%) to obtain linear oCL-diIEMA precursors with methacrylate endgroups as reported elsewhere [163]. The precursors was filled in a PDMS template of the intended re-Hex designs (e.g. template of 5 or 8 cells re-hex designs prepared according to 7.3.1) in melt (80 °C) and under vacuum to remove air bubbles, which may form holes in walls of re-Hex-SMP skeletons. The excess polymer at the surface of PDMS was scraped by a glass cover slide. The PDMS template was placed in a chamber under a nitrogen stream. The chamber was closed with a quartz glass and placed under the UV-light (Omnicure S-2000, λ = 250 – 400 nm) with 5 cm distance between the PDMS and the source of the UV-light. The

sample was irradiated for 20 min at 80 °C for crosslinking. To collect the samples from the PDMS mold in an intact manner, an amount of PCL (45 kDa) was molted (80 °C) on the top of the PDMS mold and then kept at room temperature for about 1 h to solidify. The PCL film was gently peeled from the PDMS surface (with the cross-linked samples attached to the PCL film) and placed into 50 ml DCM under gentle shaking (50 rpm/min) for 30 min in order to dissolve the PCL film and collect the re-Hex-SMP skeletons, which were placed under the fume hood for drying. The dimensions of the obtained re-Hex-SMP skeletons (length, width, depth, wall thickness and angle degree) were determined under the microscope (Keyence VW-9000, Germany).

7.3.3. Characterization of network properties

From the walls of re-Hex-SMP skeletons (obtained from 7.3.2), pieces were cut (each piece has a length ≈ 3 mm, a width ≈ 3 mm and a thickness ≈ 0.3 mm) and used as film samples for the following characterization of network properties.

The conversion of methacrylate end-groups after crosslinking was analyzed via examining a film sample (n = 1) by FT-IR spectrometry (Nicolet 6700, Thermo Scientific, Germany) equipped with a diamond-ATR-unit (DuraSamplIR, Resultec, Germany). Under permanent purging with compressed dry air, the spectra were recorded with an average of 50 scans (resolution 2 cm^{-1}).

Thermal characterization was performed by differential scanning calorimetry (DSC; 204 F1 Phoenix, Netzsch, Germany). A film sample (≈ 5 mg) (n = 1) was measured in the temperature range of -100 to +150 °C with a heating and cooling rate of 10 $K \cdot min^{-1}$ for determining the melting temperature. The thermal properties of the polymer were evaluated from the second heating run. The T_m was determined as the peak maximum of the melting transition.

For determining the degree of swilling (Q) and gel content (G), re-Hex-SMP skeletons were prepared as in 7.3.2 but the skeletons were isolated from PDMS molds with a tweezer (without the approach of PCL film to avoid extraction before determining the Q and G). From the isolated skeletons, film samples (n = 3) were cut from the walls (each film has dimensions of 3 x 3 x 0.3 mm). Each film was incubated in 2 ml DCM for 24 h. Extracted samples were dried at 40 °C under vacuum for 24 h. The mass of each sample was determined in the initial

dry state, in the swollen state and for dried samples after extraction. The obtained masses were applied in Equation 12 and Equation 13 for determining Q and G.

7.3.4. Programming of re-Hex-SMP skeleton by method of PDMS templates

A PDMS template, which is imprinted with a structure of the desired programmed shape (re-Hex with the desired a_{tem}), was fabricated by the soft photolithography technique as described in 7.3.1. The re-Hex-SMP skeleton was introduced in the PDMS template at room temperature (≈ 25 °C) based on its ability for cold deformation. The template was heated in an oven at 80 °C ($T > T_m$) to melt the crystalline switching domains and then cooled down to the room temperature (≈ 25 °C, $T < T_m$) to fix the temporary shape. Subsequently, collecting the structure from the PDMS produced a programmed re-Hex-SMP skeleton.

7.3.5. Characterization of SME properties

As the re-Hex-SMP skeletons were programmed by a controlled wall bending and changing the angle degree, the properties of SME were quantified according to the bending test. Re-Hex-SMP skeletons (n = 6) of a_{per} = 90° were programed to a_{tem} = 50°. The internal angle and the complementary angle of each cell (illustrated previously in Figure 9) was measured in the permanent shape, programed shape and after shape-recovery under the microscope. The measured values were applied in Equation 16 and Equation 17 for determining $R_{f,bending}$ and $R_{r,bending}$.

For determining the switching temperature (T_{switch}), programmed skeletons (n = 3) of α_{tem} ≈ 50° (programed by PDMS mold at 80 °C as described in 7.3.4) were used. Each skeleton was placed along with a thermometer with a thermocouple (type K, accuracy ± 1 °C) in water on a hotplate (IKA, RCT basic, IKA® Werke GmbH & Co.KG, Germany. The experiment was recorded as a video. The temperature was elevated up to 65 °C (ramping rate 6.5 K/min) and the shape switching was monitored and correlated to the applied temperature.

7.3.6. Characterization the shape-recovery force of re-Hex-SMP devices

On a hotplate (IKA, RCT basic, IKA® Werke GmbH & Co.KG, Germany), a programmed (compressed) re-Hex-SMP skeleton was placed horizontally (shown in Figure 39). The skeleton

was blocked with a metal barrier from the back side and was in tangent with a load cell (miniature button load cell 410, load cell shop, Richmond Industries Ltd, UK) from the front side. The temperature was elevated (ramping rate 6.5 K/min) for inducing the shape-recovery. Based on the geometry of the setup, the expansion of the skeleton was directed toward the load cell and the measured force was recorded. The shape-recovery force was determined from the jump point on the curve to the peak maximum of the recorded force, which was normalized by subtracting the noise (value before the jump point) from the curve.

7.3.7. Treatment of re-Hex-SMP skeletons with PDA and analysis

The intermediate layer was formed by treating re-Hex-SMP skeletons with PDA. Skeletons were immersed in a solution of dopamine hydrochloride (2 mg/ml in TRIS buffer, 10 mM, pH = 8.5) (2 ml solution for each skeleton) under shaking 150 rpm (IKA KS 260 Basic, IKA® Werke GmbH & Co.KG, Germany) for 24 h at room temperature (≈ 25° C). Thereafter, the re-hex-SMP skeletons were rinsed with water and dried under an air stream.

For FT-IR characterization, a piece from the wall of the PDA-coated skeleton was cut, vacuumed for 24 h to remove water, which may interfere with the data interpretation. The sample (n = 1) was measured with FT-IR spectrometry (Nicolet 6700, Thermo Scientific, Germany) equipped with a diamond-ATR-unit (DuraSamplIR, Resultec, Germany). Under permanent purging with compressed dry air, the spectra were recorded with an average of 50 scans (resolution 2 cm^{-1}).

From the PDA-coated skeleton, a piece from a wall was cut for determining the thickness of PDA. The piece was examined by SEM (Phenom G2 pro, Phenom-World B.V, Germany) for visualizing the PDA layer. For determining the thickness of PDA, cryo-ultramicrotomy with a diamond knife was used to prepare samples by a cross-sectional cut at room temperature (≈ 25 °C). The sliced sample was placed on a copper grid 300 mesh and examined with a transmission electron microscopy (TEM; Talos F200X, Thermo Fisher Scientific, United States) at high tension 200KV. One sample was used for 11 individual thickness measurements in different positions.

7.3.8. Formation of polycyanoacrylate (polyCA) coating over programmed re-Hex-SMP skeletons

Re-Hex-SMP skeletons of 8 vertical cells were used. All skeletons were programmed from a_{per} = 90° to an a_{tem} = 50 ° by the PDMS mold as described in 7.3.4 and were then treated with PDA. Each skeleton was placed on a glass slide and each cell of the device was filled by a micropipette with ≈ 10.5 µl of molten PEG_{1000} (at 40 °C), which solidified in the cell after cooling down to the ambient temperature (≈ 25 °C). On top of each cell, 1 µl of CA-monomer solution (1% v/v in hexane) was added. This step was repeated either 2, 4, 6, 8 or 16 times with a 5 min interval between each cycle to evaporate the solvent. Then samples were placed under the fume hood for 24 h. Afterwards, each sample was carefully immersed in 10 ml water in a glass petri dish (soda-lime glass, 60 x 15 mm, Duran group, Germany) under shaking (50 rpm, IKA KS 260 Basic, IKA® Werke GmbH & Co.KG, germany) for 1 h to dissolve the PEG_{1000}. Samples were collected and dried under the fume hood.

7.3.9. Characterization of polyCA coating thickness and coating breakability

Coated re-Hex-SMP skeleton were prepared as in 7.3.8. Thereafter, samples were cut at the cross-section, vacuumed for 24 h and sputter coated with gold (thickness of 5 nm; 5 x 10^{-2} mbar, 10-20 mA, 90 s; sputter coater SC7640, Quorum Technologies Ltd, UK). The thicknesses of the polyCA coatings were examined by SEM (Phenom G2 pro, Phenom-World B.V, Germany).

For the analysis of coating breakability, the same sample preparation procedure as in 7.3.8 was followed. When the skeletons were immersed in water, the dishes were incubated in an oven (Heraeus T6, Thermo Fischer Scientific, Germany) at 60 °C, where the shape-recovery was induced and the coating breaking was observed.

For characterization of coating breakage mechanism, PBCA (16 coating cycles) coated re-Hex-SMP skeletons were prepared as in 7.3.8. When skeletons were immersed in a petri dish (soda-lime glass, 60 x 15 mm, Duran group, Germany) containing 10 ml of Milli-Q water, the dish was placed on a hotplate (IKA, RCT basic, IKA® Werke GmbH & Co.KG, Germany) under a high speed camera-microscope (Keyence VW-9000 with VW-300 C, Germany). The

temperature was elevated up to 65 °C (ramping rate 6.5 K/min) and the experiments were monitored and recorded as videos. From the videos, images were extracted (one image/second) and analyzed for crack initiation/propagation and rupture of the coating layer.

7.3.10. Characterization of mechanical properties of polyCA membranes by in-situ micro-indentation

Coating formation over re-Hex-SMP of permanent shape

The micro-indentation experiments were performed on free-standing polyCA membranes, which were formed and examined on a re-Hex-SMP skeleton of permanent shapes (square cell, each cell = 9 mm^2). Each cell was filled by a micropipette with 22 µl of PEG_{1000} at molten state (≈ 42 °C), which is solidified at room temperature (≈ 25 °C). The polyCA membranes were formed by adding per cell 1.5 µl of a CA-monomer (1% v/v in hexane) for 16 coating cycles. Thereafter, each skeleton was placed in 10 ml Milli-Q water in a petri dish (soda-lime glass, 60 x 15 mm, diameter, Duran group, Germany) under shaking (50 rpm, IKA KS 260 Basic, IKA® Werke GmbH & Co.KG, Germany) for dissolving the PEG.

Instrumental setup

The setup of the micro-indentation instrument consisted of an inverted microscope (Leica DMI6000B, Leica Microsystems, Gemany), a micro-force sensor probe (FT-S10000-TP with a spherical glass tip of 25 µm, FemtoTools, Switzerland), which is linked to a micromanipulator with a stepper motor controller (micromanipulator SM 3.25 with Tango 3 desktop controller, Märzhäuser Wetzlar GmbH, Germany). The re-Hex-SMP skeleton coated with polyCA membrane was placed on the microscope under the force sensor tip, which was centered over the polyCA membrane. The contact point between the membrane and the tip was determined from the jump in the curve of the recorded force. For the load-unload curve, the indentation velocity was 5 µm/s, while the velocity was 20 µm/s for the experiments with indentation up to break.

7.3.11. Preparation of polyCA samples for DSC measurement

In order to determine the thermal properties of polyCA as a coating material studied in chapter 5, the analysis should be conducted at conditions linked to the device coating step. Isolating polyCA films formed on re-Hex SMP skeletons of the permanent shape (described in

7.3.10) gave ≈ 1 mg of polyCA material, which is insufficient for performing DSC measurement (at least ≈ 5 mg sample is required). Therefore, a sufficient amount of different polyCA films for measuring thermal properties were prepared in an approach that mimics (in condition and ratio) the formation of the coating over the re-Hex-SMP skeleton in the permanent shape (1.5 µl CA-monomer for each 9 mm^2, described in 7.3.10).

In a petri dish (diameter of 3.5 cm, surface area ≈ 962 mm^2), 2 ml of molten PEG_{1000} (45 °C) was added and solidified at room temperature (≈ 25 °C). From a desired CA monomer solution (1% v/v in hexane), 160 µl were spread 16 times (5 min interval between each) over the solidified PEG_{1000}. The dish was kept under the fume hood for 24 h. Thereafter, the PEG_{1000} was dissolved by immersing the dish in water bath and the floated polyCA film was collected. The collected film was placed in an eppendorf tube, washed with water and centrifuged (8500 rpm, Heraeus Biofuge Stratos, Germany). This step was repeated 3 times to remove traces of remaining PEG. Then the film was freeze dried (Alpha 1-2LD plus, Christ, Germany) and examined by DSC (204 F1 Phoenix, Netzsch, Germany). For each type of polyCA film, one sample (n = 1) was measured by DSC. Each sample (≈ 5 mg) was measured in the temperature range of -100 to +150 °C for determining the glass transition temperature. Heating and cooling rates were 10 $K \cdot min^{-1}$ for sample of PECA and PBCA and 20 $K \cdot min^{-1}$ for PMECA and PEECA samples (as they were not detectable at 10 $K \cdot min^{-1}$). The T_g was determined at the inflection point on the thermograms from the second heating run.

7.3.12. Loading re-Hex-SMP devices with a compound and coating with polyCA for demonstration experiments of on-demand dosing function

A mixture of methylene blue (30 mg/ml in water) with a molten PEG_{1000} (40 °C) was prepared at a volume ratio of 3:7. This solution has a high color intensity that enables visualization the onset of dosing upon stimulation. This solution is liquid at room temperature, which allowed loading without elevated temperature. After re-Hex-SMP (either single-cell or multi-cell) skeletons were programmed from a_{per} = 90° to a_{tem} = 50 ° and treated with PDA, each device was held at its grip. Each cell of the device was loaded manually (by a micropipette) with 10 µl of the loading solution. Devices were placed for 24 h under the fume hood for water evaporation, which produced a blue solidified PEG matrix in each cell. Each cell was filled again with 3 µl of the loading solution; then water was evaporated again, which produced

fully loaded reservoirs. Each device was coated from the top side with PBCA (1% v/v BCA in hexane) for 16 coating cycles as described in 7.3.8. Then the device was turned upside-down and coated again with 16 coating cycles. The devices were subsequently held at the grip and immersed in an aqueous medium under stirring. The temperature was increased to 55 °C (heating rate 6.5 K/min, IKA, RCT basic, IKA® Werke GmbH & Co.KG, Germany). The experiments were recorded as videos, for which the snapshots were presented in the result section.

7.3.13. Timing of on-demand dosing of re-Hex-SMP switchable devices; Release experiments

A mixture of dextran (40 mg/ml in water) and molten PEG_{1000} (40 °C) at a volume ratio of 3:7 was used as a model solution for loading. Each re-Hex-SMP skeleton of 8 vertical multi-cells was programmed from a_{per} = 90° to a_{tem} = 50 ° (as described in 7.3.4), treated with PDA (as described in 7.3.7) loaded with the mixture solution and coated with PBCA (as described in 7.3.12). Afterwards, each device was placed in 5 ml PBS buffer (10 mM, pH=7.4) solution in a well of 12 wells plates. The plate was incubated at 37.5 °C (Certomat IS, Sartorius stedim biotech, Germany) under shaking at 50 rpm. To apply a temperature stimulus, the 12 wells plate was transferred into an oven at 55 °C (Heraeus T6, Thermo Fischer Scientific, Germany) for 30 min, then were returned to the incubator (37.5 °C) for 30 min and then was sampled. Medium sampling (5 ml) was performed at specific time intervals and replaced with a fresh medium. From the samples, 100 µl aliquot was transferred into a 96 wells plate for measuring the absorption by a plate reader (Infinite F50, Tecan Group Ltd, Germany) at a wavelength of 620 nm. The release was then quantified based on the standard calibration curve.

7.4 Statistic and error consideration

Reported values are given as the mean value ± standard deviation (uncertainty), if not otherwise stated. The mean ($\overline{x}$) value is defined as the numerical average of all measured values within a data set and can be calculated according to Equation 40, where *n* is the number of data points and a_i denotes the different measured values. The standard deviation (*SD*) describes the spreading of the individual values a_i around the mean in a data set, and can be determined according to Equation 41.

$$\overline{x} = \frac{1}{n}\sum_{i=1}^{n} a_i$$ Equation 40

$$SD = \sqrt{\frac{\sum_{i=1}^{n}(a_i - \overline{x})^2}{n-1}}$$ Equation 41

When stated, the propagation of SD (propagation of uncertainty) is the effect of variables' uncertainties of a calculated value (V). When V is calculated by dividing variables A and B with standard deviations SD_A and SD_B , respectively, as in Equation 42:

$$V = \frac{A}{B}$$ Equation 42

then, the standard deviation of V (SD_V) is calculated according to Equation 43. If B is a constant, then SD_B = 0.

$$SD_V = V\sqrt{\left(\frac{SD_A}{A}\right)^2 + \left(\frac{SD_B}{B}\right)^2 - 2\,\frac{SD_A\ x\ SD_B}{AB}}$$ Equation 43

References

1. Y.A.N. Geng, et al., *Shape effects of filaments versus spherical particles in flow and drug delivery.* Nature Nanotechnology, 2007. 2(4): p. 249-255.

2. K.A. Kilian, et al., *Geometric cues for directing the differentiation of mesenchymal stem cells.* Proceedings of the National Academy of Sciences, USA, 2010. 107(11): p. 4872-4877.

3. X. Xu, et al., *Microwell Geometry Modulates Interleukin-6 Secretion in Human Mesenchymal Stem Cells.* MRS Advances, 2017. 2(47): p. 2561-2570.

4. Z. Li, et al., *Integrin β1 activation by micro-scale curvature promotes pro-angiogenic secretion of human mesenchymal stem cells.* Journal of Materials Chemistry B, 2017. 5(35): p. 7415-7425.

5. B. Bhushan, Y.C. Jung, and K. Koch, *Micro-, nano- and hierarchical structures for superhydrophobicity, self-cleaning and low adhesion.* Philosophical Transactions of the Royal Society of London, Series A: Mathematical and Physical Sciences, 2009. 367(1894): p. 1631-1672.

6. Y. Jiang, et al., *Temperature-induced evolution of microstructures on poly[ethylene-co-(vinyl acetate)] substrates switches their underwater wettability.* Materials & Design, 2019. 163: p. 107530.

7. M.P. Murphy, S. Kim, and M. Sitti, *Enhanced Adhesion by Gecko-Inspired Hierarchical Fibrillar Adhesives.* ACS Applied Materials & Interfaces, 2009. 1(4): p. 849-855.

8. A. del Campo, C. Greiner, and E. Arzt, *Contact shape controls adhesion of bioinspired fibrillar surfaces.* Langmuir, 2007. 23(20): p. 10235-43.

9. G. Ahuja and K. Pathak, *Porous carriers for controlled/modulated drug delivery.* Indian Journal of Pharmaceutical Sciences, 2009. 71(6): p. 599.

10.J.A. Champion, Y.K. Katare, and S. Mitragotri, *Making polymeric micro-and nanoparticles of complex shapes.* Proceedings of the National Academy of Sciences, USA, 2007. 104(29): p. 11901-11904.

11.X. Younan and W.G. M., *Soft Lithography.* Angewandte Chemie International Edition, 1998. 37(5): p. 550-575.

12.D. Qin, Y. Xia, and G.M. Whitesides, *Soft lithography for micro- and nanoscale patterning.* Nature Protocols, 2010. 5: p. 491.

13.K.J. McHugh, et al., *Fabrication of fillable microparticles and other complex 3D microstructures.* Science, 2017. 357(6356): p. 1138-1142.

14.D. Dendukuri, et al., *Continuous-flow lithography for high-throughput microparticle synthesis.* Nature Materials, 2006. 5(5): p. 365-9.

15.D. Dendukuri, et al., *Stop-flow lithography in a microfluidic device.* Lab on a Chip, 2007. 7(7): p. 818-828.

16.D. Dendukuri, et al., *Controlled Synthesis of Nonspherical Microparticles Using Microfluidics.* Langmuir, 2005. 21(6): p. 2113-2116.

17.H.N. Chia and B.M. Wu, *Recent advances in 3D printing of biomaterials.* Journal of Biological Engineering, 2015. 9(1): p. 4.

18.F.J. Martínez-Vázquez, et al., *Fabrication of novel Si-doped hydroxyapatite/gelatine scaffolds by rapid prototyping for drug delivery and bone regeneration.* Acta Biomaterialia, 2015. 15: p. 200-209.

19.L. Moroni, et al., *Polymer hollow fiber three-dimensional matrices with controllable cavity and shell thickness.* Biomaterials, 2006. 27(35): p. 5918-5926.

20.A. Tiwari, et al., *Stress analysis of plate with elliptical hole.* International Journal for Innovative Research in Science & Technology, 2016. 3: p. 183-190.

21.W.D. Pilkey and D.F. Pilkey, *Holes*, in *Peterson's stress concentration factors*. Third Edition, 2008, John Wiley & Sons: USA. p. 176-400.

22.J.-H. Woo and W.-B. Na, *Effect of Cutout Orientation on Stress Concentration of Perforated Plates with Various Cutouts and Bluntness.* International Journal of Ocean System Engineering, 2011. 1(2): p. 95-101.

23.J. Rezaeepazhand and M. Jafari, *Stress concentration in metallic plates with special shaped cutout.* International Journal of Mechanical Sciences, 2010. 52(1): p. 96-102.

24.N.P. Patel and D.S. Sharma, *On the stress concentration around a polygonal cut-out of complex geometry in an infinite orthotropic plate.* Composite Structures, 2017. 179: p. 415-436.

25.B.C. Kim, et al., *Guided fracture of films on soft substrates to create micro/nano-feature arrays with controlled periodicity.* Scientific Reports, 2013. 3: p. 3027.

26.R. Adelung, et al., *Strain-controlled growth of nanowires within thin-film cracks.* Nature Materials, 2004. 3: p. 375.

27.M. Kim, D. Ha, and T. Kim, *Cracking-assisted photolithography for mixed-scale patterning and nanofluidic applications.* Nature Communications, 2015. 6: p. 6247.

28.J. Schijve, *Fatigue of aircraft materials and structures.* International Journal of Fatigue, 1994. 16(1): p. 21-32.

29.R. Lakes, *Foam Structures with a Negative Poisson's Ratio.* Science, 1987. 235(4792): p. 1038-1040.

30.K.L. Alderson, A. Fitzgerald, and K.E. Evans, *The strain dependent indentation resilience of auxetic microporous polyethylene.* Journal of Materials Science, 2000. 35(16): p. 4039-4047.

31.K.E. Evans, A. Alderson, and F.R. Christian, *Auxetic two-dimensional polymer networks. An example of tailoring geometry for specific mechanical properties.* Journal of the Chemical Society, Faraday Transactions, 1995. 91(16): p. 2671-2680.

32.T. Lee and R. Lakes, *Anisotropic polyurethane foam with Poisson'sratio greater than 1.* Journal of Materials Science, 1997. 32(9): p. 2397-2401.

33.A. Pickles, et al., *The effect of the processing parameters on the fabrication of auxetic polyethylene.* Journal of Materials Science, 1995. 30(16): p. 4059-4068.

34.E.A. Friis, R.S. Lakes, and J.B. Park, *Negative Poisson's ratio polymeric and metallic foams.* Journal of Materials Science, 1988. 23(12): p. 4406-4414.

35.H.-L. Yeh, H.-Y. Yeh, and R. Zhang, *A Study of Negative Poisson's Ratio in Randomly Oriented Quasi-Isotropic Composite Laminates.* Journal of Composite Materials, 1999. 33(19): p. 1843-1857.

36.D. Li, et al., *Stiff square structure with a negative Poisson's ratio.* Materials Letters, 2017. 188: p. 149-151.

37.W. Gaoxiang, et al., *Directing the Deformation Paths of Soft Metamaterials with Prescribed Asymmetric Units.* Advanced Materials, 2015. 27(17): p. 2747-2752.

38.J. Liu and Y. Zhang, *Soft network materials with isotropic negative Poisson's ratios over large strains.* Soft Matter, 2018. 14(5): p. 693-703.

39.Y. Yao, et al., *Fabrication and characterization of auxetic shape memory composite foams.* Composites Part B: Engineering, 2018. 152: p. 1-7.

40.M. Mir, et al., *Review of Mechanics and Applications of Auxetic Structures.* Advances in Materials Science and Engineering, 2014: p. 17.

41.D.Y. Fozdar, et al., *Three-Dimensional Polymer Constructs Exhibiting a Tunable Negative Poisson's Ratio.* Advanced Functional Materials, 2011. 21(14): p. 2712-2720.

42.U.D. Larsen, O. Signund, and S. Bouwsta, *Design and fabrication of compliant micromechanisms and structures with negative Poisson's ratio.* Journal of microelectromechanical systems, 1997. 6(2): p. 99-106.

43.J.N. Grima, et al., *On the potential of connected stars as auxetic systems.* Molecular Simulation, 2005. 31(13): p. 925-935.

44.A. Spadoni and M. Ruzzene, *Elasto-static micropolar behavior of a chiral auxetic lattice.* Journal of the Mechanics and Physics of Solids, 2012. 60(1): p. 156-171.

45.T. Frenzel, M. Kadic, and M. Wegener, *Three-dimensional mechanical metamaterials with a twist.* Science, 2017. 358(6366): p. 1072-1074.

46.J.N. Grima and K.E. Evans, *Auxetic behavior from rotating squares.* Journal of Materials Science Letters, 2000. 19(17): p. 1563-1565.

47.J.N. Grima, A. Alderson, and K.E. Evans, *Negative Poisson's ratios from rotating rectangles.* Computational Methods in Science and Technology, 2004. 10(2): p. 137-145.

48.J.N. Grima, et al., *On the auxetic properties of rotating rhombi and parallelograms: a preliminary investigation.* Physica Status Solidi (b), 2008. 245(3): p. 521-529.

49.C. Coulais, C. Kettenis, and M. van Hecke, *A characteristic length scale causes anomalous size effects and boundary programmability in mechanical metamaterials.* Nature Physics, 2017. 14: p. 40.

50.J.C.Á. Elipe and A.D. Lantada, *Comparative study of auxetic geometries by means of computer-aided design and engineering.* Smart Materials and Structures, 2012. 21(10): p. 105004.

51.Z. Wang and H. Hu, *Auxetic materials and their potential applications in textiles.* Textile Research Journal, 2014. 84(15): p. 1600-1611.

52.I. Masters and K. Evans, *Models for the elastic deformation of honeycombs.* Composite structures, 1996. 35(4): p. 403-422.

53.T.W. Tan, et al., *Compliance and longitudinal strain of cardiovascular stents: influence of cell geometry.* Journal of Medical Devices, 2011. 5(4): p. 041002.

54.S.K. Bhullar, N.L. Lala, and S. Ramkrishna, *Smart biomaterials-a review.* Reviews on Advanced Materials Science, 2015. 40(3): p. 303-314.

55.Y. Liu and H. Hu, *A review on auxetic structures and polymeric materials.* Scientific Research and Essays, 2010. 5(10): p. 1052-1063.

56.A. Lendlein, et al., *Light-induced shape-memory polymers.* Nature, 2005. 434(7035): p. 879-882.

57.X.-J. Han, et al., *pH-Induced Shape-Memory Polymers.* Macromolecular Rapid Communications, 2012. 33(12): p. 1055-1060.

58.R. Mohr, et al., *Initiation of shape-memory effect by inductive heating of magnetic nanoparticles in thermoplastic polymers.* Proceedings of the National Academy of Sciences of the United States of America, 2006. 103(10): p. 3540-3545.

59.P. Zhang, et al., *Ultrasonic Cavitation Induced Shape-Memory Effect in Porous Polymer Networks.* Macromolecular Rapid Communications, 2016. 37(23): p. 1897-1903.

60.A. Lendlein and S. Kelch, *Shape-Memory Polymers.* Angewandte Chemie International Edition, 2002. 41(12): p. 2034-2057.

61.M. Behl and A. Lendlein, *Shape-memory polymers.* Materials Today, 2007. 10(4): p. 20-28.

62.I. Bellin, et al., *Polymeric triple-shape materials.* Proceedings of the National Academy of Sciences, USA, 2006. 103(48): p. 18043-18047.

63.T. Xie, *Tunable polymer multi-shape memory effect.* Nature, 2010. 464(7286): p. 267.

64.M. Behl, et al., *One-step process for creating triple-shape capability of AB polymer networks.* Advanced Functional Materials, 2009. 19(1): p. 102-108.

65.P.R. Buckley, et al., *Inductively heated shape memory polymer for the magnetic actuation of medical devices.* IEEE Transactions on Biomedical Engineering 2006. 53(10): p. 2075-2083.

66.U.N. Kumar, et al., *Non-contact actuation of triple-shape effect in multiphase polymer network nanocomposites in alternating magnetic field.* Journal of Materials Chemistry, 2010. 20(17): p. 3404-3415.

67.T. Xie, *Tunable polymer multi-shape memory effect.* Nature, 2010. 464: p. 267.

68.I. Kolesov and H. Radusch, *Multiple shape-memory behavior and thermal-mechanical properties of peroxide cross-linked blends of linear and short-chain branched polyethylenes.* Express Polymer Letters, 2008. 2(7): p. 461-473.

69.M. Behl, et al., *Temperature-memory polymer actuators.* Proceedings of the National Academy of Sciences, USA, 2013. 110(31): p. 12555-12559.

70.M. Farhan, et al., *Noncontinuously Responding Polymeric Actuators.* ACS Applied Materials & Interfaces, 2017. 9(39): p. 33559-33564.

71.S. Pandini, et al., *Two-way reversible shape memory behaviour of crosslinked poly(ε-caprolactone).* Polymer, 2012. 53(9): p. 1915-1924.

72.L. Wang, et al., *Reprogrammable, magnetically controlled polymeric nanocomposite actuators.* Materials Horizons, 2018. 5(5): p. 861-867.

73.M. Labet and W. Thielemans, *Synthesis of polycaprolactone: a review.* Chemical Society Reviews, 2009. 38(12): p. 3484-3504.

74.M. Möller, R. Kånge, and J.L. Hedrick, *Sn(OTf)2 and Sc(OTf)3: Efficient and versatile catalysts for the controlled polymerization of lactones.* Journal of Polymer Science Part A: Polymer Chemistry, 2000. 38(11): p. 2067-2074.

75.F. Friess, et al., *Oligo(epsilon-caprolactone)-based polymer networks prepared by photocrosslinking in solution.* Journal of Applied Biomaterials & Functional Materials, 2012. 10(3): p. 273-9.

76.C. Wischke, M. Schossig, and A. Lendlein, *Shape-Memory Effect of Micro-/Nanoparticles from Thermoplastic Multiblock Copolymers.* Small, 2014. 10(1): p. 83-87.

77.W. Wagermaier, et al., *Characterization Methods for Shape-Memory Polymers.* Advances in polymer science, 2010. 226: p. 97-145.

78.A. Lendlein and R. Langer, *Biodegradable, Elastic Shape-Memory Polymers for Potential Biomedical Applications.* Science, 2002. 296(5573): p. 1673-1676.

79.G.M. Baer, et al., *Fabrication and in vitro deployment of a laser-activated shape memory polymer vascular stent.* Biomedical Engineering Online, 2007. 6(8).

80.A.A. Sharp, et al., *Toward a self-deploying shape memory polymer neuronal electrode.* Journal of Neural Engineering, 2006. 3(4): p. 23.

81.C. Wischke and A. Lendlein, *Shape-Memory Polymers as Drug Carriers—A Multifunctional System.* Pharmaceutical Research, 2010. 27(4): p. 527-529.

82.G. Li, et al., *Spatial and temporal control of shape memory polymers and simultaneous drug release using high intensity focused ultrasound.* Journal of Materials Chemistry, 2012. 22(16): p. 7692-7696.

83.M. Gibaldi, M. Lee, and A. Desai, *Gibaldi's drug delivery systems in pharmaceutical care*. 2007: American Society of Health-System Pharmacists.

84.R. Langer and J. Folkman, *Polymers for the sustained release of proteins and other macromolecules.* Nature, 1976. 263: p. 797.

85.S. Luo and D.R. Walt, *Fiber-optic sensors based on reagent delivery with controlled-release polymers.* Analytical Chemistry, 1989. 61(2): p. 174-177.

86.A.S. Hoffman, *Applications of thermally reversible polymers and hydrogels in therapeutics and diagnostics.* Journal of Controlled Release, 1987. 6(1): p. 297-305.

87.T. Werner, I. Klimant, and O.S. Wolfbeis, *Ammonia-sensitive polymer matrix employing immobilized indicator ion pairs.* Analyst, 1995. 120(6): p. 1627-1631.

88.C. Wischke, et al., *Polyalkylcyanoacrylates as in situ formed diffusion barriers in multimaterial drug carriers.* Journal of Controlled Release, 2013. 169(3): p. 321-328.

89.S.A. Molokhia, et al., *The capsule drug device: Novel approach for drug delivery to the eye.* Vision Research, 2010. 50(7): p. 680-685.

90.A.C.R. Grayson, et al., *Multi-pulse drug delivery from a resorbable polymeric microchip device.* Nature Materials, 2003. 2(11): p. 767-772.

91.D. Capodanno, F. Dipasqua, and C. Tamburino, *Novel drug-eluting stents in the treatment of de novo coronary lesions.* Vascular Health and Risk Management, 2011. 7: p. 103.

92.N.K. Varde and D.W. Pack, *Microspheres for controlled release drug delivery.* Expert Opinion on Biological Therapy, 2004. 4(1): p. 35-51.

93.B.G. De Geest, et al., *Layer-by-layer coating of degradable microgels for pulsed drug delivery.* Journal of Controlled Release, 2006. 116(2): p. 159-169.

94.J.C. Wright, et al., *An in vivo/in vitro comparison with a leuprolide osmotic implant for the treatment of prostate cancer.* Journal of Controlled Release, 2001. 75(1): p. 1-10.

95.Y.-C. Su and L. Lin, *A water-powered micro drug delivery system.* Journal of Microelectromechanical Systems, 2004. 13(1): p. 75-82.

96.C. Aschkenasy and J. Kost, *On-demand release by ultrasound from osmotically swollen hydrophobic matrices.* Journal of Controlled Release, 2005. 110(1): p. 58-66.

97.V. Radovan, et al., *Conditional Ultrasound Sensitivity of Poly[(N-isopropylacrylamide)-co-(vinyl imidazole)] Microgels for Controlled Lipase Release.* Macromolecular Rapid Communications, 2015. 36(21): p. 1891-1896.

98.Y. Jing, et al., *Ultrasound-Triggered Smart Drug Release from Multifunctional Core–Shell Capsules One-Step Fabricated by Coaxial Electrospray Method.* Langmuir, 2011. 27(3): p. 1175-1180.

99.Y. Hirokawa and T. Tanaka, *Volume phase transition in a nonionic gel.* The Journal of Chemical Physics, 1984. 81(12): p. 6379-6380.

100. T. Hoare, et al., *A Magnetically Triggered Composite Membrane for On-Demand Drug Delivery.* Nano Letters, 2009. 9(10): p. 3651-3657.

101. J.T.F. Keurentjes, et al., *Externally Triggered Glass Transition Switch for Localized On-Demand Drug Delivery.* Angewandte Chemie International Edition, 2009. 48(52): p. 9867-9870.

102. P.Y. Wang, *Implantable reservoir for supplemental insulin delivery on demand by external compression.* Biomaterials, 1989. 10(3): p. 197-201.

103. R. Lo, et al., *A passive MEMS drug delivery pump for treatment of ocular diseases.* Biomedical Microdevices, 2009. 11(5): p. 959.

104. B. Kim, et al., *A Strain-Regulated, Refillable Elastic Patch for Controlled Release.* Advanced Materials Interfaces, 2016. 3(9).

105. Y. Yang, et al., *Controlled release of BSA by microsphere-incorporated PLGA scaffolds under cyclic loading.* Materials Science and Engineering: C, 2011. 31(2): p. 350-356.

106. J. Di, et al., *Stretch-Triggered Drug Delivery from Wearable Elastomer Films Containing Therapeutic Depots.* ACS Nano, 2015. 9(9): p. 9407-9415.

107. Y. Zhang, et al., *Controlled display of enzyme activity with a stretchable hydrogel.* Chemical Communications, 2013. 49(84): p. 9815-9817.

108. D. Mertz, et al., *Mechanically Responding Nanovalves Based on Polyelectrolyte Multilayers.* Nano Letters, 2007. 7(3): p. 657-662.

109. D. Mertz, et al., *Mechanotransductive surfaces for reversible biocatalysis activation.* Nature Materials, 2009. 8: p. 731.

110. P. Fatemeh, C. Luna, and C. Mu, *A magnetic poly(dimethylesiloxane) composite membrane incorporated with uniformly dispersed, coated iron oxide nanoparticles.* Journal of Micromechanics and Microengineering, 2010. 20(1): p. 015032.

111. F.N. Pirmoradi, et al., *On-demand controlled release of docetaxel from a battery-less MEMS drug delivery device.* Lab Chip, 2011. 11(16): p. 2744-52.

112. N.M. Elman, H.L. Ho Duc, and M.J. Cima, *An implantable MEMS drug delivery device for rapid delivery in ambulatory emergency care.* Biomed Microdevices, 2009. 11(3): p. 625-31.

113. J.M. Maloney, et al., *Electrothermally activated microchips for implantable drug delivery and biosensing.* Journal of Controlled Release, 2005. 109(1-3): p. 244-55.

114. R. Farra, et al., *First-in-Human Testing of a Wirelessly Controlled Drug Delivery Microchip.* Science Translational Medicine, 2012. 4(122): p. 122ra21-122ra21.

115. W. Brostow and H.E. Hagg Lobland, *Brittleness of materials: implications for composites and a relation to impact strength.* Journal of Materials Science, 2009. 45(1): p. 242.

116. Y. Barkan, et al., *Comparative evaluation of polycyanoacrylates.* Acta Biomaterialia, 2017. 48: p. 390-400.

117. H. Lee, et al., *Mussel-Inspired Surface Chemistry for Multifunctional Coatings.* Science, 2007. 318(5849): p. 426-430.

118. W.B. Tsai, et al., *Poly(dopamine) coating to biodegradable polymers for bone tissue engineering.* Journal of Biomaterials Applications, 2014. 28(6): p. 837-48.

119. A.L. Sisson, D. Ekinci, and A. Lendlein, *The contemporary role of ε-caprolactone chemistry to create advanced polymer architectures.* Polymer, 2013. 54(17): p. 4333-4350.

120. A. Lendlein, A.M. Schmidt, and R. Langer, *AB-polymer networks based on oligo(ε-caprolactone) segments showing shape-memory properties.* Proceedings of the National Academy of Sciences, USA, 2001. 98(3): p. 842.

121. T.K. Dash and V.B. Konkimalla, *Poly-ε-caprolactone based formulations for drug delivery and tissue engineering: A review.* Journal of Controlled Release, 2012. 158(1): p. 15-33.

122. A. Lendlein, et al., *Shape-memory polymer networks from oligo(ε-caprolactone)dimethacrylates.* Journal of Polymer Science Part A: Polymer Chemistry, 2005. 43(7): p. 1369-1381.

123. I.D. Johnston, et al., *Mechanical characterization of bulk Sylgard 184 for microfluidics and microengineering.* Journal of Micromechanics and Microengineering, 2014. 24(3): p. 035017.

124. S. Civjan, P.M. Margetis, and R.L. Reddick, *Properties of n-Butyl-α-Cyanoacrylate Mixtures.* Journal of Dental Research, 1969. 48(4): p. 536-542.

125. T. Yokoyama, *Experimental determination of impact tensile properties of adhesive butt joints with the split Hopkinson bar.* The Journal of Strain Analysis for Engineering Design, 2003. 38(3): p. 233-245.

126. C. Xie and W. Tong, *Cracking and decohesion of a thin Al2O3 film on a ductile Al–5%Mg substrate.* Acta Materialia, 2005. 53(2): p. 477-485.

127. S. Krishnamurthy and I. Reimanis, *Multiple cracking in CrN and Cr 2 N films on brass.* Surface and Coatings Technology, 2005. 192(2): p. 291-298.

128. A.A. Abd Elhady, *Sress and strain concentration factors for plate with small notch subjected to biaxial loading – Three dimensional finite element analysis.* Ain Shams Engineering Journal, 2010. 1(2): p. 139-145.

129. Z. Yang, et al., *The concentration of stress and strain in finite thickness elastic plate containing a circular hole.* International Journal of Solids and Structures, 2008. 45(3): p. 713-731.

130. D. Kawadkar, D. Bhope, and S. Khamankar, *Evaluation of Stress Concentration in Plate with Cut-Out and Its Experimental Verification.* International Journal of Engineering Research and Applications, 2012. 2(5): p. 566-571.

131. K.L. Mittal, *Adhesion Measurement of Thin Films.* ElectroComponent Science and Technology, 1976. 3(1): p. 21-42.

132. Materials Properties Database. Available from: www.matweb.com.

133. C.B. Walsh and E.I. Franses, *Ultrathin PMMA films spin-coated from toluene solutions.* Thin Solid Films, 2003. 429(1–2): p. 71-76.

134. S. Khodaparast, et al., *Water-based peeling of thin hydrophobic films.* Physical review letters, 2017. 119(15): p. 154502.

135. C. Wischke, et al., *Understanding instability and rupture of poly(alkyl-2-cyanoacrylate) capsules.* Int J Artif Organs, 2011. 34(2): p. 243-248.

136. W. Sheng, et al., *Brushing up from "anywhere" under sunlight: a universal surface-initiated polymerization from polydopamine-coated surfaces.* Chemical Science, 2015. 6(3): p. 2068-2073.

137. B. Zhu and S. Edmondson, *Polydopamine-melanin initiators for surface-initiated ATRP.* Polymer, 2011. 52(10): p. 2141-2149.

138. H. Hu, et al., *Modification of carbon nanotubes with a nanothin polydopamine layer and polydimethylamino-ethyl methacrylate brushes.* Carbon, 2010. 48(8): p. 2347-2353.

139. F. Zhang, et al., *Accelerated Curing Speed of Ethyl α-Cyanoacrylate by Polymer with Catecholamine Groups.* Chinese Journal of Chemistry, 2012. 30(10): p. 2275-2280.

140. D. Beech, *Bonding of alkyl 2-cyanoacrylates to human dentin and enamel.* Journal of dental research, 1972. 51(5): p. 1438-1442.

141. D.J. Boday, et al., *Strong, low-density nanocomposites by chemical vapor deposition and polymerization of cyanoacrylates on aminated silica aerogels.* ACS applied materials & interfaces, 2009. 1(7): p. 1364-1369.

142. J. Liebscher, et al., *Structure of Polydopamine: A Never-Ending Story?* Langmuir, 2013. 29(33): p. 10539-10548.

143. P. Klemarczyk, *The isolation of a zwitterionic initiating species for ethyl cyanoacrylate (ECA) polymerization and the identification of the reaction products between 1°, 2°, and 3° amines with ECA.* Polymer, 2001. 42(7): p. 2837-2848.

144. W. Dong Yang, et al., *Ammonia plasma treatment of polyolefins for adhesive bonding with a cyanoacrylate adhesive.* Journal of Adhesion Science and Technology, 1995. 9(4): p. 501-525.

145. H. Hillborg, et al., *Crosslinked polydimethylsiloxane exposed to oxygen plasma studied by neutron reflectometry and other surface specific techniques.* Polymer, 2000. 41(18): p. 6851-6863.

146. M. Ebara, et al., *Switchable surface traps for injectable bead-based chromatography in PDMS microfluidic channels.* Lab on a Chip, 2006. 6(7): p. 843-848.

147. K.H. Nam, I.H. Park, and S.H. Ko, *Patterning by controlled cracking.* Nature, 2012. 485: p. 221.

148. J. Huang, et al., *The control of crack arrays in thin films.* Journal of Materials Science, 2014. 49(1): p. 255-268.

149. Y.K.D.V. Prasad and S. Somasundaram, *A mathematical model for bend-allowance calculation in automated sheet-metal bending.* Journal of Materials Processing Technology, 1993. 39(3): p. 337-356.

150. K. Cai, et al., *Effects of size and surface on the auxetic behaviour of monolayer graphene kirigami.* Scientific Reports, 2016. 6: p. 35157.

151. H. Meng and G. Li, *A review of stimuli-responsive shape memory polymer composites.* Polymer, 2013. 54(9): p. 2199-2221.

152. H. Koerner, et al., *Remotely actuated polymer nanocomposites-stress-recovery of carbon-nanotube-filled thermoplastic elastomers.* Nature Materials, 2004. 3(2): p. 115-120.

153. M. Razzaq, et al., *Controlled actuation of shape-memory nanocomposites by application of an alternating magnetic field.* Materials Research Society Symposium Proceedings, 2009. 1140: p. 185-190.

154. H. Wan, et al., *A study of negative Poisson's ratios in auxetic honeycombs based on a large deflection model.* European Journal of Mechanics - A/Solids, 2004. 23(1): p. 95-106.

155. X.-c. Zhang, et al., *Numerical Investigation on Dynamic Crushing Behavior of Auxetic Honeycombs with Various Cell-Wall Angles.* Advances in Mechanical Engineering, 2015. 7(2): p. 679678.

156. R.A. Zangmeister, T.A. Morris, and M.J. Tarlov, *Characterization of Polydopamine Thin Films Deposited at Short Times by Autoxidation of Dopamine.* Langmuir, 2013. 29(27): p. 8619-8628.

157. F. Leonard, J.A. Collins, and H.J. Porter, *Interfacial polymerization of n-alkyl α-cyanoacrylate homologs.* Journal of Applied Polymer Science, 1966. 10(11): p. 1617-1623.

158. H. Jaffe, et al., *Synthesis and bioevaluation of alkyl 2-cyanoacryloyl glycolates as potential soft tissue adhesives.* Journal of Biomedical Materials Research, 1986. 20(2): p. 205-212.

159. B. Mizrahi, et al., *Elasticity and safety of alkoxyethyl cyanoacrylate tissue adhesives.* Acta Biomaterialia, 2011. 7(8): p. 3150-3157.

160. B.-F. Ju, K.-T. Wan, and K.-K. Liu, *Indentation of a square elastomeric thin film by a flat-ended cylindrical punch in the presence of long-range intersurface forces.* Journal of Applied Physics, 2004. 96(11): p. 6159-6163.

161. Y.-C. Tseng, S.-H. Hyon, and Y. Ikada, *Modification of synthesis and investigation of properties for 2-cyanoacrylates.* Biomaterials, 1990. 11(1): p. 73-79.

162. Y. Zhang, et al., *Mechanical properties of PTFE coated fabrics.* Journal of Reinforced Plastics and Composites, 2010. 29(24): p. 3624-3630.

163. N.K. Uttamchand, et al., *Triple-Shape Capability of Thermo-sensitive Nanocomposites from Multiphase Polymer Networks and Magnetic Nanoparticles.* Materials Research Society Proceedings, 2011. 1190: p. 1190-NN03-21.